Characterization of virus-like particles from the BEVS platform with a special focus on gradient ultracentrifugation

by

Nicholas Cheng

A thesis
presented to the University of Waterloo
in fulfillment of the
thesis requirement for the degree of
Master of Science
in
Pharmacy

Waterloo, Ontario, Canada, 2026

© Nicholas Cheng 2026

Author's Declaration

I hereby declare that I am the sole author of this thesis. This is a true copy of the thesis, including any required final revisions, as accepted by my examiners.

I understand that my thesis may be made electronically available to the public.

Abstract

Coronaviruses continue to be an evolving threat, and Severe Acute Respiratory Syndrome (SARS) Virus-Like-Particles (VLPs) may be suitable as vaccine candidates. Early indications were that a SARS-VLP could be generated based on a universal betacoronavirus sequence using only Spike, Envelope and Membrane structural proteins. This process involved the generation of VLPs through the insect cell-baculovirus expression vector system (IC-BEVS), followed by semi-purification via gradient ultracentrifugation and subsequent fractionation. Collected fractions were analyzed by bicinchonic acid assay, flow virometry, immunoblotting, and multi-angle dynamic light scattering. Particle concentration, size, DNA content, and surface protein composition was determined for semi-purified samples.

This study provides a clearer understanding of biological dynamics in VLP generation workflows, by comparing HIV-VLPs, SARS-VLPs, baculovirus, and other co-produced particles. It was expected that significant concentrations of particles would not be observed in uninfected Sf9 cell culture supernatant samples, baculovirus alone would be observed in non-VLP producing samples, and VLPs would be observed in addition to baculovirus in VLP major structural protein producing samples. MADLS was used to assess the size and concentration of all particles produced and semi-purified, since all samples would be treated identically prior to measurement. It can be concluded that though both types of VLPs possess similarly-derived envelopes, their behavior is highly dependent on structural protein composition.

In terms of particle diameter, VLPs were expected to range between 50 nm and 250 nm, and baculovirus at 250 nm and greater. Post semi-purification, it was noted that

some particles in the expected size range of baculovirus and VLP were detected in all samples, between fractions of densities 1.05 to 1.21 g/mL. Further analysis elucidated that uninfected samples had significantly lower measurement accuracy and a larger range of mean concentrations and sizes for those particles, which indicates a lack of reliability. Particles in the expected size range for VLPs found in non-VLP producing baculovirus samples were far more consistent, and determined to be real particles between densities 1.07 to 1.17 g/mL. These may be extracellular vesicles produced by insect cells under stress of infection, which have been documented in literature. Particles in the expected size range for baculovirus for this sample were also found in this density range. In VLP producing samples, particles were found that were consistent with expected size ranges for VLPs and baculovirus in the density ranges of 1.07 to 1.17 g/mL. Data from multiple orthogonal methods confirmed that the fraction containing the highest concentration of non-fluorescent HIV-VLPs, SARS-VLPs, and baculovirus was that with a density of 1.13 g/mL. Fluorescent HIV-VLPs by contrast, appeared less dense and had a maximum concentration at a density of 1.10 g/mL. In examining MADLS as a method of better characterizing the SARS-VLP, significant knowledge about the IC-BEVS was obtained which will assist in further developing this system and associated downstream purification processes.

Acknowledgements

I would like to thank all the people who made this thesis possible.

Dr. Aucoin, Dr. Slavcev, Dr. Beazely, Dr. Dixon, Dr. Nafissi

From the Aucoin lab: Scott Boegel, Dr. Christiane Nogueira, Lisa Nielsen, Jacqueline Powichrowski, Kenth Maquiling, Dr.Madhuja Chakraborty, Christopher Sung, Dr. Aaron Yip.

From the Slavcev lab: Dr. Jesse St. Jean, Dr. Hibah Alattas, Merium Fernando, Rohini Prakash, Dr. Kholoud Shaban, Ikechukwu Benjamin Moses, Thaddeus Gugu, Anna Kosiak, Anna Ffrench, Adam Falah, Julia Lumini.

Fellow co-supervised students: Andrew Ng, Deborah Pushparajah, Jiayang Li, Morgan Cardno, Mehraveh Hosseinali.

Inspiration and other assistance: Dr. Derek Smith, Dr. Donna Strickland, Dr. Tania Rodríguez Ramos, Dr. Jennifer Aguiar, Ibrahim Mubarik, Maggie Wong, William Cheng, Courtney MacPherson, Walton Smith, Manuel Ron Lleras, Patrick Aldridge, Ilya Kovalevskiy, Alexander Krcmarov, Manuel Aliendre, Liam Gauthier, Antun Dvorski, Benjamin Raskin, Aviel Avshalumov, David Ferguson... and many others!

Dedication

This is dedicated to Sir Edward Jenner and all his descendants, specifically my good friend, Solstice Morrell.



Figure 1: SLt Solstice Morrell at sea, left, portrait of Sir Edward Jenner, right [1]

Table of Contents

Author's Declaration ii

Abstract iii

Acknowledgements v

Dedication vi

List of Figures xii

List of Tables xvi

List of Abbreviations xvii

1 Introduction 1

1.1 Context 1

1.2 Rationale 5

1.3 Hypothesis 7

1.4 Objectives 8

2 Literature Review **9**

2.1 Viral Structure . . . 9

2.1.1 Coronavirus . . . 10

2.1.2 HIV . . . 11

2.2 IC-BEVS . . . 12

2.2.1 Baculovirus . . . 13

2.3 Ultracentrifugation . . . 13

2.3.1 Cushion . . . 14

2.3.2 Gradient . . . 14

2.4 Dynamic Light Scattering . . . 15

2.5 State of Art of VLP characterization . . . 16

3 Methods **22**

3.1 Overall process . . . 22

3.2 Cells and Viruses . . . 24

3.3 Insect Cell Culture and Maintenance . . . 24

3.4 Virus Amplification . . . 25

3.5 Infectious Virus Titering . . . 25

3.6 Recombinant Protein/VLP Production . . . 26

3.7 Flow Virometry . . . 26

3.7.1 Total Virus Particle Count via SYBR Green Staining . . . 27

3.7.2 Fluorescent Virus-Like Particle Count . . . 28

3.7.3 Accounting for Fluorescent Virus-Particle Count in SYBR Green I Staining Protocol . . . 28

3.8 Dot blotting . . . 29

3.9 SDS-PAGE and Western blotting . . . 30
3.10 BCA Assay . . . 33
3.11 Multi-Angle Dynamic Light Scattering . . . 34
3.12 Sucrose Cushion Ultracentrifugation . . . 35
3.13 Iodixanol Gradient Ultracentrifugation . . . 36
3.13.1 Iodixanol Gradient Ultracentrifugation Fraction Collection . . . 37
3.13.2 Density of Iodixanol Gradient Ultracentrifugation Fractions . . . 38
3.14 Rheometry of Iodixanol Solutions . . . 38
3.15 Refractometry of Iodixanol Solutions . . . 39

4 Results **41**
4.1 Cell culture and harvest . . . 42
4.1.1 Growth Curves . . . 42
4.2 Ultracentrifugation Fraction Characterization . . . 47
4.2.1 Fraction Density . . . 47
4.2.2 Total Protein Content . . . 49
4.2.3 Flow Virometry . . . 51
4.2.4 Immunoblotting . . . 55
4.2.5 Multi-Angle Dynamic Light Scattering . . . 62
4.2.6 Correlation of Orthogonal Methods . . . 77

5 Discussion **83**
5.1 Growth and Infection of cell cultures . . . 85
5.2 Baculovirus and VLP Proteins in Iodixanol Fractions . . . 87
5.3 MADLS identifies two distinct particle populations . . . 91
5.4 GFP fusion alters GAG-VLP produced in IC-BEVS . . . 94

6 Conclusions and Future Directions **98**

6.1 Semi-purification of recombinant products 99

6.2 MADLS characterization of iodixanol fractions 100

6.3 An EV-based model for VLP production in IC-BEVS 101

6.4 Study Limitations 102

6.5 Future Directions 104

References **106**

APPENDICES **123**

A General **124**

A.1 Consensus SARS-CoV-2 Sequences 124

B Flow Virometry **126**

B.1 Equations 126

B.1.1 Calculations associated with SYBR green staining of baculovirus particles 126

B.2 Supplementary Results 127

B.2.1 Infected Cell Culture Supernatant Characterization 127

B.2.2 Semi-Purification Characterization 131

C Multi-Angle Dynamic Light Scattering **136**

C.1 Equations 136

C.1.1 Rayleigh Scattering Intensity Law 136

C.1.2 Stokes - Einstein - Sutherland 137

C.1.3 Rayleigh–Gans–Debye Approximation 137

C.1.4 Beer–Lambert Law 138
C.2 Supplementary Results 139
C.2.1 Density 139
C.2.2 Refractive Index 140
C.2.3 Viscosity 141
C.2.4 MADLS Analysis of Separation Medium 143
C.3 MADLS Methodology 144
C.3.1 Concentration 145
C.3.2 Size 151
C.3.3 Particle Detection Variability 153
C.3.4 Solvent Peaks 161
C.3.5 Estimated VLP Concentration 163

List of Figures

1 Sir Edward Jenner and his descendant vi

3.1 Flowchart of sequential experimental processes and analytical techniques. . 23

4.1 Viability curves of Sf9 cells cultured without passaging until a given viability was reached. 43

4.2 Viability curves of Sf9 cells post-infection with a given recombinant baculovirus. 44

4.3 Growth curves of Sf9 cells post-infection with a given recombinant baculovirus. 46

4.4 Density of semi-purified samples. 48

4.5 Total protein content of semi-purified samples. 50

4.6 Flow virometry-derived dsDNA-containing particle concentration in semi-purified samples. 52

4.7 Flow virometry-derived particle concentration in semi-purified samples. . . 54

4.8 Anti-GP64 immunoblots of semi-purified samples (rBEV-mKOκ and SARS-VLP). 56

4.9 Anti-GP64 immunoblots of semi-purified samples (GAG-VLP and GAG-GFP-VLP). 57

4.10 Anti-P24 immunoblots of semi-purified samples (GAG-VLP and GAG-GFP-VLP). 59

4.11 Anti-Spike immunoblots of semi-purified samples (SARS-VLP) 61
4.12 MADLS: Concentration of particles between 50 nm < diameter < 250 nm. 65
4.13 MADLS: Size of particles between 50 nm < diameter < 250 nm. 66
4.14 MADLS: Concentration of particles of diameter > 250 nm. 68
4.15 MADLS: Size of particles of diameter > 250 nm. 69
4.16 MADLS: Concentration of particles of diameter > 250 nm after sample-matching subtraction. 71
4.17 MADLS: Size of particles between 50 nm < diameter < 250 nm after sample matching subtraction. 72
4.18 MADLS: Fold-increase in concentration of particles of diameter > 250 nm. 73
4.19 MADLS: Fold-increase in concentration of particles between 50 nm < diameter < 250 nm. 74
4.20 Correlation between MADLS-derived particle concentration and dsDNA-containing particle concentration. 78
4.21 Correlation between MADLS-derived particle concentration and fluorescent particle concentration. 79

5.1 Proposed mechanism for production of enveloped VLPs in insect cell-baculovirus expression vector system. 97

B.1 Flow virometry-derived dsDNA-containing particle concentration in infected cell culture supernatant samples. 128
B.2 Flow virometry-derived fluorescent particle concentration in infected cell culture supernatant samples. 130
B.3 Flow virometry-derived dsDNA-containing particle yield percentages at semi-purification stages. 132
B.4 Flow virometry-derived particle yield percentages at semi-purification stages. 134

C.1 Density of iodixanol-NTC solutions. 140
C.2 Refractive index of iodixanol-NTC solutions. 141
C.3 Viscosity of iodixanol-NTC solutions. 142
C.4 Light scattering intensity and size distribution of particles in solutions of iodixanol-NTC, pre and post correction. 144
C.5 MADLS-derived particle concentration measurement of known sample versus buffer for particles of a given diameter range. 146
C.6 MADLS-derived measurements of known sample for particles where (50 nm < diameter < 250 nm). 148
C.7 MADLS-derived measurements of known sample for particles where (diameter > 250 nm). 150
C.8 MADLS-derived particle size measurement of known sample versus buffer for particles of a given diameter range. 152
C.9 Hit rate of known sample versus buffer for particles of a given diameter range. 154
C.10 Hit rate of semi-purified samples for particles of (50 nm < diameter < 250 nm). 156
C.11 Hit rate of semi-purified samples for particles of (50 nm < diameter < 250 nm). 157
C.12 Hit rate of semi-purified infected samples for particles of (diameter > 250 nm). 159
C.13 Hit rate of semi-purified uninfected samples for particles of (diameter > 250 nm). 160
C.14 Aggregated MADLS-derived size measurements of solvent peaks across semi-purified samples. 162
C.15 Estimated concentration of VLPs in VLP-producing samples. 164
C.16 Correlation: Particle concentration between dsDNA-containing and sample matched subtraction of > 250 nm in diameter. 166

C.17 Correlation: Particle concentration between fluorescent and sample matched subtraction of 50 nm < diameter < 250 nm. 167

C.18 Correlation: Particle concentration between fluorescent and 50 nm < diameter < 250 nm in semi-purified samples, by biological replicates. 168

C.19 Correlation: Particle concentration between dsDNA-containing and diameter > 250 nm in semi-purified samples, by biological replicates. 169

C.20 MADLS (1-6): Concentration of particles between 50 nm < diameter < 250 nm. 170

C.21 MADLS (1-6): Size of particles between 50 nm < diameter < 250 nm. . . . 171

C.22 MADLS (1-6): Concentration of particles of diameter > 250 nm. 172

C.23 MADLS (1-6): Size of particles of diameter > 250 nm. 173

List of Tables

2.1 Recent studies characterizing enveloped VLPs derived from HIV or SARS-CoV-2. 18

3.1 Description of recombinant baculovirus vectors used in this study. 24

A.1 Comparison between wild-type and consensus-based SARS-CoV-2 major structural proteins 125

List of Abbreviations

ACE2	angiotensin-converting enzyme 2
AcMNPV	*Autographa californica* multiple nucleopolyhedrovirus
APS	ammonium persulfate
ATCC	American Type Culture Collection
BCA	bicinchoninic acid
BEVS	baculovirus expression vector system
CA	capsid (protein)
DLS	dynamic light scattering
dsDNA	double-stranded deoxyribonucleic acid
ELISA	enzyme-linked immunosorbent assay
EPDA	end-point dilution assay
ESCRT	endosomal sorting complex required for transport
EV	extracellular vesicle
eVLP	enveloped virus-like particle
GAG	group-specific antigen
GFP	green fluorescent protein
GP64	baculovirus major envelope glycoprotein GP64
HIV	human immunodeficiency virus
HPI	hours post-infection
HRP	horseradish peroxidase
IC-BEVS	insect cell–baculovirus expression vector system
MA	matrix (protein)
mAG	monomeric Azami-Green

MADLS	multi-angle dynamic light scattering
MERS-CoV	Middle East Respiratory Syndrome coronavirus
mKOκ	monomeric Kusabira-Orange-κ
MOI	multiplicity of infection
mRNA	messenger ribonucleic acid
MSP	major structural protein
NC	nucleocapsid (protein)
NIH	National Institutes of Health
NTA	nanoparticle tracking analysis
P24	HIV-1 capsid protein p24
PBS	phosphate-buffered saline
PVDF	polyvinylidene difluoride
rBEV	recombinant baculovirus
RT	room temperature
SARS-CoV	Severe Acute Respiratory Syndrome coronavirus
SARS-CoV-2	Severe Acute Respiratory Syndrome coronavirus 2
SARS-VLP	SARS coronavirus-like particle
SDS-PAGE	sodium dodecyl sulfate–polyacrylamide gel electrophoresis
Sf9	*Spodoptera frugiperda* cell line 9
SMV	single-membrane vesicle
TBS	Tris-buffered saline
TEM	transmission electron microscopy
TEMED	*N,N,N′,N′*-tetramethylethylenediamine
VLP	virus-like particle
VLP-EV	virus MSP-decorated extracellular vesicle
WB	Western blot
WHO	World Health Organization

Chapter 1

Introduction

1.1 Context

December 31st, 2019: The World Health Organization (WHO) China was alerted by local health authorities to rising cases of pneumonia with an unknown cause centered around Wuhan, Hubei province [2]. March 11th, 2020: The WHO declares a pandemic caused by a new coronavirus strain, dubbed COVID-19 [3]. January 12th, 2023: Global statistics indicate 666 million confirmed cases and 6.7 million deaths caused by the virus [4]. The agent of disease was classified as Severe Acute Respiratory Syndrome Coronavirus 2 (SARS-CoV-2), belonging to the beta coronavirus family known to infect humans and other mammals. Unlike other recent coronaviruses such as Middle-East Respiratory Syn-

drome (MERS-CoV) and Severe Acute Respiratory Syndrome (SARS-CoV), SARS-CoV-2 has decreased lethality, with death rates of 34.4%, 9.5% and 2.13% respectively [5]. This relatively lower virulence is linked to high transmissibility of SARS-CoV-2, which is hypothesized to be caused by enhanced Spike protein cleavage in addition to higher binding efficiency of target human receptors and elevated viral load in pre-symptomatic patients [6].

Pharmaceutical companies have brought several competing vaccines, approved by health Canada, to the market using messenger ribonucleic acid (mRNA) (Pfizer-BioNTech/Moderna), adenovirus (Ad5) (Johnson and Johnson/AstraZeneca), recombinant protein (Novavax) and virus-like particle (Medicago) technologies [7]. Despite this rapid and diverse vaccine roll out, the virus accrued viable mutations and continued to evolve. This led to the classification of several variants of the original SARS-CoV-2 virus, known as the index virus, identified by Greek letters and dates of earliest sample collection: Alpha (Sep-2020), Beta (May-2020), Gamma (Nov-2020), Delta (Oct-2020), Omicron (Nov-2021) [8]. Disconcertingly, sub-variants have been demonstrated to evade detection by antibodies purified from sera of patients who have been double vaccinated by the Pfizer-BioNTech mRNA vaccine. Genomic analysis of one such variant suggests that this "immune escape" property was conferred by non-receptor binding domain gene mutations [9]. Clearly the need for a vaccine against a particular variant is lesser when compared to that for one which is all

encompassing.

The concept of such a universal vaccine has been explored at length by a variety of organizations from military research departments to NIH-funded start-ups, each with its own platform and direction [10]. On January 18th, 2023 a collaboration between the U.S. Army and the Henry M. Jackson foundation released a phylogenetic-based design for a "pan-coronavirus" vaccine using receptor binding domain consensus sequences produced from three distinct groupings of human, animal and human-like coronaviruses [11]. Marrying the ideas of consensus-related universality and VLP technology leads to the belief of cross-variant protection if sufficient generation of broadly neutralizing antibodies and a durable cytotoxic T-cell response are achieved. This "universal" VLP would be an incredibly valuable asset to the pharmaceutical manufacturer that secures a licensing agreement because many governmental agencies have mandates to secure supplies of an effective vaccine for their personnel to reduce illness-related work interruptions [12].

Fundamentally VLPs are particles that resemble viruses and typically do not contain viral genomes, consequently they can't replicate or have productive infections [13]. These types of particles may be better than inactivated, mRNA, or subunit vaccines in terms of eliciting an appropriate immune response while also being safer than live-attenuated vaccines [14]. VLPs of all shapes and sizes can be made through cell culture, and the insect cell-baculovirus expression vector system (IC-BEVS) has been touted as a good

platform for their production [15]. Enveloped viruses, such as influenza, SARS-CoV-2, and HIV are important pathogens for which vaccines are being developed [16]. Enveloped VLPs derived from these viruses may be good as candidate vaccines; however in this system, recombinant baculovirus is co-produced with these particles. The properties of the enveloped VLP and baculovirus may be similar enough to complicate purification. Though deemed non-pathogenic in mammalian cells, residual baculovirus titer must be assessed in the production of VLP products derived from IC-BEVS [17, 18].

In this work, we use validated techniques and explore multi-angle dynamic light scattering (MADLS) in particular to ascertain the production of a novel SARS-VLP created using consensus sequences from SARS-CoV, MERS-CoV and SARS-CoV-2. Given that the number of sequences for SARS-CoV-2 were dominant, the sequence used is closely tied to circulating SARS-CoV-2 strains.

To dive into the characterization of the SARS-VLP after its production, these particles were semi-purified using sucrose cushion and iodixanol density gradient ultracentrifugations. Iodixanol is a good medium for the recovery of virus particles; however, the different concentrations of iodixanol in the gradients influence the readouts of MADLS measurements.

This thesis starts with a review of enveloped virus structure, the IC-BEVS production platform, ultracentrifugation-assisted semi-purification, particle characterization us-

ing MADLS, and the state of art of enveloped VLP characterization (Chapter 2). Chapter 3 discusses use of established and novel methodologies for particle characterization in this work. Chapter 4 presents results of experiments with different VLPs and samples as controls that can be used to help understand the production of SARS-VLPs. Chapter 5 provides insight into knowledge obtained through this work as well as its implications. Chapter 6 details conclusions from our work and future directions for the exploitation of our findings.

1.2 Rationale

Current gold standard techniques for VLP characterization include immunochemical means such as Western blotting and enzyme-linked immunosorbent assay, as well as high-resolution visualization such as transmission electron microscopy. These techniques are expensive, time-consuming, and require great operator skill. This makes them unsuitable for high-throughput experimental VLP purification workflows. The development of affordable, rapid, and low-skill barrier techniques for VLP characterization would widen the bottleneck in these workflows.

Attempts to generate fluorescent SARS-VLPs via fusion of the Spike major structural protein with a fluorescent protein do not report retained VLP assembly or Spike function-

ality. The sensitivity of Spike to modifications underscores its importance in viral assembly and egress, however this makes it difficult to visualize SARS-VLPs directly using fluorescence. Fluorescent HIV-derived VLPs have been extensively studied and are expected to possess similar physical characteristics to SARS-VLPs, as well as both particle types having been proven to be produced in IC-BEVS. If semi-purification methods result in both particle types distributing similarly due to comparable physical characteristics, it stands to reason that fluorescent HIV-derived VLPs may act as a more easily visualized surrogate for SARS-VLP in purification workflows.

MADLS is used industrially to characterize a wide range of particles, from lipid nanoparticles to cement grains. A distinct advantage over Single-Angle Dynamic Light Scattering (DLS) is that MADLS is capable of resolving distinct particle populations in a single sample. Though analysis on semi-purified enveloped VLP products of IC-BEVS has not yet been reported in literature, it may prove effective at determining particle concentration of both VLPs and baculoviruses.

To characterize the SARS-VLP, orthogonal methods were used and SARS-VLP samples were compared to samples containing HIV-VLPs, baculovirus, and non-viral insect cell secretions. Specifically 3 additional IC-BEVS-derived samples were generated, an HIV-VLP, a green fluorescent HIV-VLP, and an orange fluorescent protein that is not expected to form VLPs. The non-fluorescent HIV-VLP was included to control for all aspects of pro-

duction of the fluorescent HIV-VLP except the fluorescence imparting protein. This will allow observations to be made regarding the impact of this fluorescent protein on VLP characteristics and production. Since all VLPs explored here will be produced using the IC-BEVS, it is expected that baculovirus will be present to some degree in the semi-purified samples. By comparing samples expected to contain VLPs to one that is not expected to produce a VLP, the contribution of the VLP presence to the analysis can be determined in isolation of the baculovirus contribution present in all IC-BEVS-derived samples. Similarly, by comparing analysis of previous samples to uninfected insect cells allowed to reach a viability similar to that of infected cells, the contribution of the baculovirus to semi-purification is able to be assessed. Two samples of uninfected cells were allowed to reach viabilities corresponding to upper and lower bounds at which cells subjected to IC-BEVS would be harvested.

1.3 Hypothesis

SARS-VLPs produced using the insect cell–baculovirus expression vector system (IC-BEVS) are efficiently assembled and extruded into the culture supernatant in a manner consistent with established enveloped VLP systems, and consequently exhibit physical, biophysical, and purification behaviors comparable to well-characterized HIV-derived VLPs,

enabling the latter to serve as fluorescent surrogates for monitoring SARS-VLP purification.

1.4 Objectives

1. Produce and harvest IC-BEVS supernatants from four recombinant baculoviruses encoding major structural proteins of SARS-VLPs, GAG-GFP VLPs, GAG VLPs, and the non-assembling mKusabira-Orange-κ protein, alongside uninfected Sf9 controls, under matched conditions and at defined cell viabilities, followed by standardized semi-purification.

2. Quantitatively and qualitatively characterize the resulting semi-purified preparations using established analytical methods, including fluorescence flow virometry, SYBR-Green flow virometry, bicinchoninic acid (BCA) protein quantification, Western and dot blot analyses, to benchmark SARS-VLPs against positive (GAG-based) and negative controls.

3. Evaluate particle size distribution of all semi-purified samples using advanced biophysical analysis, specifically multi-angle dynamic light scattering (MADLS), to complement conventional assays and assess its utility for VLP characterization.

Chapter 2

Literature Review

2.1 Viral Structure

Structural protein self-assembly and lipid membrane interactions are both key forces that result in formation of multivalent, repetitive surface structures in enveloped VLPs (eVLPs) [19]. These patterns mimic native viral pathogen associated molecular patterns, which can cross-link B-cell receptors and activate innate immune pathways alike, resulting in strong immunological responses that make the VLP an attractive vaccine platform [20]. Despite genomic material being absent from VLPs, certain structural proteins may originally serve to interact with nucleic acid polymers to stabilize the native virion [19]. Coronavirus and HIV are both enveloped viruses, however their structural proteins possess key differences,

necessitating contextual appreciation when using them to develop an eVLP platform [21].

2.1.1 Coronavirus

In addition to various non-structural proteins, the typical coronavirus has four major structural proteins – Spike (S), Envelope (E), Membrane (M), and Nucleocapsid (N) [22]. S trimers embedded into the outer surface of the virion interact with host cell receptors [22]. E pentamers form a cation-selective channel that functions as a viroporin and mediates viral maturation [22]. M dimers guide interaction between structural proteins and the host-cell derived envelope [22]. N binds to viral RNA and allows it to be packaged into nascent virions [22].

S, E, and M are translated individually from viral mRNA and embed on the inner membrane of the endoplasmic reticulum [23]. Proceeding through the endoplasmic reticulum-Golgi intermediate complex into the Golgi body, they are trafficked to the inner membrane of single-membrane vesicles (SMV) [24]. N is synthesized in the cytoplasm and associates with transcribed viral RNA, which causes proximate SMVs to invaginate and form mature viral particles [24]. SMVs then fuse with the plasma membrane resulting in coronavirus virion egress into the extracellular milieu [24].

Studies have shown that S, E, and M alone can form VLPs with a characteristic coronavirus "crown" structure visible on negative-stain TEM [25, 26]. Structurally they appear

similar to native SARS-CoV-2 virions, albeit lacking internal electron-dense internal components [25, 26]. These VLPs have been further tested on mouse models to demonstrate generation of anti-Spike antibodies and infer their effectiveness in neutralizing coronavirus samples with promising early results even in the absence of the nucleocapsid [26].

2.1.2 HIV

HIV, like many retroviruses, has three major genetic components – Group-specific antigen (gag), Polymerase (pol), and Envelope (env) [27]. The *gag* gene produces Gag polyprotein which forms structural scaffolding of the virion, env provides the surface glycoprotein that directs receptor targeting, and pol encodes essential enzymes for viral infection, production, and maturation [28].

Gag polyproteins are shown to interact with one another on the inner leaflet of the plasma membrane localized to lipid rafts, resulting in virion self-assembly and egress [29]. Gag is cleaved into the HIV major structural proteins: Matrix (p17), Capsid (P24), Nucleocapsid (p7), and p6 [28]. These reorganize and virion maturation is achieved, which is essential for the virion to be infective [30].

The self-assembling property of the Gag polyproteins can induce formation of VLPs in the absence of a viral genome, env, and pol [31]. These Gag-VLPs are similar to the immature form of HIV-1 virions, each containing approximately 5000 Gag polyproteins,

and have been exploited by researchers as a reliable VLP platform for display of viral antigens from a variety of viral species such as influenza [32, 33]. These Gag-VLPs are able to form even when a green fluorescent protein (GFP) has been fused to the 3' terminus of Gag, resulting in fluorescent GAG-GFP-VLPs that can be more easily identified and quantified post-production [31].

2.2 IC-BEVS

The IC-BEVS has been used extensively as a production platform for recombinant protein production owing to its high expression levels and advantage of being a eukaryotic-based system [34]. Typical cell lines used include Sf9 and Sf21, spontaneously immortalized clones derived from *Spodoptera frugiperda* ovarian tissue [35]. Suspension or adherent cultured cells are infected with engineered baculovirus to produce recombinant protein [34]. Use of recombinant baculovirus as a vector confers much flexibility in protein expression, however the main drawback is that baculovirus virions are co-produced [34]. Though this is not a major complication when expressing recombinant proteins in IC-BEVS, it convolutes separation if the system is used to produce enveloped VLPs [36]. To improve the suitability of IC-BEVS to produce enveloped VLPs, methods to reduce baculovirus titer have been explored and show great promise [37].

2.2.1 Baculovirus

Originally derived from *Autographica californica* multiple nucleopolyhedrovirus, recombinant baculoviruses are highly effective at infecting insect cells used in IC-BEVS [38]. A wild-type baculovirus produces prodigious quantities of Polyhedrin protein in late-stage infection to protect baculovirus virions from the environment as well as p10 protein to prepare for host cell destabilization [39]. Recombinant genes can replace these proteins in genetically engineered baculoviruses, resulting in high yields of the desired protein upon infection [40].

2.3 Ultracentrifugation

Based on physical properties like density and shape, particles move through a medium at a given sedimentation rate when high centrifugal force is applied [41]. In conjunction with other analytical techniques, ultracentrifugation is commonly used to identify buoyant densities of particles in addition to separating them from other sample components [42]. VLPs must be purified of contaminants to validate and control effects on downstream work such as immunological testing, with ultracentrifugation playing a key role in this [43].

2.3.1 Cushion

Enveloped VLP production often involves harvest of supernatant from cell culture, in which VLPs typically exist in dilute conditions [44]. By layering a dense sucrose solution underneath supernatant and performing ultracentrifugation it is possible to force the VLPs into a solid pellet [45]. Other proteins, cell debris, and contaminants may be unable to pass through this dense medium, therefore semi-purification as well as concentration of VLPs may occur in one experimental step [45].

2.3.2 Gradient

To determine a VLP's approximate density, a discontinuous or continuous gradient may be formed by layering solutions of decreasing density atop one another [46, 47]. Upon sample loading and ultracentrifugation the VLP will migrate to the point at which the density of the medium is equal to its own density [46, 47]. The gradient can be fractionated and the density of the fraction containing the VLP assessed [46, 47]. An important consideration is that the osmotic pressure of the gradient may be greater than that of the medium the VLP was generated in, resulting in possible osmotic shrinkage or swelling of the VLP thus altering its apparent density [48]. This fact is the reason behind the popularity of iodixanol as a gradient forming medium, which is iso-osmotic compared to traditionally used gradient forming media such as sucrose or cesium chloride [48, 46, 47].

2.4 Dynamic Light Scattering

Multi-Angle Dynamic Light Scattering (MADLS) is an optical technique that can be used to determine size and concentration of particles in an aqueous sample [49, 50]. Since particles constantly collide and translate via Brownian motion, a laser beam shone at the sample will also vary in its scattering pattern [49, 50]. By measuring the speed at which the pattern changes, the diffusion coefficient for particles in the sample can be determined [49, 50]. This is related to the hydrodynamic diameter by the Stokes-Einstein-Sutherland equation, which is effectively the particle size in that medium [49, 50]. Since the intensity of scattered light will be scaled to the number of particles present, the concentration of particles can be determined [49, 50]. According to physics, smaller particles will diffuse faster than larger particles, making their contributions to light fluctuations faster and slower respectively [49, 50]. By layering this with knowledge that smaller and larger particles dominate certain angles of light scattering, backscatter and forward scatter respectively, multiple angles of detection allow a richer assessment of heterogenous particle populations [51]. This gives MADLS an advantage over single-angle DLS, which is critical in determining size and concentration of multiple particle types in one sample such as baculovirus virions and enveloped VLPs. It is worth noting that the spherical particle assumption of the Stokes-Einstein-Sutherland equation is violated by the rod-shaped baculovirus, and thus determination of these particles may be less accurate using this formula when compared

to the more spherical VLPs [49, 50].

It is critical to know the physical properties of the particle and medium before performing a MADLS experiment, since viscosity, refractive index, and absorption will all play a key role in determining the result [52, 53, 54]. Refractive index of the medium will affect scattering behaviour, while that of the particle will affect scattering intensity and contrast against the medium [53]. Viscosity of the medium will directly impact diffusion rate, which cascades to affect measurements of particle size and concentration [54]. Absorption of the particle will determine scattering intensity, which directly impacts concentration [52]. These values can be found readily in literature for widely studied particle types, however for certain types of medium it is not as trivial to find. In a VLP semi-purification workflow using a fractionated density gradient, each of the fractions will have different densities, viscosities, and refractive indices resulting in a requirement to recalibrate for all possible states of the medium.

2.5 State of Art of VLP characterization

Recent studies surrounding enveloped VLP characterization, focusing on HIV-derived VLPs and SARS-CoV-2 VLPs produced in IC-BEVS or mammalian culture are reviewed here. The VLP type examined and techniques/methods performed are noted, as well as com-

ments on the data, what it proves, and if it gives the reader confidence that a VLP is truly produced. Studies were rated qualitatively from very weak, weak, moderate, strong, and very strong. Across these works, characterization and proof of VLP formation are dependent on low-throughput and high-skill techniques, none of which can allow the authors to state with 100% certainty that a VLP is indeed being produced. Interestingly, the microscopy images supplied in some works as evidence of VLP existence [55, 56, 57] have a large enough field of view that one can observe presence of other particles of similar sizes to those noted as VLPs.

Table 2.1: Recent studies characterizing enveloped VLPs derived from HIV or SARS-CoV-2.

VLP Type	Methods	Comments	Proof of VLP	Reference
GAG-GFP-VLP	In-house fluorimetry, fluorescence microscopy, transmission electron microscopy (TEM), nanoparticle tracking analysis (NTA)	Several optical methods were used to determine fluorescence of entire samples and individual cells, quantifying GAG-GFP presence. TEM images show presence of VLP-sized particles similar in appearance to immature HIV-1 virions. NTA quantifies concentration of particles with a mode of 154 nm, ranging between 100 and 200 nm in size. This study demonstrates the presence of particles of the expected VLP size, in addition to fluorescence of the samples. This does not definitively prove that GAG-GFP-VLPs are produced, however given that GAG-GFP is unlikely to be cleaved due to the lack of viral protease in the construct, it is expected that GFP signal is linked to presence of GAG.	Strong	[31]

Continued on next page

VLP Type	Methods	Comments	Proof of VLP	Reference
HA/NA/GAG-GFP-VLP	Dot blot, Western blot (WB), single radial immunodiffusion, hemagglutination assay, TEM , flow virometry	Several immunochemical methods were used to determine protein identity and quantity. TEM images show presence of VLP-sized particles with a range of 100 – 150 nm similar in appearance to HIV-1 virions. Flow virometry quantifies fluorescent events attributed to GAG-GFP presence. This study demonstrates presence of particles of the expected VLP size. Immunochemical and optical analysis of tangential flow filtration retentate supported by co-migration of HA and GAG on a gradient suggests presence of a VLP.	Very Strong	[55]
GP120/GAG-VLP	Enzyme-linked immunosorbent assay (ELISA), WB, TEM	Immunochemical methods were used to determine protein identity and presence in certain fractions. ELISA demonstrates presence of multiple P24 proteins in particles. TEM shows presence of VLP-sized particles with a range of 100 – 120 nm, however image quality is low. This study demonstrates presence of particles of the expected VLP size, however post-fractionation, several fractions reactive to P24 ELISA are pooled. Since WB for GP120 and P24 takes place after pooling, it is possible that many particle subtypes containing P24 and not GP120 were included.	Strong	[58]

Continued on next page

VLP Type	Methods	Comments	Proof of VLP	Reference
GAG-VLP	ELISA	ELISA demonstrates the presence of multiple P24 proteins on particles. Baculovirus virions are unlikely to possess GAG proteins due to highly specific GAG self-assembly and envelop-derivation pathways.	Moderate	[37]
SARS-CoV-2 (S, E, M, N)	TEM, WB	WB shows co-migration of S and N on a gradient which suggest presence of VLP. TEM shows VLP-sized particles between 50 – 120 nm with visually evident "corona", supporting evidence of S presence on particles.	Very Strong	[59]
SARS-CoV-2 (S, E, M, N)	WB, ELISA, NTA, TEM	Several immunochemical methods were used to identify proteins and their presence in filtrate. NTA confirmed presence of VLP-sized particles ranging between 84 – 161 nm. TEM displayed particles within the size range with a visually evident "corona", confirming incorporation of S onto particles.	Very Strong	[60]
SARS-CoV-2 (S, E, M)	Dot blot, WB, TEM, ELISA	Several immunochemical methods were used to identify proteins and their presence in crude supernatant and gradient fractions. WB confirmed co-migration of S, E, and M, suggesting they exist on the same particle type. TEM displayed particles with a visually evident "corona", confirming incorporation of S onto particles.	Very Strong	[61]

Continued on next page

VLP Type	Methods	Comments	Proof of VLP	Reference
SARS-CoV-2 (S, E, M)	WB, TEM	WB indicated presence of co-migrated S, E, M, supporting that they exist on the same particle. TEM showed low quality image of particles with a barely discernable "corona", suggesting S was incorporated onto these particles.	Strong	[57]
SARS-CoV-2 (S, E, M)	WB, TEM, ELISA	WB indicated presence of co-migrated S trimers, GP64, and M, supporting that they are present on the same particle. Sandwich ELISA proved existence of a type of particle with both GP64 and Spike present on its surface. TEM showed an image of a particle with what may have been a "corona", suggesting S had been incorporated onto these particles.	Moderate	[62]

Chapter 3

Methods

3.1 Overall process

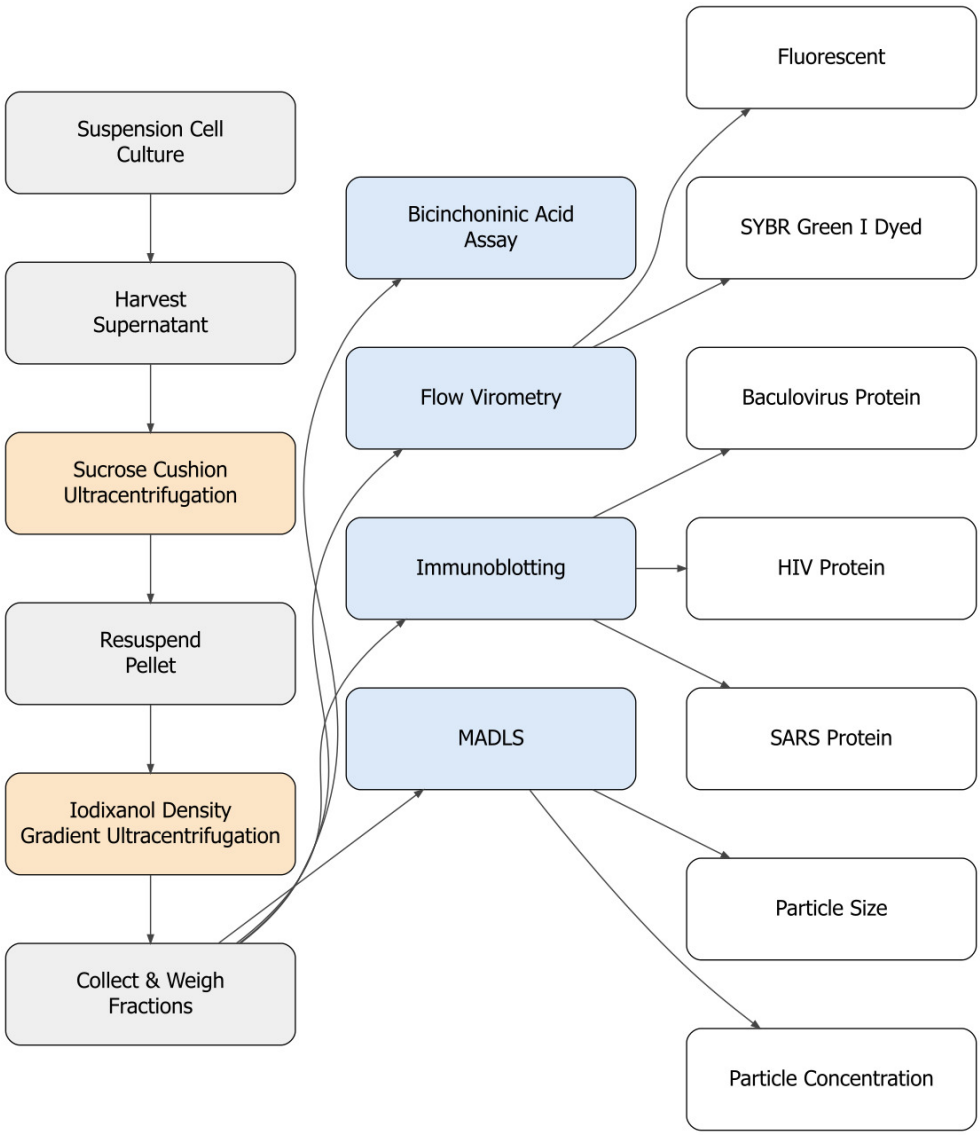

Figure 3.1: Flowchart of sequential experimental processes and analytical techniques. Sf9 insect cells were cultured in suspension, then infected or allowed to overgrow. Supernatant was harvested, semi-purified, and fractionated. Fractions were analyzed using a series of orthogonal methods to determine particle characteristics.

3.2 Cells and Viruses

Spodoptera frugiperda cell line 9 (Sf9), from the American Type Culture Collection (ATCC) was used. Vectors were previously generated by Dr. Mark Bruder using the *flash*BACGOLD ™ (Oxford Expression Technologies Ltd., Oxford UK) and Escort IV transfection reagent (Sigma Aldrich) [63]. Four different baculoviruses were used in this study 3.1.

Table 3.1: Description of recombinant baculovirus vectors used in this study.

Vector	**Description**
rBEV-p10mKOκ	Recombinant baculovirus designed to express an orange fluorescent protein, mKusabira-Orange-κ (mKOκ)
rBEV-GAG	Recombinant baculovirus designed to express group-specific antigen (GAG), a human immunodeficiency virus (HIV) polyprotein that is composed of several structural proteins: Matrix (MA), Capsid (CA), and Nucleocapsid (NC)
rBEV-GAG-GFP	Recombinant baculovirus designed to express green fluorescent protein fused to the GAG polyprotein (GAG-GFP)
rBEV-SARS-VLP	Recombinant baculovirus designed to express SARS structural proteins Spike (S), Envelope (E), and Membrane (M)

3.3 Insect Cell Culture and Maintenance

Sf9 cells were cultured in suspension using SF900-III Serum-Free Media (Gibco) in a shaking incubator at 27°C and approximately 120 rpm. Seeding densities of 0.4 or 0.6 x 10^6

cells/mL in 30 mL total volume in an autoclaved 125 mL Erlenmeyer flask required passaging every 3 or 2 days respectively, when cells reached between 2 - 3 x 10^6 cells/mL. Culture viability and density were monitored via trypan blue staining and analysis with the Countess II Automated Cell Counter (Thermo Fisher Scientific).

3.4 Virus Amplification

Each of the four aforementioned rBEVs used in this project were derived from previously titered P1 stocks. Each rBEV stock was amplified to a P2 working stock by infecting Sf9 cell cultures (2 x 10^6 cells/mL) at a multiplicity of infection (MOI) of 0.1. 72 hours post-infection (HPI), the cell culture was harvested via centrifugation at 1200 x g for 10 minutes. Supernatant was decanted into a test tube and stored at 4°C.

3.5 Infectious Virus Titering

Titering of amplified rBEV stocks was achieved by using the end-point dilution assay (EPDA) technique. Sf9 cells were designed in-house by a former student to express monomeric Azami-Green (mAG), a GFP, when infected by baculovirus [63]. Upon infection of these cells by a baculovirus, fluorescence can be observed under a fluorescence microscope. The EPDA technique involves seeding these cells in a 96-well microplate at

1.5 x 10^6 cells/mL, followed by adding serially diluted baculovirus to each row, from least dilute (10^{-4}) to most dilute (10^{-10}), with an uninfected control row. After incubation at 27°C for 7 days, fluorescence is scored according to a binary system of fluorescence or no fluorescence observed in a given well. This data can be used to calculate the titer of the baculovirus.

3.6 Recombinant Protein/VLP Production

To produce a recombinant product, titered P2 stocks were used to infect Sf9 cell cultures (2 x 10^6 cells/mL) at a MOI of 3. Cell viability and density was assessed every 24 HPI, and at 72 HPI, the cell culture was harvested via centrifugation at 1200 x g for 10 minutes. The supernatant was decanted into individual sealable centrifuge tubes for each biological replicate and stored at 4°C.

3.7 Flow Virometry

Flow virometry used a 530 nm laser beam to probe individual particles in a fluidics system, gaining insight into particle characteristics based on the perturbations of scattered light. The BD Accuri C6 Plus Flow Cytometer (BD Biosciences) was used to quantify populations of fluorescent and stained particles. Flow cytometry analysis was performed using the

FlowJo® V10 software (FlowJo LLC, Ashland, OR) by plotting side scatter - height (SSC-H) against filter 1 - height (FL1-H) on logarithmic scales. Pre-analysis calibration was performed using Flowset CS&T RUO beads (BD Biosciences) in PBS at an approximately concentration of 1 x 10^6/mL.

3.7.1 Total Virus Particle Count via SYBR Green Staining

The amount of DNA-containing particles in a given sample was determined using SYBR Green I Nucleic Acid Stain (Thermo Fisher Scientific). Samples were diluted in PBS to an initial dilution of (1 or 3 or 9) x 10^{-2} and through the protocol, came to a final dilution of (1 or 3 or 9) x 10^{-3}. Following initial dilution, samples were fixed with 2% paraformaldehyde at 4°C for 1 hour, frozen at -80°C for 30 min, thawed in a 30°C water bath for 10 mins, and permeabilized with 10% Triton X-100 for 5 min. After being stained with diluted SYBR Green I (5 x10^{-3}), samples were incubated in a water bath at 80°C for 10 min in total darkness, before being placed on ice and allowed to cool for 10 minutes prior to being transferred into sample tubes for analysis by flow virometry. The flow cytometer, which was set to a flow rate of 35 μL/min with a 30 sec run limit, performed automated sampling. Blank solutions of PBS containing paraformaldehyde, Triton X-100, and SYBR Green I at final concentrations were subject to sample preparation procedures and used as baseline signal when gates were applied to all samples during analysis.

3.7.2 Fluorescent Virus-Like Particle Count

Particles which were fluorescent by design, GAG-GFP-VLPs, were additionally analyzed by flow virometry after direct dilution. In a microplate, samples were diluted with PBS to a total dilution of (1 or 3 or 9) x 10^{-3} and analyzed using the same machine parameters as those of section 3.7.1. This allows the visualization of populations of fluorescent GAG-GFP-VLPs without interference of SYBR Green I dye. Blank solutions of PBS were used as baseline signal when gates were applied to all samples during analysis.

3.7.3 Accounting for Fluorescent Virus-Particle Count in SYBR Green I Staining Protocol

In order to account for unstained GAG-GFP fluorescence contributing to the total signal in SYBR stained samples, an appropriate control measure was implemented. For each sample that was SYBR stained, a replicate was created by performing the same staining protocol (as in section 3.7.1) except for the addition of SYBR Green I dye, which was replaced by PBS in the replicate to maintain an equivalent dilution. In the unstained replicate, any fluorescent signal exhibited by the sample can be attributed to the expected fluorescence of GAG-GFP that remains after potential quenching by other components in the protocol (paraformaldehyde, Triton X-100, heating). This signal can be subtracted from the signal

of the same sample that underwent the complete SYBR protocol, this yields the exclusive signal contribution from the SYBR stained particles in the sample.

3.8 Dot blotting

For each biological replicate of SARS-VLP (A, B, C), a dot blot protocol was performed to detect Spike protein abundance. 2 μL of sample (infected cell culture supernatant, fractions 1 – 6, pellet from sucrose gradient ultracentrifugation) was spotted on a nitrocellulose membrane (Bio-Rad). Membranes were air dried at room temperature (RT) for 15 min prior to blocking with 5% milk TBS-T on a rocking platform for 1 hr at RT.

Membranes were thrice washed with 1 X TBS-T, rocking for 10 min at RT each time. Membranes were incubated with 1:1000 HRP-conjugated anti-Spike antibody (Novus Biologicals) in 5% milk TBS-T, rocking at RT for 1 hr. Membranes were once again thrice washed with 1 X TBS-T, rocking for 10 min at RT each time. Membranes were exposed to 1-Step Ultra TMB Blot reagent (ThermoFisher Scientific) for 20 min at RT.

The "universal" setting on an iBright FL1500 imaging system (ThermoFisher Scientific) was performed for colorimetric detection. Dot intensity was analyzed using the ImageJ online image analysis software version 1.54r September 2025 (NIH).

3.9 SDS-PAGE and Western blotting

All four infected samples, herein referred to as p10mKOκ SARS-VLP, GAG-VLP, and GAG-GFP were examined through SDS-PAGE and Western blot analysis. A sample created by equivolumetrically pooling SARS-VLP, GAG-VLP, and GAG-GFP supernatant was used as a positive control. Polyacrylamide gels were cast within 1.5 mm glass plates, a 10 well comb, and the Bio-Rad gel casting stand. Reagents "A" and "B" were used along with TEMED and 10% ammonium persulfate (APS) as per the manufacturer's instructions to cast gels, which were stored overnight under high humidity at 4°C.

25 μL of each sample (Fractions 1-6 and the equivolumetric infected cell culture supernatant mixture) was heated to 95° C with 8 μL of 4 x Laemmli buffer. 25 μL of mixture (in addition to unstained Precision Plus Protein™molecular weight ladder (Bio-Rad)) was loaded into wells in the mounted gels, and electrophoresis was conducted in the mini-PROTEAN system (Bio-Rad) by stacking for 20 min at 80 V, followed by resolving for 1h 15 min at 120 V. Dye front was observed to reach 1 cm from the bottom of the gel.

Gels were removed from cassettes and imaged as stain-free gels on the ChemiDoc Touch imaging system (Bio-Rad). A polyvinylidene difluoride (PVDF) membrane was pre-wetted in 100% methanol for 10 min to enhance hydrophilicity. Gels were carefully placed on PVDF membranes and sandwiched between thick blot paper before being loaded into the

Trans-Blot Turbo Transfer system (Bio-Rad) in alignment with the flow of electrical current based on the manufacturer's instructions. Protein transfer was performed at 25 V for 7 minutes, after which the membranes were imaged in the ChemiDoc Touch imaging system (Bio-Rad) as blots to confirm protein transfer.

Membranes were blocked with 5% milk TBS-T for 1 hr at RT on a rocker platform, rinsed thrice with TBS-T for 10 min each. Membranes were then incubated overnight on the rocker at 4°C in primary antibody solution composed of 1:1000 mouse anti-GP64 antibody (Thermo Fisher Scientific) in 5% milk TBS-T. After washing thrice with TBS-T as described prior, membranes were incubated for 1 hr at 4°C on the rocker in 1:3000 goat anti-mouse antibody with horseradish peroxidase (HRP) conjugate (Thermo Fisher Scientific) in 5% milk TBS-T.

After washing thrice with TBS-T as described prior, membranes were incubated at RT with chemiluminescent substrate Western ECL Substrate (Bio-Rad) for 5 minutes. Membranes were imaged in the ChemiDoc Touch imaging system (Bio-Rad) as chemiluminescent blots to visualize GP64 protein banding.

The membrane corresponding to p10mKOκ was then washed thrice in TBS-T and left to dry at RT overnight for future analysis. All other membranes underwent a "stripping" protocol to remove bound antibodies from blotted proteins, enabling re-probing with different antibodies. In accordance with the Thermo Fisher Mild Acid Stripping Buffer protocol,

stripping buffer was made which composed of 15 g glycine, 1 g SDS, 10 mL Tween 20, made up to a total volume of 1 L using DI water, after pH adjustment with HCl to 2.2. Membranes were washed thrice with TBS-T to remove excess chemiluminescent substrate, then incubated protein-side up on a rocker at RT with the stripping buffer for 20 min. Membranes were washed thrice with TBS-T, then re-blocked with 5% milk TBS-T on a rocker at 4°C for 1 hr.

Membranes corresponding to GAG-GFP and GAG-VLP were incubated overnight on the rocker at 4°C in primary antibody solution composed of 1:1000 mouse anti-P24 antibody (Thermo Fisher) in 5% milk TBS-T. The membrane corresponding to SARS-VLP was incubated overnight on the rocker at 4°C in primary antibody solution composed of 1:1000 rabbit anti-Spike antibody conjugated to HRP (Novus Biologicals) in 5% milk TBS-T.

The following morning, all membranes were washed thrice with TBS-T. The membrane corresponding to SARS-VLP was incubated with chemiluminescent substrate for 5 mins prior to being imaged as described for prior Western blots. It was then washed thrice in TBS-T and let dry for future analysis. The remaining membranes were incubated for 1 hr on the rocker at 4°C in secondary antibody solution composed of 1:3000 goat anti-mouse antibody (Thermo Fisher) in 5% milk TBS-T. Membranes were washed thrice in TBS-T and incubated with chemiluminescent substrate for 5 min prior to being imaged as described prior.

3.10 BCA Assay

To quantify the total amount of protein present in each of the fractions of semi-purified samples, a BCA assay was performed. To accommodate 3 technical replicates of each fraction, having 9 fractions per biological replicate, and 3 biological replicates per virus type, a high-throughput method was chosen by leveraging 96-well microplates. Utilizing the Pierce BCA Protein Assay Kit (Thermo Fisher Scientific) and accompanying manufacturer's instructions, working reagent and BSA standards (in 1 X NTC) were prepared fresh. For all samples and BSA standards, 25 μL was introduced to individual microplate wells in triplicate. 200 μL working reagent was added to each well using a multichannel pipette and mixed with samples, this was done rapidly to ensure that lag time in between technical replicates was minimized. Plates were incubated for 37° C for 30 min and equilibrated to RT for 5 min. Using a Varioskan LUX microplate reader (Thermo Fisher Scientific), absorbance was recorded at 562 nm. A standard curve was constructed from values obtained from blank-corrected BSA standards, which was then used to determine protein concentration.

3.11 Multi-Angle Dynamic Light Scattering

To assess size and concentration,a Malvern Zetasizer Ultra red device, and DTS0012 polystyrene cuvettes were used. Measurement settings of "Size", "MADLS", and "Particle Concentration" were used.

Factory-fresh DTS0012 cuvettes were washed with DI H2O and soap. They were rinsed for 1 min with a narrow beam of water to ensured no soap remained. Each cuvette was then soaked in 1 X NTC overnight to remove any excess particles. On experiment day, cuvettes were rinsed with 1 X NTC and allowed to air dry upside-down for 30 mins. The zetasizer was turned on and allowed to warm up for 20 min. Each cuvette was assigned a fraction, which was then used for that specific fraction number throughout this project. Once dry, cuvettes were loaded with 1 mL of fraction sample, stopper secured on the cuvette mouth, and placed in the sample chamber of the zetasizer. After 2 min of equilibration, a given measurement setting protocol was initiated. Contextually, 10 sequential repeat measurements were performed using the "Particle concentration" setting. Results were corrected for physical parameters (see C.2 for refractive index and C.3 for viscosity calibration curves) of individual fractions by leveraging the zetasizer's onboard ZS Xplorer software to edit sample properties, and various particle populations were visualized based on peak particle hydrodynamic radius, and corresponding concentration. After every measurement cuvettes were removed from the sample chamber, sample was removed from

the cuvette and stored in microtubes for further use, and 10% bleach in DI water was added to each cuvette to remove excess biologicals, and allowed to sit overnight. The following day, cuvettes were emptied and rinsed with a narrow beam of DI water for 1 min each, followed by thrice rinsing with 1 X NTC before being inverted and allowed to air-dry.

3.12 Sucrose Cushion Ultracentrifugation

To remove excess debris and perform a pre-purification cleaning of VLPs, a sucrose cushion ultracentrifugation was performed. A 25% (w/v) sucrose solution in 1 X NTC was made fresh, and passed through a 0.22 μm sterile filter. Briefly 5 mL of infected cell culture supernatant was added to a 13.2 mL thin-wall polypropylene ultracentrifuge tube (Beckman Coulter), and 1.5 mL of sucrose solution was layered underneath this via pipette snorkelling. The remaining 5 mL of VLP supernatant was added slowly to the top of the sample to reduce possible disturbance of the sucrose cushion. 14 tubes were constructed in this manner, corresponding to a certain biological replicate (A, B, or C) of each of the four viruses being investigated, and two replicates of uninfected Sf9 cell culture supernatants to act as negative controls. After careful balancing to $<$ 1 mg difference in mass of opposite buckets in a SW 41TI swinging bucket rotor (Beckman Coulter) the rotor was loaded into an Optima XPN-100 floor-ultracentrifuge (Beckman Coulter). Set to 26,000 rpm at 4°

C for 1.5 hr, samples were pelleted through the sucrose cushion, experiencing an average force of 83,300 x g. Supernatant was removed, and pellets were soaked in 2.1 mL 1 X NTC for 20 min while kept in the ultracentrifuge tubes on ice. Pellets were pipetted gently to resuspend in 1 X NTC and remained in the original ultracentrifuge tubes at 4° C overnight. The following day, 100 μL of each pellet was taken for further analysis.

3.13 Iodixanol Gradient Ultracentrifugation

To resolve VLPs, baculoviruses, and any remaining impurities post-sucrose cushion purification, particles were separated into isopycnic groupings via iodixanol gradient ultracentrifugation. Iodixanol solutions of 10, 20, 30, 40, 50% iodixanol in 1 X NTC were made fresh by diluting 60% iodixanol solution Optiprep (Stemcell Technologies). These were passed through a 0.22 μm sterile filter before being weighed to determine mass and subsequently density. 1.5 mL of each of the six solutions was gently overlaid, from most dense to least dense in a 13.2 mL thin-wall polypropylene ultracentrifuge tube (Beckman Coulter). This was covered with parafilm and allowed to sit overnight at 4°C, in order to form a continuous density gradient. The following day 2 mL of resuspended pellet was gently overlaid at the top of the tube. This process was performed for each virus replicate and two uninfected Sf9 cell culture controls, for a total of 14 gradients. After careful balancing

to < 1 mg difference in mass of opposite buckets in a SW 41 TI swinging bucket rotor (Beckman Coulter) the rotor was loaded into an Optima XPN-100 floor-ultracentrifuge (Beckman Coulter). Set to 35,000 rpm at 4° C for 2.5 hr experiencing an average force of 151,000 x g, particles migrated to their isopycnic point in the density gradient. Density gradients were removed from the buckets and placed in a fixed tube holder in preparation for fractionation.

3.13.1 Iodixanol Gradient Ultracentrifugation Fraction Collection

After particles were separated via density gradient ultracentrifugation, nine fractions of 1.2 mL each were withdrawn from every ultracentrifuge tube. This allows analysis of particles corresponding to the density of each fraction, without sample convolution from particles of different densities. Since the density gradient would become difficult to visualize after ultracentrifugation, ultracentrifuge tubes had been marked prior to use at various points corresponding to 1.2 mL of volume drawn between two points. Fractions were taken by piercing the tube with a 21 G BD PrecisionGlide needle (Beckton Dickinson) at these points, and with the bevel facing upward in the center of the tube 1.2 mL of solution was drawn into a 3 mL Luer Lock syringe (Beckton Dickinson). This was done for each of fractions one through eight, which were then ejected into 1.5 mL microcentrifuge tubes for storage. Fraction 9 was drawn by pipetting the remaining solution in the bottom of

the ultracentrifuge tube up and down 30 times to dislodge any pellet that may have been formed prior to being collected in a microcentrifuge tube.

3.13.2 Density of Iodixanol Gradient Ultracentrifugation Fractions

In order to assess the density of each fraction, 1.5 mL microcentrifuge tubes were pre-weighed on a calibrated analytical balance. Fractions were removed from storage at 4°C and allowed to equilibrate to room temperature, which was recorded prior to further measurement, before being vortexed for 20 s each to ensure homogeneity. A calibrated pipette was used to extract 1000 μL of fraction from a storage microcentrifuge tube, and eject it into a pre-weighed microcentrifuge tube. This tube was weighed on the analytical balance and the total mass recorded, this was done for each sample. The mass of the tube was subtracted from the total mass, allowing the determination of density in g/mL for each sample.

3.14 Rheometry of Iodixanol Solutions

Iodixanol-NTC solutions of 5% increases were created, from 5% to 55% iodixanol, while pure 1 X NTC was used as "0%" and undiluted Optiprep ™ was used as "60%". Each solution was equilibrated to 25°C, with 1 mL being transferred into a pre-weighed microcentrifuge

tube and re-weighed. Density of each solution in grams per milliliter was obtained by subtracting tube mass from total mass. Each solution was made in triplicate, with each replicate having density determined. An MCR 702e rheometer (Anton Paar) was fitted with a glass parallel plate and used to measure the viscosity of the solution. After the instrument had been initialized and calibrated, 170 μL of the solution was loaded onto sample platform. A gap of 0.25 mm was set and the plate lowered, excess solution was trimmed and the rheometer was set to collect 600 measurements at equal intervals over a 5 minute period. After the run was complete, data was saved, the sample platform cleaned and reset for the following solution. Triplicate solutions were run once each, generating an oscillatory value for viscosity based on shear rate, shear stress, and torque. The final 100 measurements were averaged to determine the final value of viscosity for that solution. An average value was determined between replicates and plotted against average density of the solution to extract a fourth-order polynomial line of best fit. This model was used to determine the viscosity (mPa*s) of a given fraction based on its measured density.

3.15 Refractometry of Iodixanol Solutions

Iodixanol-NTC solutions of 5% increases were created, from 5% to 55% iodixanol, while pure 1 X NTC was used as "0%" and undiluted Optiprep ™ was used as "60%" solutions.

Each solution was equilibrated to 24°C, with 1 mL being transferred into a pre-weighed microcentrifuge tube and re-weighed. Density of each solution in grams per milliliter was obtained by subtracting tube mass from total mass. A handheld refractometer (Aichose) was calibrated using ultrapure water (resistivity of 18.2 MΩ, total organic carbon 3 ppb) as a zero measurement. 100 μL of a given iodixanol-NTC solution was placed on the prism and the flap closed. Held perpendicular to the light source, a degrees Brix value was obtained by readout of the internal scale. This was converted to refractive index using a sucrose conversion table (USDA Technical Manual) and recorded. The prism was then rinsed with DI water and dried with a clean cloth. This was repeated in triplicate for each solution. An average value was determined between replicates and plotted against average density of the solution to extract a linear best fit model. This model was used to determine the refractive index (unitless) of a given fraction based on its measured density.

Chapter 4

Results

The experimental design emphasized both biological and technical replication, with three independent cell cultures and infections for each of the four virus types, and one independent culture for upper and lower viability bounds of uninfected samples. Each independent sample was semi-purified and separated into 9 fractions, each of which was analyzed in technical triplicate for each established quantitative methodology (BCA assays and flow virometry measurements). Western blots were run on one biological replicate of each virus type, and dot blots were run on all three biological replicates of SARS-VLP. The results of immunoblotting methodologies are for the sole purpose of qualitative observations, since the replication of such low-throughput techniques would not provide sufficient value for the effort expended. Multi-angle dynamic light scattering techniques were performed using 10

sequential measurements on each independent fraction, and comparison to flow virometry methods are expressed as correlation coefficients. Thus, reported trends that hold true across independent cultures provide more robust insights than single-production studies.

4.1 Cell culture and harvest

4.1.1 Growth Curves

3 flasks were infected for each recombinant baculovirus, rBEV-mKOκ, rBEV-GAG, rBEV-GAG-GFP, or rBEV-SARS, for a total of 12 flasks. 2 additional flasks were left uninfected and without passaging until 54% and 74% viabilities were reached for total cell concentrations of $12.8*10^6$ cells/mL and $13.1*10^6$ cells/mL at 432 and 336 hours respectively (Figure 4.1). For infected samples, cell viability and concentration was determined in intervals of 24 HPI up to 72 HPI, when viral supernatant harvest occurred (Figure 4.2).

Total concentration of viable cells was shown to increase to a maximum at 24 HPI, then drop by 48 HPI for all samples (Figure 4.3). A subsequent drop in viable cell concentration at 72 HPI for all samples with the exception of Sf9 cells infected by rBEV-GAG-GFP suggests that rBEV infection was successful and products of infection are likely present in viral supernatant. Despite the deviation from the expected viability decrease at 72 HPI, cultures infected with rBEV-GAG-GFP appeared greenish in colour. This is consistent with prior

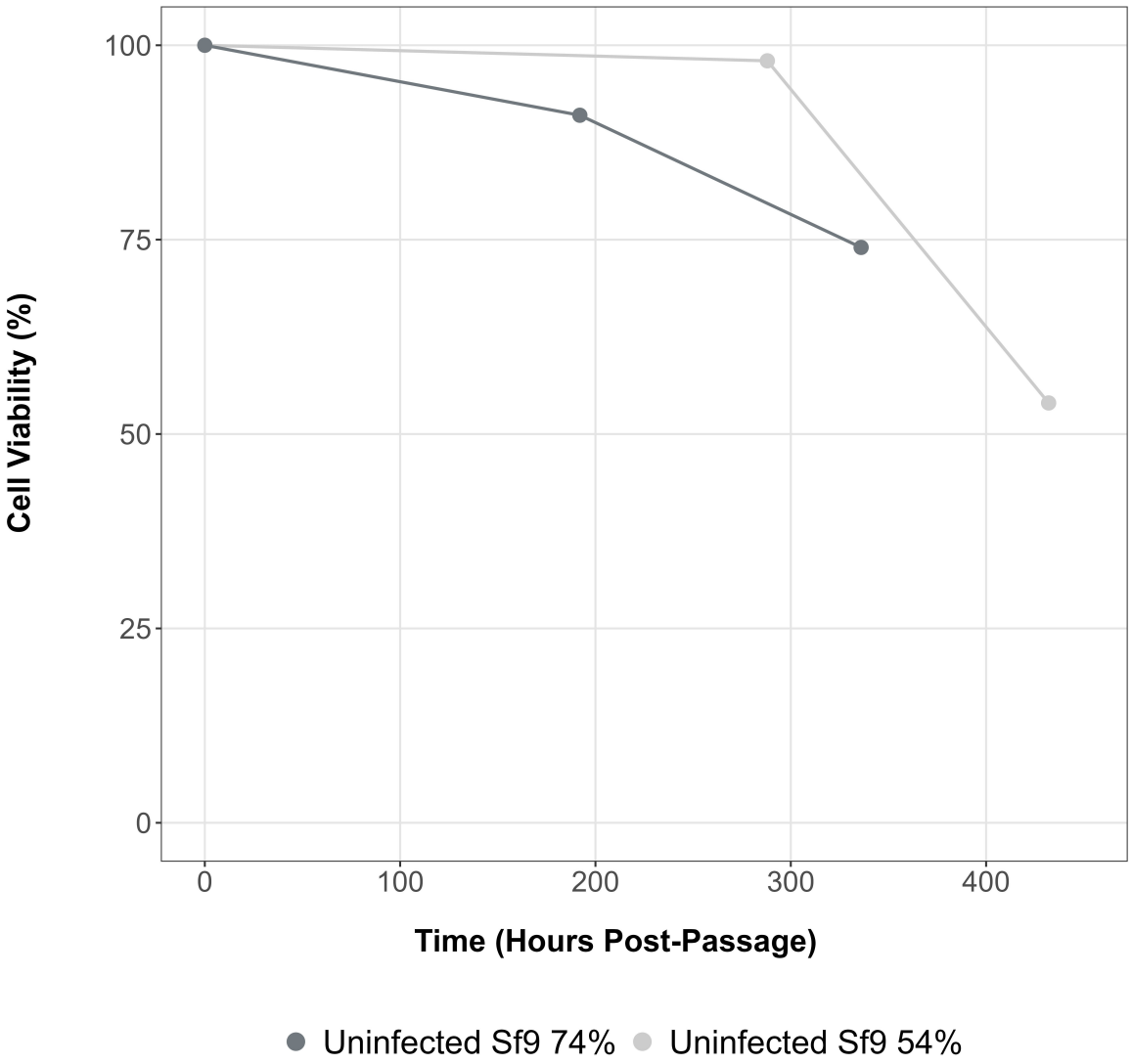

Figure 4.1: Viability curves of Sf9 cells cultured without passaging until a given viability was reached. Cell viability was determined at 192 and 336 or 288 and 432 hours post-passaging for samples cultured to 74% (dark grey) and 54% (light grey) respectively. Single replicates were produced for each viability.

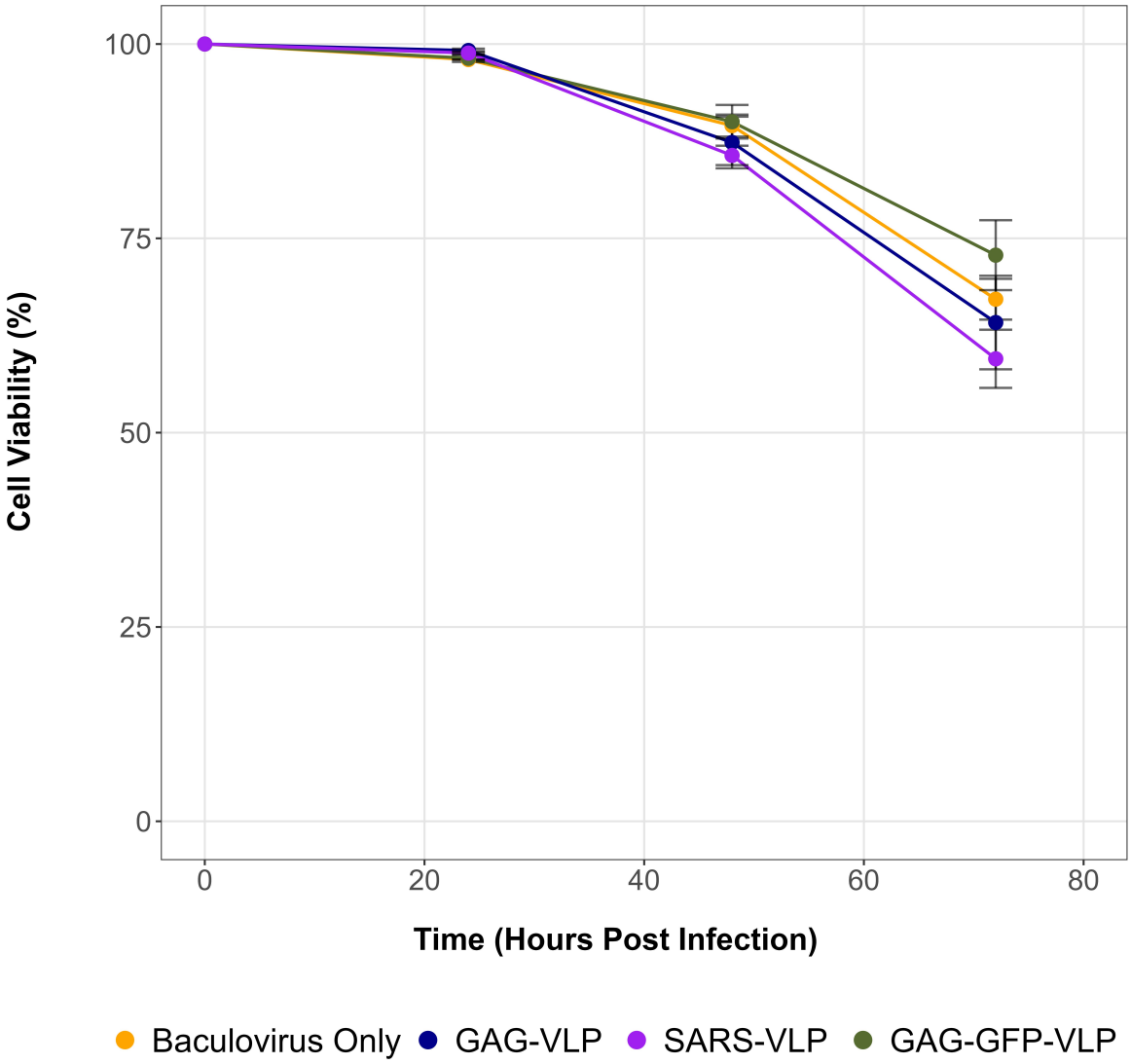

Figure 4.2: Viability curves of Sf9 cells post-infection with a given recombinant baculovirus. Cell Viability was determined at 24, 48, and 72 HPI. Baculovirus Only / rBEV-mKOκ (orange), GAG-VLP (blue), GAG-GFP-VLP (green), SARS-VLP (purple). Error bars represent range of biological triplicates.

qualitative observations of GFP expression and provides support to the claim that GFP proteins were produced and GAG-GFP-VLP products were present in supernatant.

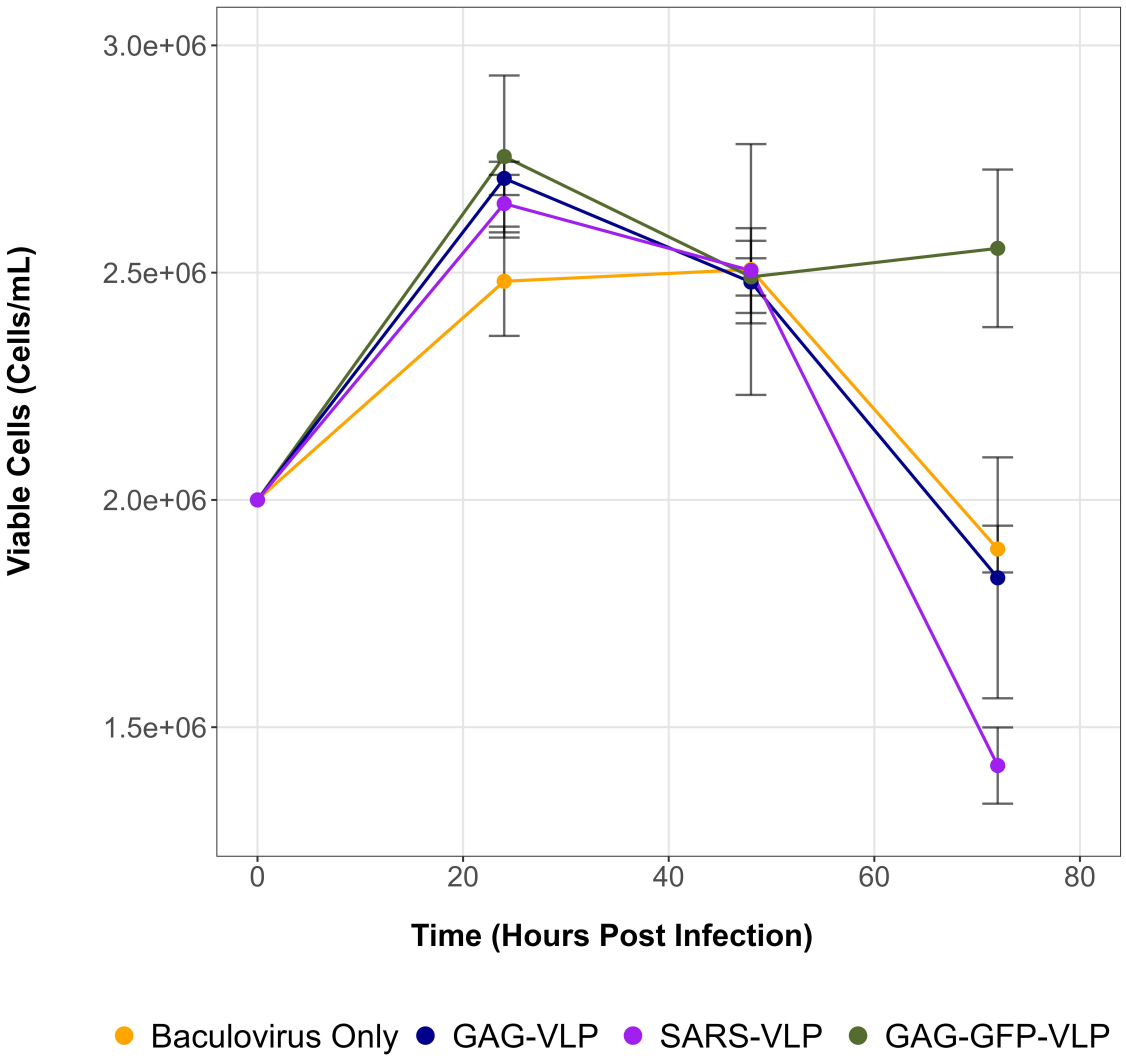

Figure 4.3: Growth curves of viable Sf9 cells post-infection with a given recombinant baculovirus. Cell concentration and viability were determined at 24, 48, and 72 HPI. Baculovirus Only / rBEV-mKOκ (orange), GAG-VLP (blue), GAG-GFP-VLP (green), SARS-VLP (purple). Error bars represent range of biological triplicates.

4.2 Ultracentrifugation Fraction Characterization

Material resuspended from pelleting through a sucrose cushion was further subject to iodixanol gradient ultracentrifugation. Fractions were then collected and characterized.

4.2.1 Fraction Density

Following ultracentrifugation, fractions were collected and weighed to obtain the density of the fractions collected. Densities of each fraction were found to be similar with the exception of the densities of uninfected Sf9 samples (Figure 4.4). After fraction 2, densities of the uninfected Sf9 fractions are lower than the infected counterparts. Despite this, the obvious similarity allows direct comparison between fractions of identical numbers between samples.

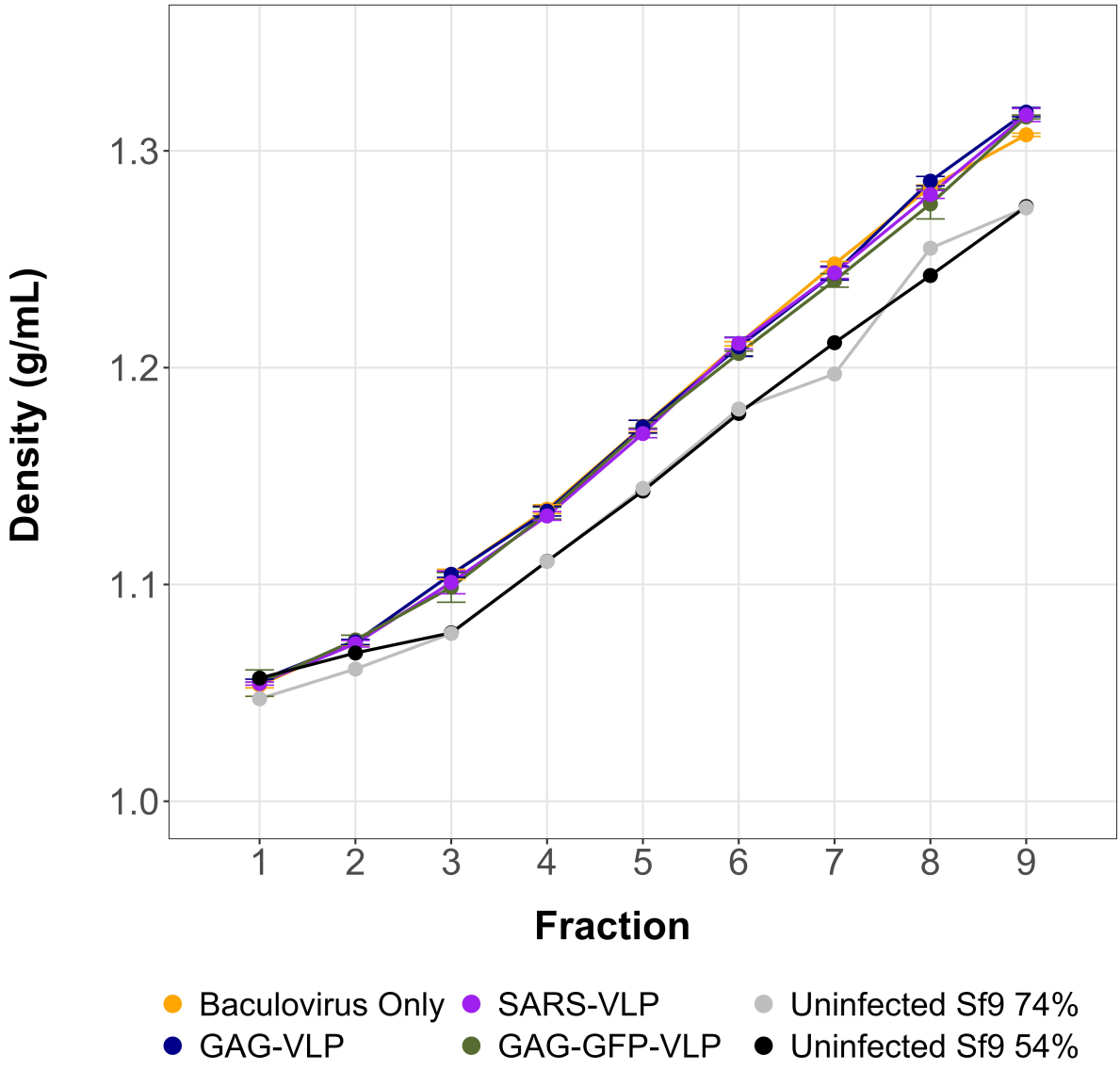

Figure 4.4: Density of semi-purified samples. Uninfected Sf9 supernatant at 54% viability (black), 74% viability (grey), Baculovirus Only / rBEV-mKOκ (orange), GAG-VLP (blue), GAG-GFP-VLP (green), SARS-VLP (purple). Error bars represent biological replicates.

4.2.2 Total Protein Content

Total protein concentration decreased with increasing fraction density. The highest concentrations present in fractions 1 and 2 (Figure 4.5). Beyond fraction 6 (approximate density 1.21 g/mL) protein concentration remained relatively constant at or below 50 μg/mL. This suggests that proteins are found mostly in less dense fractions, and possibly some that are pelleted have become re-suspended in the most dense fraction. This could further suggest that particles containing proteins are found at greater proportions in less dense fractions.

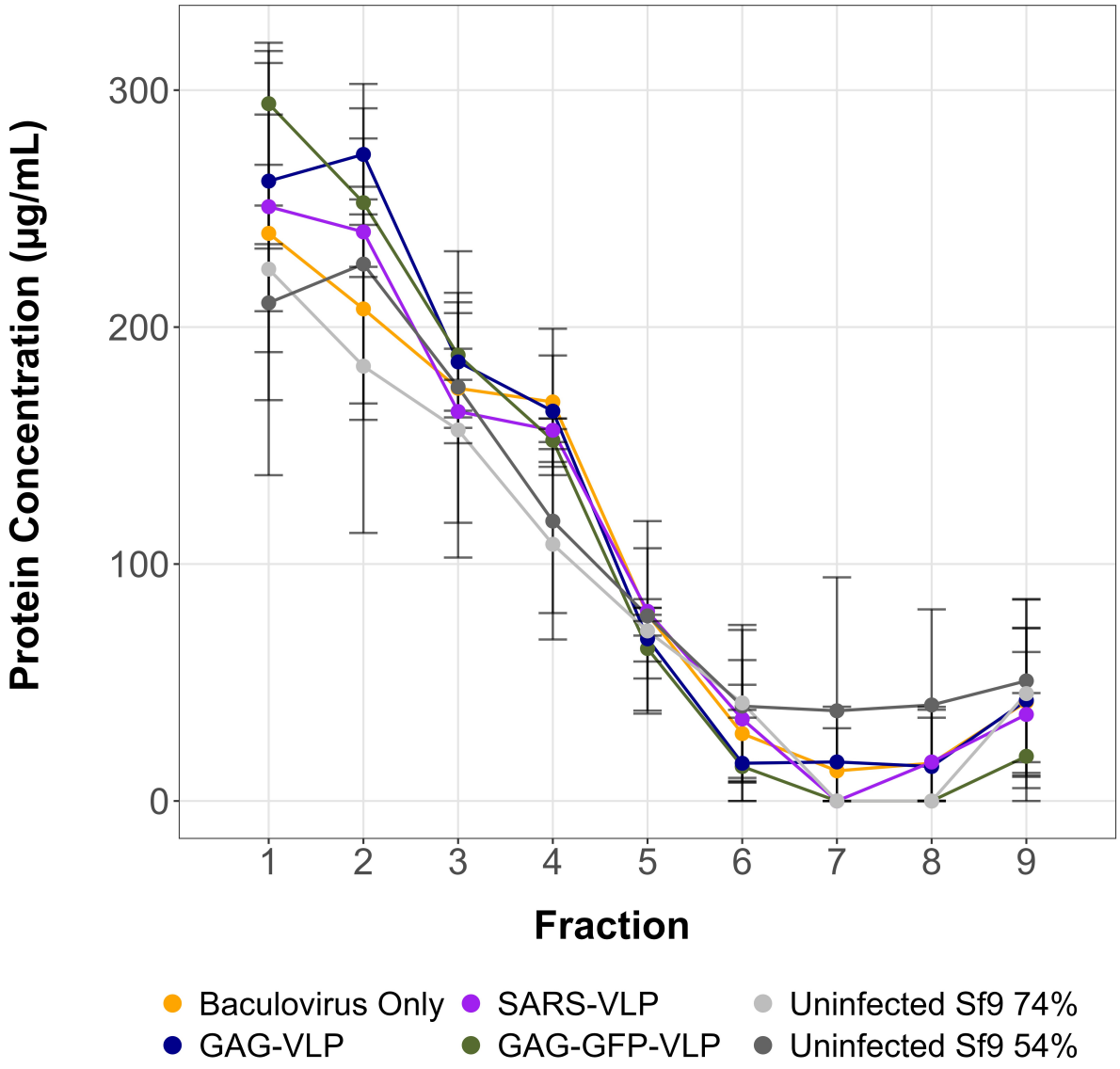

Figure 4.5: Total protein content in semi-purified samples of cell culture supernatant. Uninfected Sf9 supernatant at 54% (black), 74% (grey), Baculovirus Only / rBEV-mKOκ (orange), GAG-VLP (blue), GAG-GFP-VLP (green), SARS-VLP (purple). Error bars represent biological triplicates.

4.2.3 Flow Virometry

A flow cytometer has been used to detect fluorescent virus (through DNA staining) and virus-like particles (fluorescent protein fused to the *GAG* gene).

SYBR-Green I DNA Staining

Flow virometry was performed to assess the concentration of SYBR Green I stained DNA-containing particles of all semi-purified samples. Similarly fluorescence flow virometry was used to determine concentration of fluorescent particles in semi-purified GAG-VLP and GAG-GFP-VLP samples.

Semi-purified fractions of infected samples show similar distribution trends of DNA-containing particles, spanning fractions 2 - 5 with peak particle concentration occurring in fraction 4 (Figure 4.6). This suggests that the majority of baculovirus virions are present between fractions 2 - 5 for each semi-purified sample. It is also of note that the concentration of DNA-containing particles in GAG-GFP-VLP samples appears to be decreased relative to other infected samples, which could indicate a decreased allocation of baculovirus-producing host cell proteins.

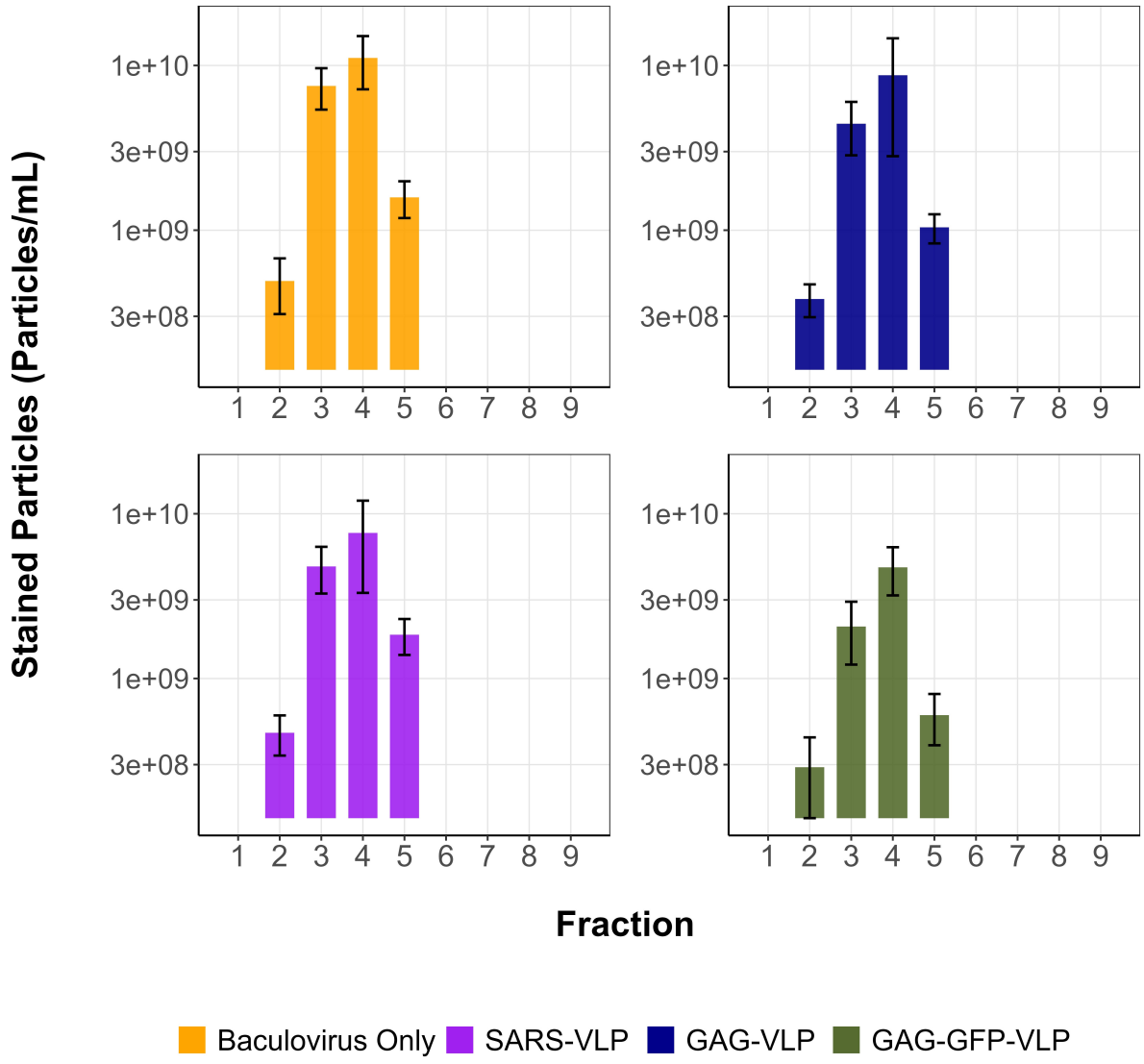

Figure 4.6: Flow virometry-derived dsDNA-containing particle concentration in semi-purified samples. Baculovirus Only / rBEV-mKOκ (orange), GAG-VLP (blue), GAG-GFP-VLP (green), SARS-VLP (purple). Samples stained with SYBR Green I dye to detect dsDNA-containing particles. Uninfected Sf9 supernatant samples below instrument LOD ($1.5 * 10^8$ Particles/mL) not shown. Error bars represent biological triplicates.

Comparison of stained particle profile and naturally fluorescent particle profile

Analysis of fluorescent particles within GAG-VLP shows no discernible signal as expected, and fluorescent particles in GAG-GFP-VLP show similar confinement to fractions 2 - 5 (Figure 4.7). The proportion of fluorescent particles within GAG-GFP-VLP fractions however, is dissimilar to that of DNA-containing particles, with peak particle concentration occurring in fraction 3. This suggests that the fluorescence flow virometry analysis functions as intended and that fluorescent particles are not identical to DNA-containing particles. These results further suggest that fluorescent particles are less dense on average than DNA-containing particles, however there may be significant overlap between density ranges.

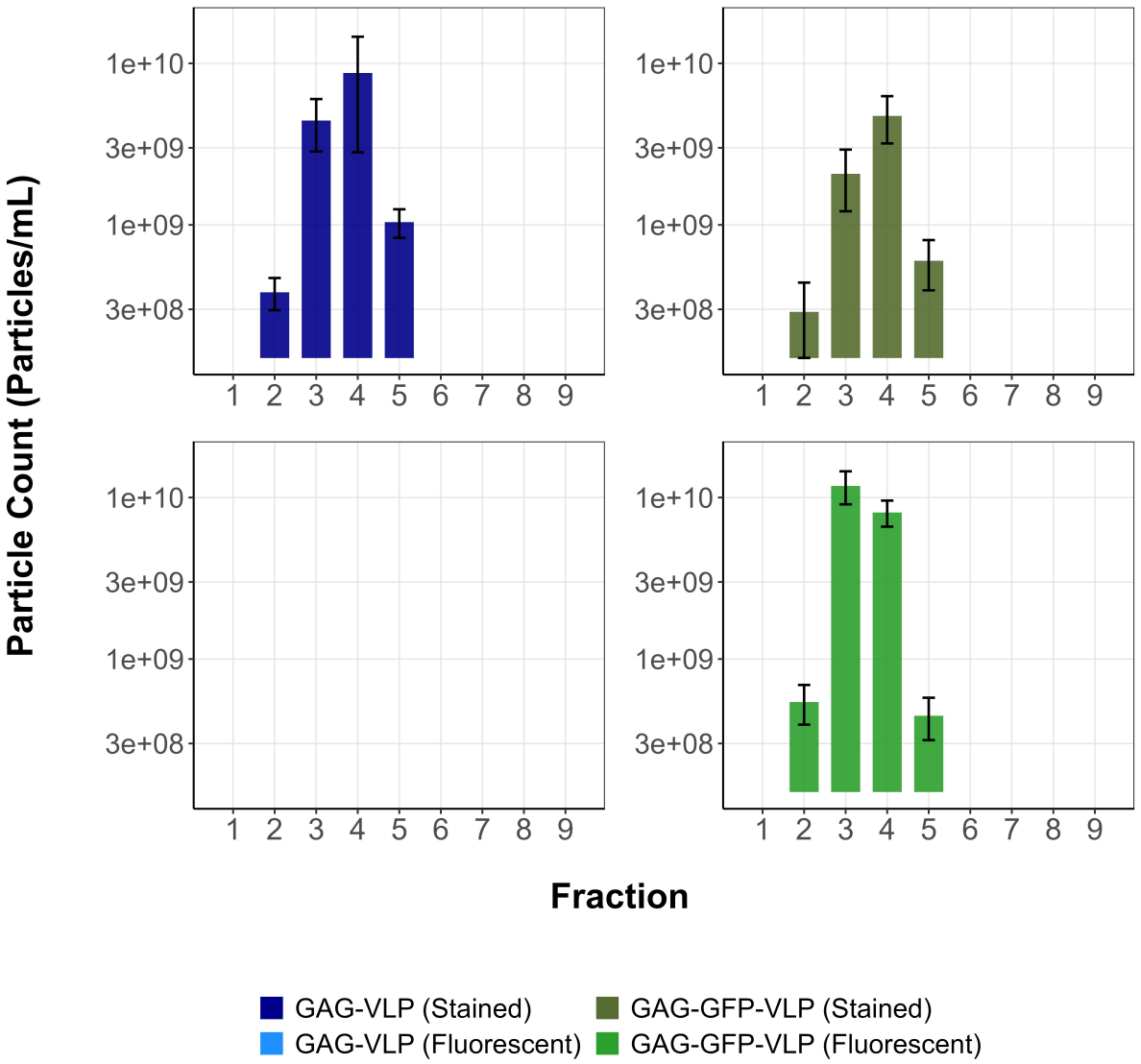

Figure 4.7: Flow virometry-derived particle concentration in semi-purified sample. dsDNA-containing particles in GAG-VLP (dark blue), GAG-GFP-VLP (dark green). Fluorescent particles in GAG-VLP (light blue), GAG-GFP-VLP (light green). Fluorescent flow virometry of GAG-VLP samples yielded data close to the instrument LOD ($1.5*10^8$ Particles/mL) consistent with non-fluorescent signal shifting, data not shown. Error bars represent biological replicates.

4.2.4 Immunoblotting

To assess protein composition characteristics of particles in semi-purified fractions of interest (1 - 6), immunoblotting was performed using antibodies specific to structural proteins. GP64 (64 kDa), P24 (24 kDa alone, 55 kDa in complete GAG), and Spike (monomeric 180 kDa, trimeric 540 kDa) are the major structural proteins of baculovirus, HIV, and SARS-CoV, and will be present on their respective viral particles or VLPs [64, 62].

Baculovirus Major Structural Protein - GP64

An equivolumetric sample of infected cell culture supernatant from rBEV-GAG-VLP, rBEV-GAG-GFP-VLP, and rBEV-SARS-VLP was run with each Western blot and used as a normalized reference point for comparison.

All rBEVs showed similar trends in intensity of blotting over fractions 1 – 6, with fractions 1 and 6 showing little to no GP64, fractions 2 and 5 showing a fraction of intensity of the infected cell culture supernatant, and fractions 3 and 4 presenting the highest intensities, approximately 25 – 125 % and 250% higher than the reference respectively (Figures 4.8, 4.9). This suggests that the majority of baculovirus virions, or particles presenting GP64, are present in decreasing abundance in fractions 4, 3, 5, and 2.

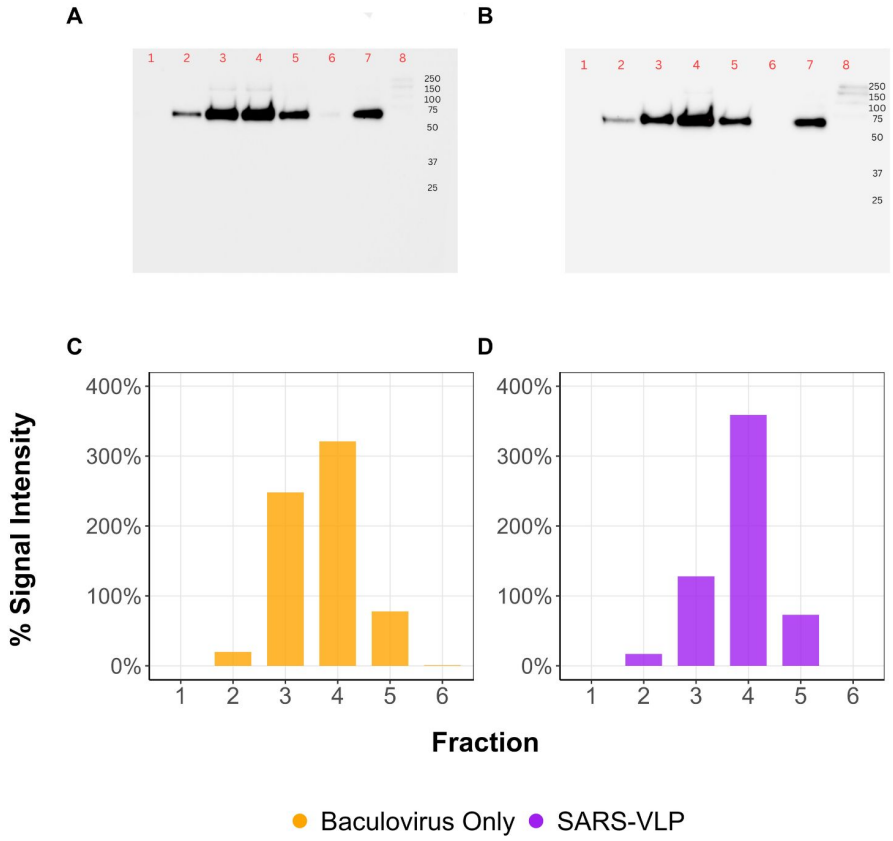

Figure 4.8: Anti-GP64 Western blots and band intensity of semi-purified samples. Lanes 1 - 6: Fractions 1 - 6. Lane 7: Equivolumetric supernatant mixture (GAG-VLP:GAG-GFP-VLP:SARS-VLP) included for signal normalization. Lane 8: Unstained Precision Plus Protein™molecular weight ladder (Bio-Rad). A, C: Baculovirus Only / rBEV-mKOκ (orange). B, D: SARS-VLP (purple).

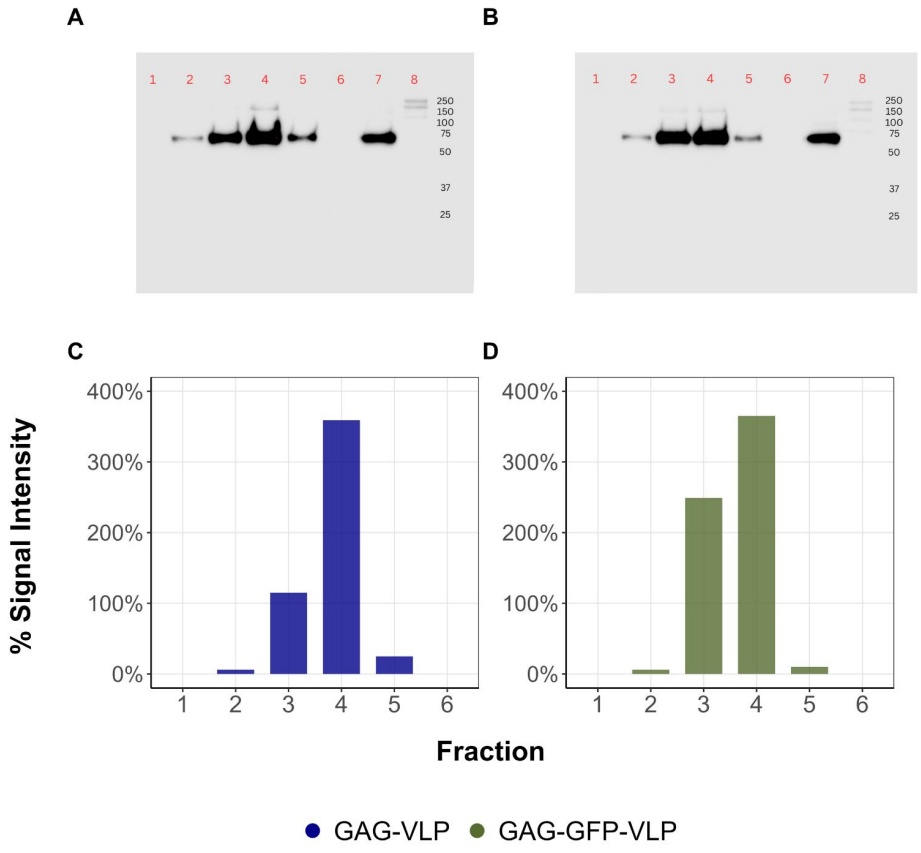

Figure 4.9: Anti-GP64 Western blots and band intensity of semi-purified samples. Lanes 1 - 6: Fractions 1 - 6. Lane 7: Equivolumetric supernatant mixture (GAG-VLP:GAG-GFP-VLP:SARS-VLP) included for signal normalization. Lane 8: Unstained Precision Plus Protein™molecular weight ladder (Bio-Rad). A, C: GAG-VLP (blue). B, D: GAG-GFP-VLP (green).

HIV Major Structural Protein - P24

After acid-washing Western blots containing GAG-VLP and GAG-GFP-VLP samples, blots were re-probed using polyclonal anti-P24 antibodies. As a sub-component of GAG polyproteins, P24 was expected to be detected at approximately 55 kDa.

GAG-VLP showed far lower intensity of P24 signal when compared to the same fractions of GAG-GFP-VLP (Figure 4.10). GAG-VLP also showed a similar distribution trend of P24 signal intensity as GP64, with P24-containing particles showing decreasing abundance from fractions 4, 3, and 5. GAG-GFP-VLP by contrast, showed a distribution trend of P24 signal intensity unlike GP64, with P24-containing particles showing decreasing abundance from fractions 3, 4, 2, and 5. This suggests that the distribution trends of P24-containing particles are not identical between GAG-VLP and GAG-GFP-VLP samples, contrary to expectations. These results imply that based on the difference in distribution trends of GP64 and P24 in GAG-GFP-VLP, the majority of GP64 and P24 are present on particles of different densities. The multiple bands observed in the GAG-GFP-VLP sample are expected to correspond to various sizes of GAG-GFP polyprotein resulting from differential cleavage through some native cellular mechanism.

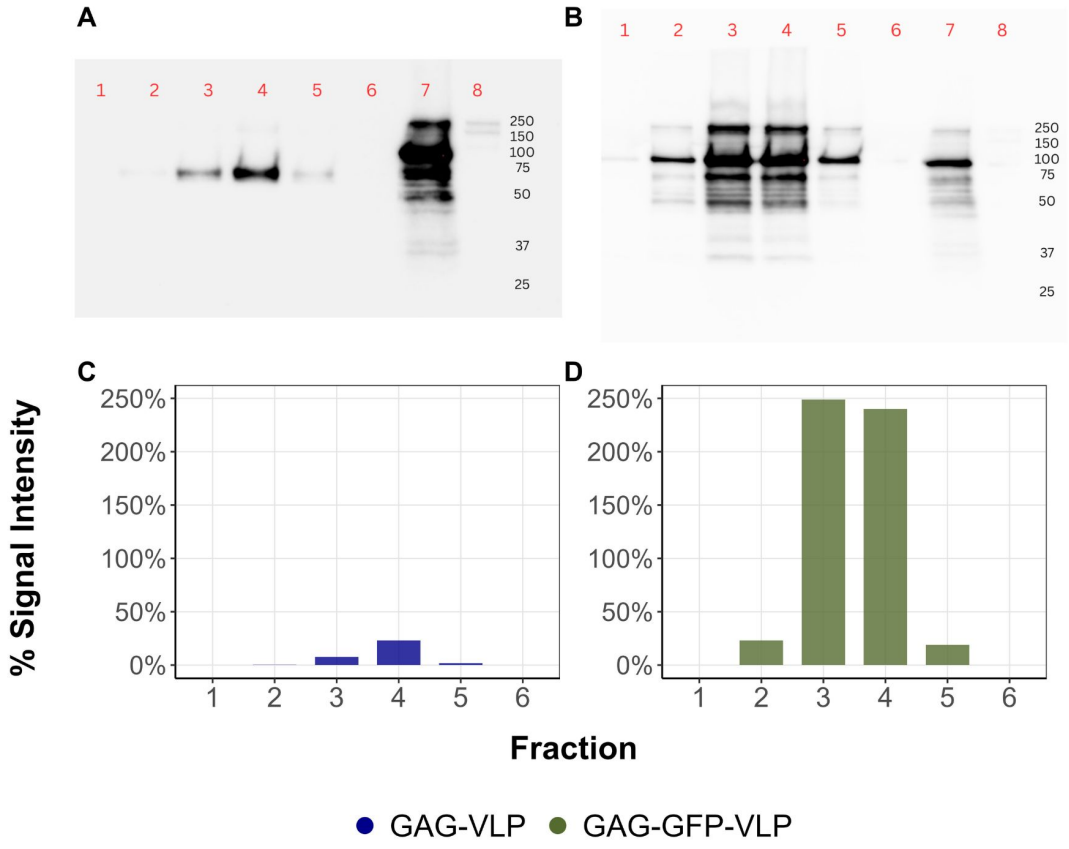

Figure 4.10: Anti-P24 Western blots and band intensity of semi-purified samples. Approximately 55 kDa band used for signal intensity comparison. Lanes 1 - 6: Fractions 1 - 6. Lane 7: Equivolumetric supernatant mixture (GAG-VLP:GAG-GFP-VLP:SARS-VLP) included for signal normalization. Lane 8: Unstained Precision Plus Protein™molecular weight ladder (Bio-Rad). A, C: GAG-VLP (blue). B, D: GAG-GFP-VLP (green).

SARS Major Structural Protein - Spike

Dot blots were performed separately on semi-purified SARS-VLP fractions of interest, using monoclonal anti-Spike antibodies to detect Spike protein. Infected cell culture supernatant from SARS-VLP was used as an intensity normalization reference in addition to fractions 1 – 6 for each biological replicate of SARS-VLP.

SARS-VLP biological replicates demonstrated consistent Spike protein distribution, with decreasing abundance of Spike protein in fractions 4, 3, 5, and 2 (Figure 4.11). This suggests that the majority of SARS-VLPs or particles presenting Spike protein are present between fractions 2 - 5. Furthermore since distribution trends are similar between Spike proteins and GP64, it can be inferred that particles harboring these membrane-bound proteins have a similar distribution when subject to semi-purification.

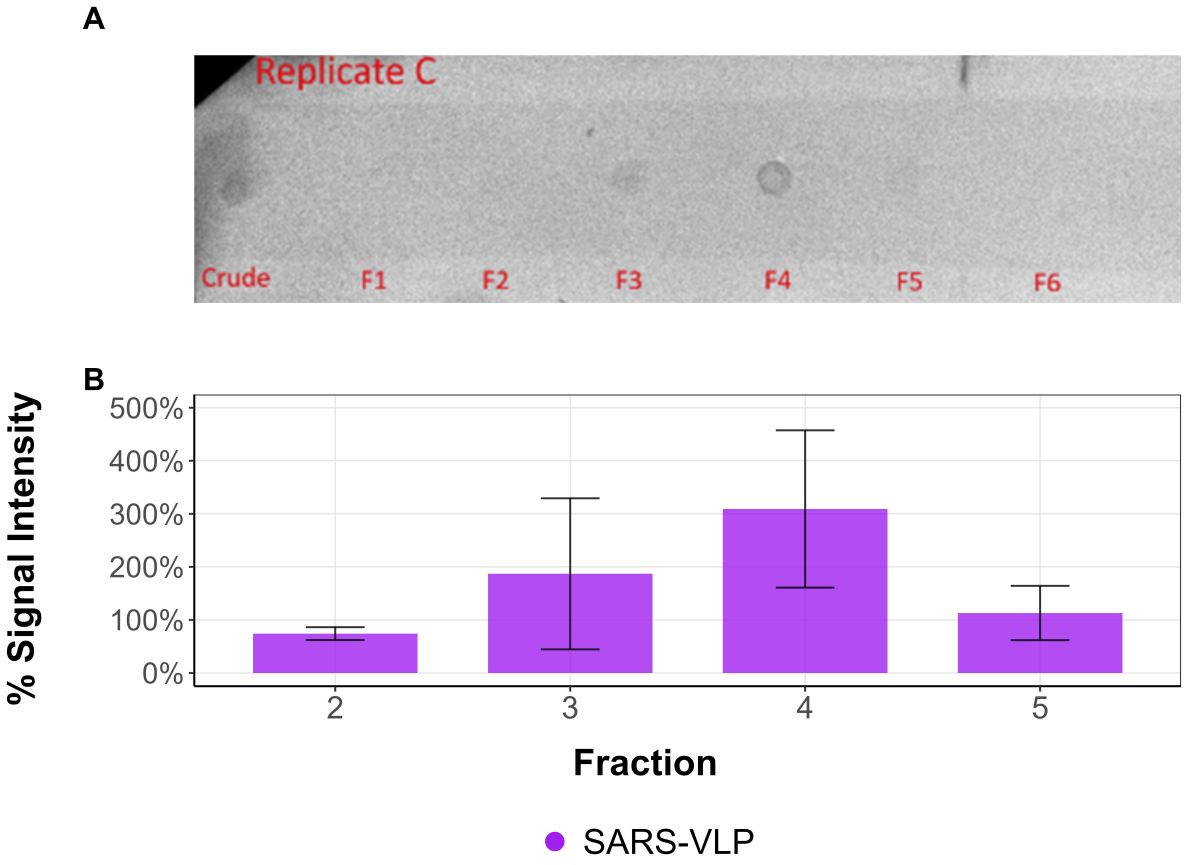

Figure 4.11: Anti-Spike dot blots and dot intensity in semi-purified samples. A: Dot blot of semi-purified SARS-VLP fractions, replicate C shown as method representative. "Crude" and "F1 - F6" correspond to infected cell culture supernatant and semi-purified fractions 1 - 6 respectively. B: Intensity of fraction signal normalized to infected cell culture supernatant signal. Error bars represent biological triplicates.

4.2.5 Multi-Angle Dynamic Light Scattering

MADLS was used to look at particle size and concentration. The results suggested two clusters of particle sizes resulting from the samples independent of the "solvent peak" introduced by preparation in iodixanol. Particles were treated as two distinct classes based on diameter X, where (X > 250 nm) or (50 nm < X < 250 nm).

A requirement for accurate MADLS measurements is knowledge of sample-specific optical/physical properties, including refractive index, absorbance, and viscosity. These properties become parameters for the mathematical interpretation of light intensity fluctuations and their translation into particle sizes and concentrations. Viscosity is required in the Stokes-Einstein-Sutherland equation, and an underestimation of viscosity can cause particles to appear larger than they truly are due to the slow rate of diffusion they experience in increasingly viscous media [65]. Refractive index of the particle is required when applying the Rayleigh Scattering Intensity Law, which will affect particle concentration results [66]. Refractive indices of the medium and particle are both required for the Rayleigh-Gans-Debye Approximation, which is a derivative of the Rayleigh Scattering Intensity Law [67]. This equation relates the intensity of the scattered light to the differential of the refractive index of the medium, through which the incident and scattered light must both transit through, and that of the particle with which the incident light must interact in order to scatter [67]. Theoretically if the refractive indices of both the medium and the particle

were identical, the light would appear to pass through the particle uninterrupted, which can cause significant underestimation in particle concentration when left unaccounted. Absorbance of the particle is essential in understanding the degree to which the incident light fails to be scattered and is instead absorbed and dissipated in another energetic form. If unaccounted for it may appear that particle concentration is far lower than in reality, the Beer-Lambert Law is particularly relevant for the fundamentals of the MADLS technique though it is often taken for granted since most materials have widely published absorbance values [68].

Semi-purified fractions of infected samples present with two main particle classes of interest, those where diameter X is (50 nm $<$ X $<$ 250 nm) and (X $>$ 250 nm). VLPs are likely to be detected within the particle class where (50 nm $<$ X $<$ 250 nm), whereas baculovirus virions are likely to be detected within the class where (X $>$ 250 nm).

Distribution of (50 nm $<$ X $<$ 250 nm) particles appears to be consistent between samples, with the majority of reliable concentrations presenting in fractions 2 - 4 of infected and 1 - 3 of uninfected samples. Infected sample fractions 1, 5, and 6 in addition to uninfected sample fractions 4 - 5 consistently present with (50 nm $<$ X $<$ 250 nm) particles with unreliable concentration measurements, therefore they have been marked with an asterisk in visualization (see C.3.3 for further details on measurement reliability criteria and C.20, C.21 for visualization of fractions 1 - 6). It is of note that all infected samples

present decreasing abundance of (50 nm $<$ X $<$ 250 nm) particles in fractions 4, 3, and 2, with the exception of GAG-GFP-VLP in which abundance decreases from fraction 3, 4, and 2 (Figure 4.12). Uninfected samples do not reliably follow this trend, and fractions 1 - 3 present concentrations approximately one order of magnitude lower than infected samples. This suggests that (50 nm $<$ X $<$ 250 nm) particles are separated similarly across infected samples, but that GAG-GFP-VLP samples contain additional (50 nm $<$ X $<$ 250 nm) particles which are less dense than other samples. This is supported by the slight concentration increase in fraction 3 for GAG-GFP-VLP samples compared to other infected samples. These particles may be slightly larger compared to other (50 nm $<$ X $<$ 250 nm) particles of the same class in other samples, as evidenced by the average size of (50 nm $<$ X $<$ 250 nm) particles in GAG-GFP-VLP appearing larger compared to fraction 3 of other samples (Figure 4.13). Also of note is that uninfected particle size ranges of this class possess greater variability than infected samples, suggesting a non-homogeneous origin for these particles in uninfected samples. The identity of these particles may be apoptotic bodies, as unpassaged cell cultures are known to accumulate growth factors which are potent inducers of apoptosis, which could explain their highly variable sizes.

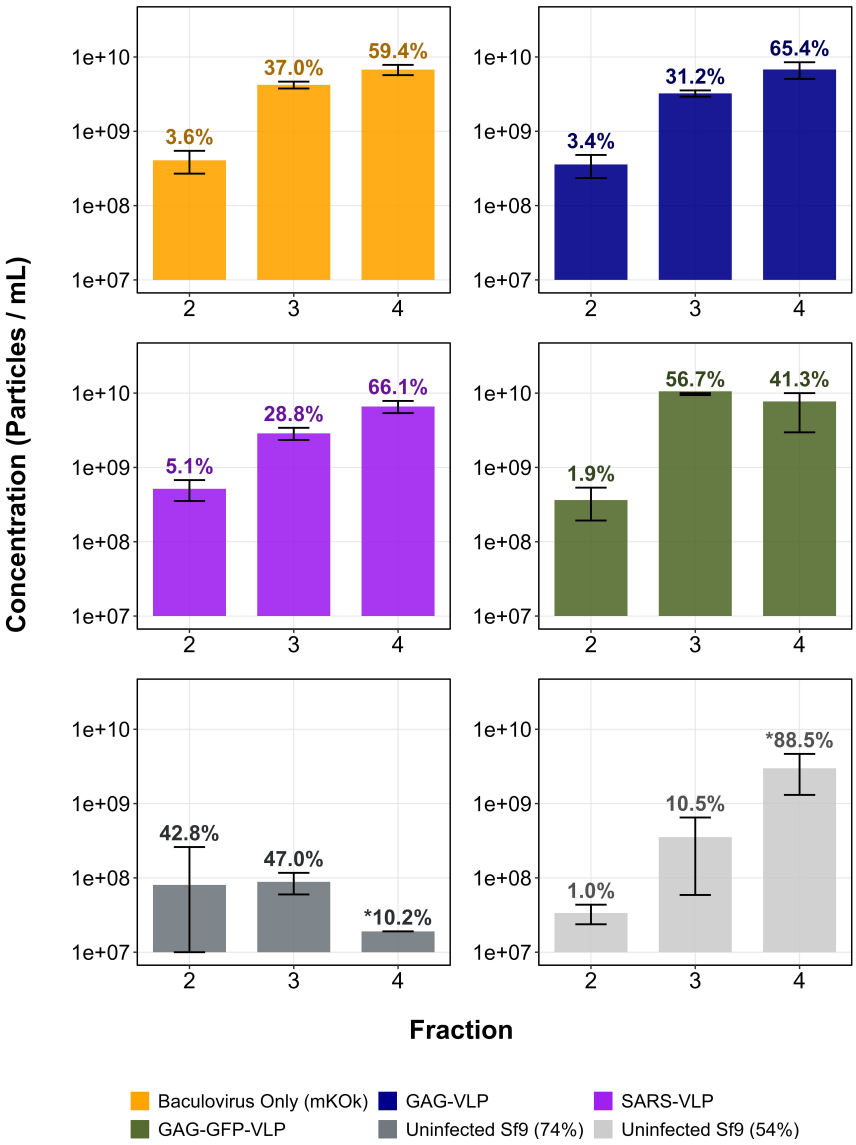

Figure 4.12: MADLS-derived particle concentration in semi-purified samples for particles of 50 nm < diameter < 250 nm. Baculovirus Only / rBEV-mKOκ (orange), GAG-VLP (blue), GAG-GFP-VLP (green), SARS-VLP (purple), Uninfected Sf9 supernatant at 54% viability (light grey), 74% viability (dark grey). Percentage of total particles indicated above measurement. Although measurements were taken for fractions 1 - 9, confident measurements were only obtained for fractions 2 - 4 for infected and 1 - 3 for uninfected samples. Samples with a hit rate less than 50% of total scans or unacceptably high standard error are denoted by an asterisk (See C.10, C.11 for further details). Error bars represent decuplicate scans of biological triplicates for infected and decuplicate scans for uninfected samples.

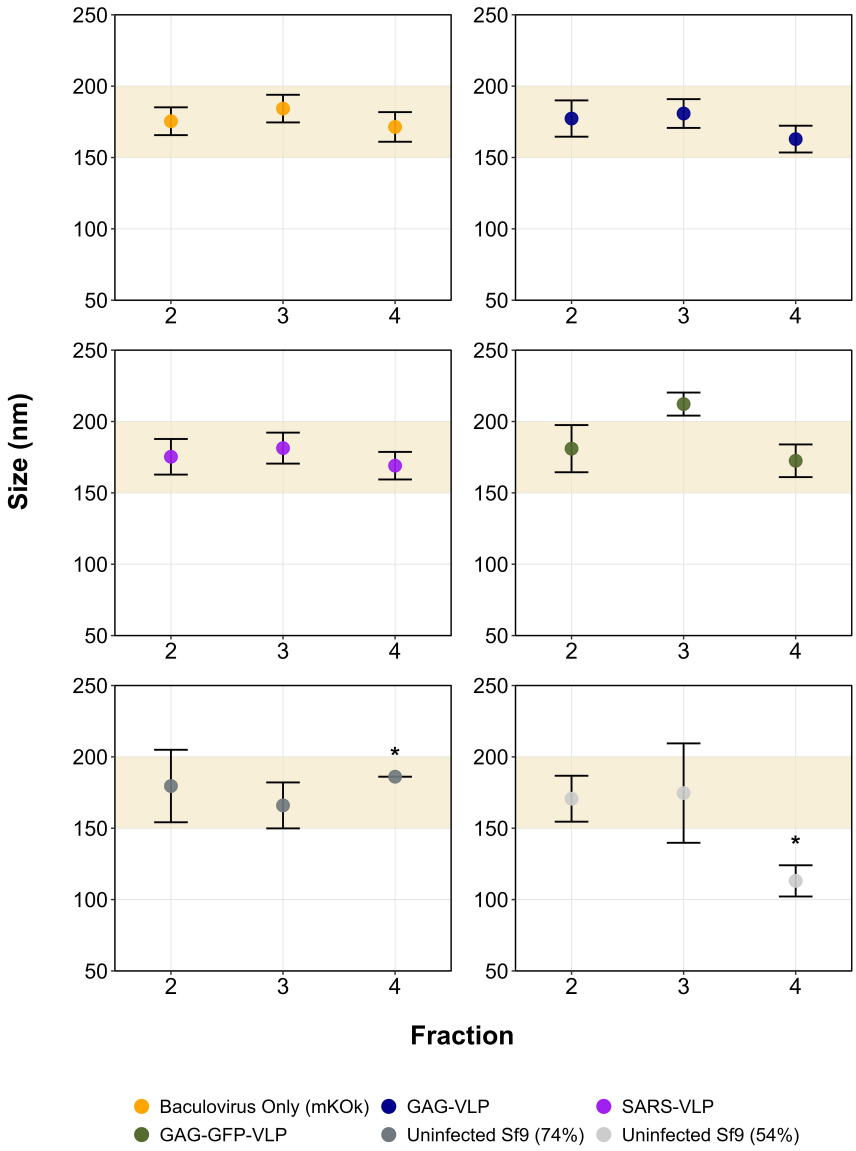

Figure 4.13: MADLS-derived particle size in semi-purified samples, for particles of 50 nm < diameter < 250 nm. Baculovirus Only / rBEV-mKOκ (orange), GAG-VLP (blue), GAG-GFP-VLP (green), SARS-VLP (purple), Uninfected Sf9 supernatant at 54% viability (light grey), 74% viability (dark grey). Although measurements were taken for fractions 1 - 9, confident measurements were only obtained for fractions 2 - 4 for infected and 1 - 3 for uninfected samples. Samples with a hit rate less than 50% of total scans or unacceptably high standard error are denoted by an asterisk (See C.10, C.11 for further details). Error bars represent decuplicate scans of biological triplicates for infected and decuplicate scans for uninfected samples. Light beige graph area visually highlights particles between 150 - 200 nm in diameter.

Distribution of (X > 250 nm) particles appears to be consistent between samples, with the majority of reliable concentrations presenting in infected samples in fractions 2 - 5 and uninfected samples across fractions 1 - 6. Fraction 6 of infected samples consistently presents with (X > 250 nm) particles at unreliable concentration measurements in infected samples, therefore they have been marked with an asterisk in visualization (see C.3.3 for further details on measurement reliability criteria and C.22, C.23 for visualization of fractions 1 - 6). It is of note that all infected samples present decreasing abundance of (X > 250 nm) particles in fractions 4, 3, 5, and 2, though this difference is not as pronounced between fraction 3 and 5 for uninfected samples (Figure 4.14). This suggests that (X > 250 nm) particles are separated similarly across infected samples. These particles appear to have consistent size distribution within their class, aside from slightly increased variability in fraction 5 for SARS-VLP and GAG-GFP-VLP samples (Figure 4.15).

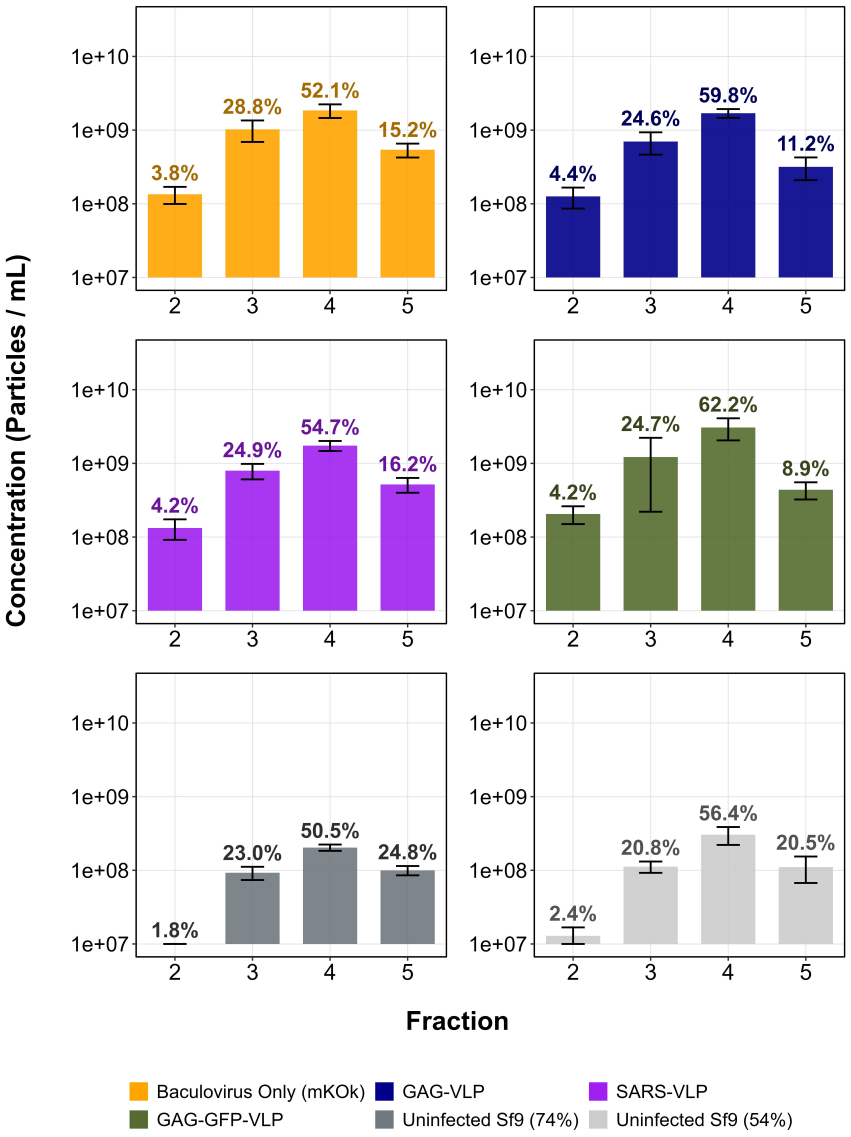

Figure 4.14: MADLS-derived particle concentration in semi-purified samples for particles of diameter > 250 nm. Baculovirus Only / rBEV-mKOκ (orange), GAG-VLP (blue), GAG-GFP-VLP (green), SARS-VLP (purple), Uninfected Sf9 supernatant at 54% viability (light grey), 74% viability (dark grey). Percentage of total particles indicated above measurement. Although measurements were taken for fractions 1 - 9, confident measurements were only obtained for fractions 2 - 5 for infected and 1 - 6 for uninfected samples. Samples with a hit rate less than 50% of total scans are denoted by an asterisk (See C.12, C.13 for further details). Error bars represent decuplicate (10x) scans of biological triplicates for infected and decuplicate scans for uninfected samples.

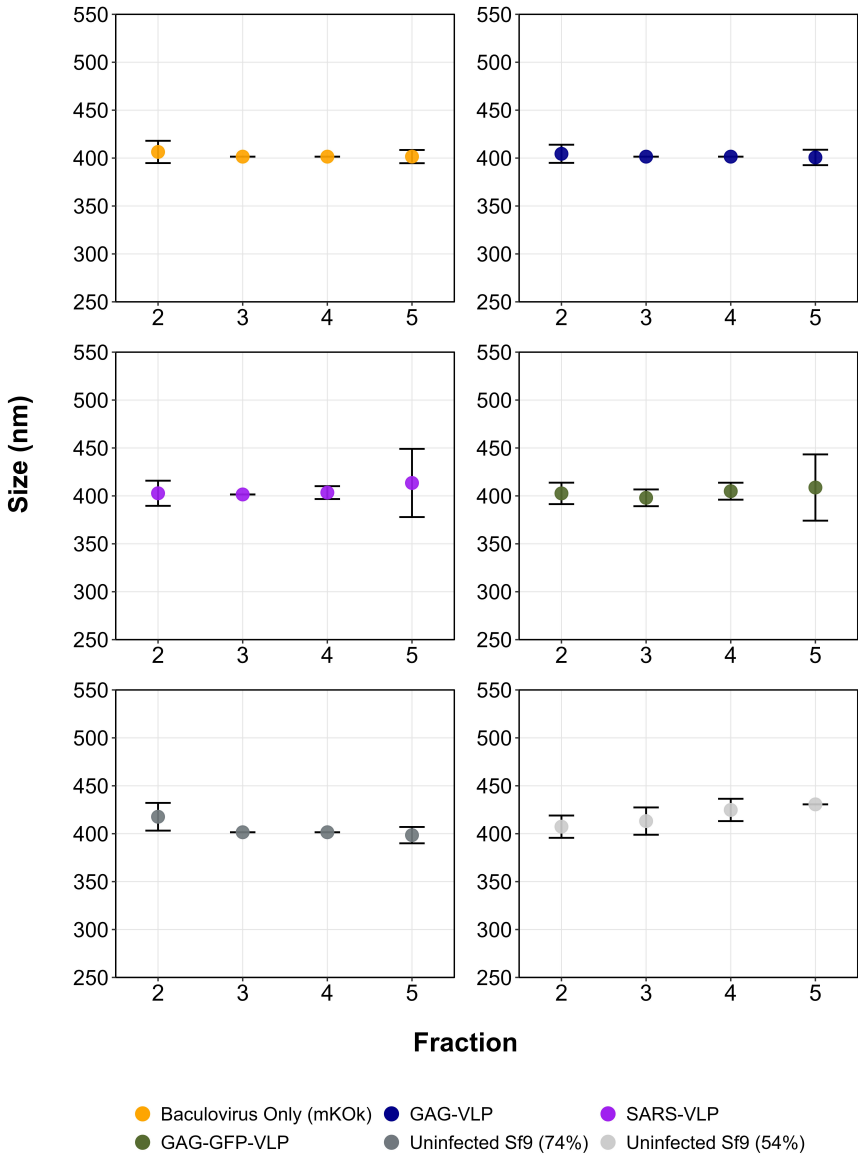

Figure 4.15: MADLS-derived particle size in semi-purified samples for particles of diameter $>$ 250 nm. Baculovirus Only / rBEV-mKOκ (orange), GAG-VLP (blue), GAG-GFP-VLP (green), SARS-VLP (purple), Uninfected Sf9 supernatant at 54% viability (light grey), 74% viability (dark grey). Although measurements were taken for fractions 1 - 9, confident measurements were only obtained for fractions 2 - 5 for infected and 1 - 6 for uninfected samples. Samples with a hit rate less than 50% of total scans are denoted by an asterisk (See C.12, C.13 for further details). Error bars represent decuplicate scans of biological triplicates for infected and decuplicate scans for uninfected samples.

To best examine the contrast between infected and uninfected samples, raw MADLS particle concentration results were transformed into two types of resultant figures: 1) Where an uninfected sample was subtracted from an infected sample (Figures 4.16, 4.17). Two styles of fraction matching were by fraction number (F2F) or by similarity of density (D2D). 2) Where infected samples were divided by the average value of uninfected samples (Figures 4.18, 4.19). For both figure types, only fractions of interest for each particle class were examined.

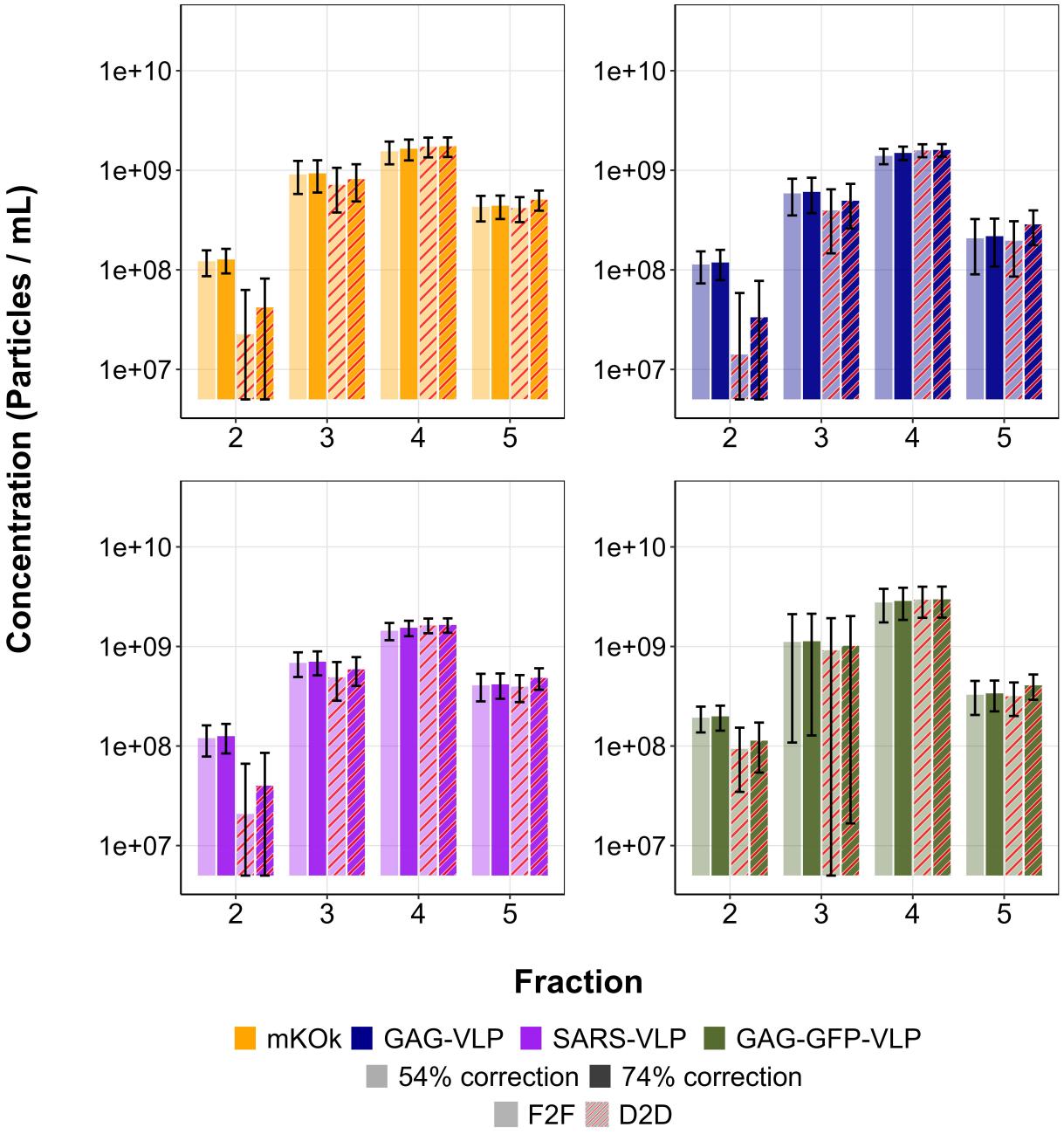

Figure 4.16: MADLS-derived particle concentration in semi-purified samples for particles of diameter > 250 nm after subtraction by a given uninfected Sf9 supernatant sample at 54% viability (light grey) or 74% viability (dark grey) by fraction (F2F) (no stripes) or density (D2D) (red stripes) matching. Baculovirus Only / rBEV-mKOκ (orange), GAG-VLP (blue), GAG-GFP-VLP (green), SARS-VLP (purple). Error bars represent decuplicate scans of biological triplicates.

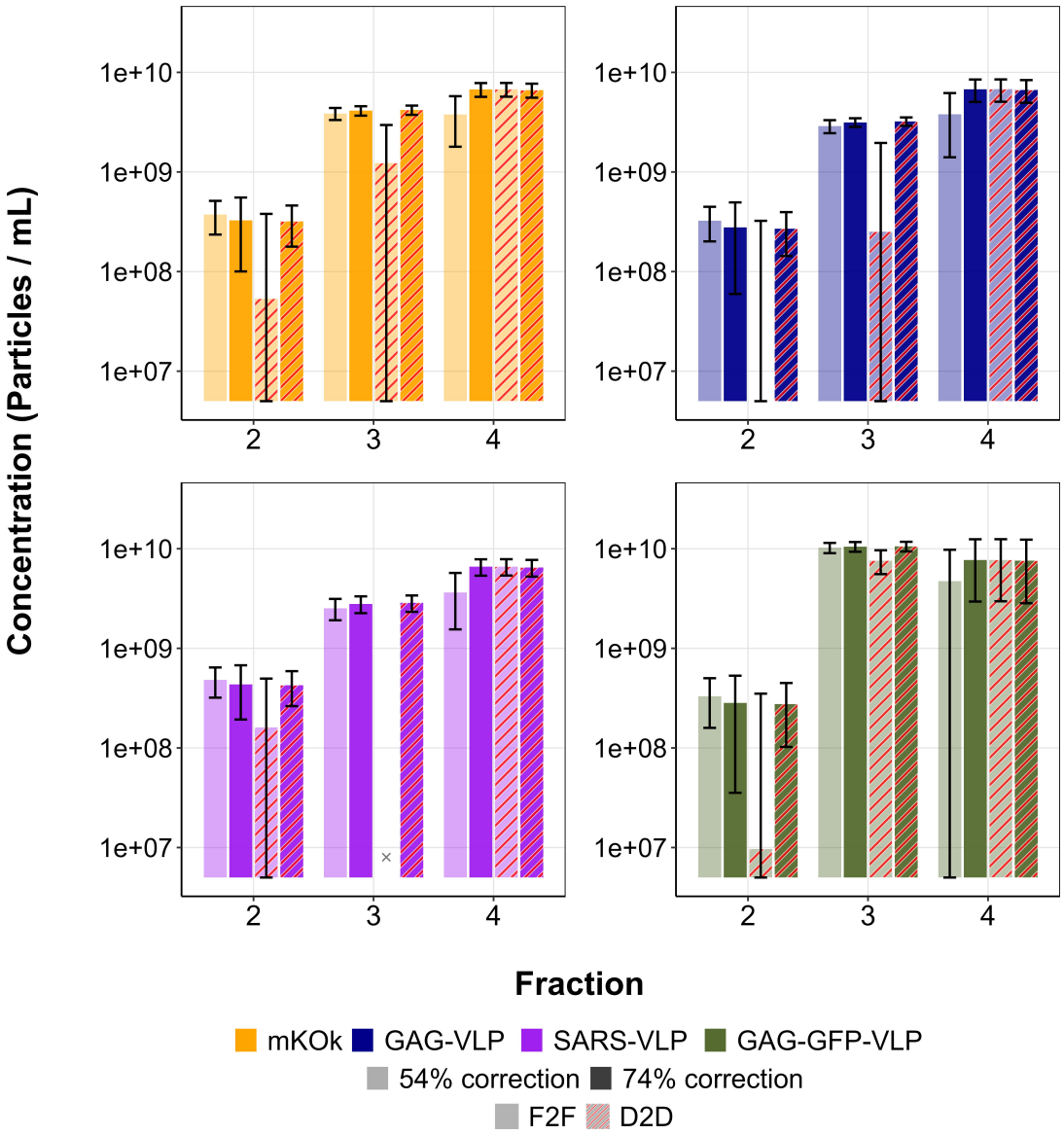

Figure 4.17: MADLS-derived particle concentration in semi-purified samples for particles of 50 nm $<$ diameter $<$ 250 nm after subtraction by a given uninfected Sf9 supernatant sample at 54% viability (light grey) or 74% viability (dark grey) by fraction (F2F) (no stripes) or density (D2D) (red stripes) matching. Baculovirus Only / rBEV-mKOκ (orange), GAG-VLP (blue), GAG-GFP-VLP (green), SARS-VLP (purple). Error bars represent decuplicate scans of biological triplicates. Samples where a zero value was obtained after subtraction are denoted by the symbol "x".

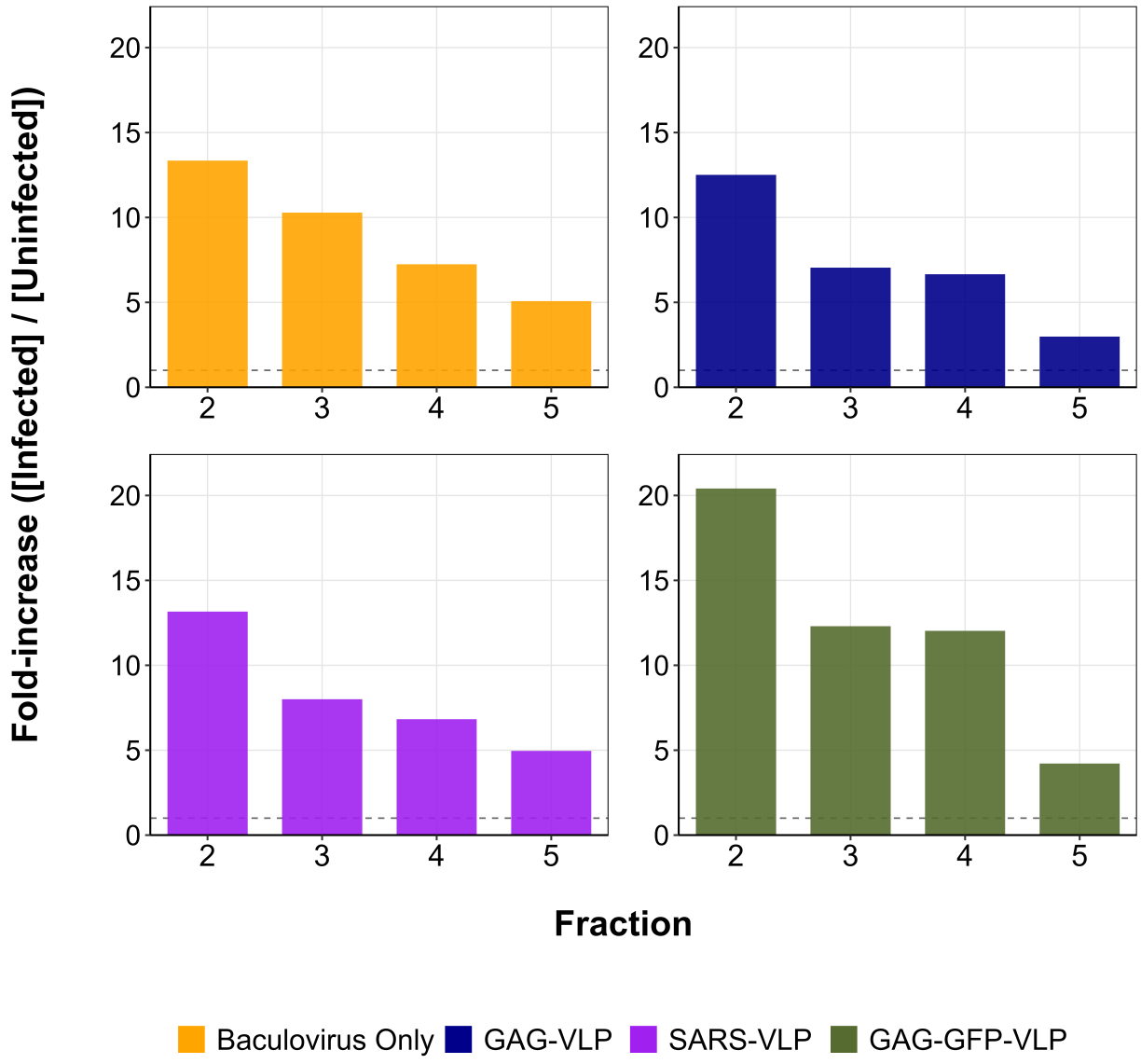

Figure 4.18: Fold-increase of average particle concentration in semi-purified samples for particles of diameter > 250 nm when compared to average particle concentration of uninfected samples. Baculovirus Only / rBEV-mKOκ (orange), GAG-VLP (blue), GAG-GFP-VLP (green), SARS-VLP (purple). Dashed line through y = 1 visually highlights the baseline of average uninfected samples.

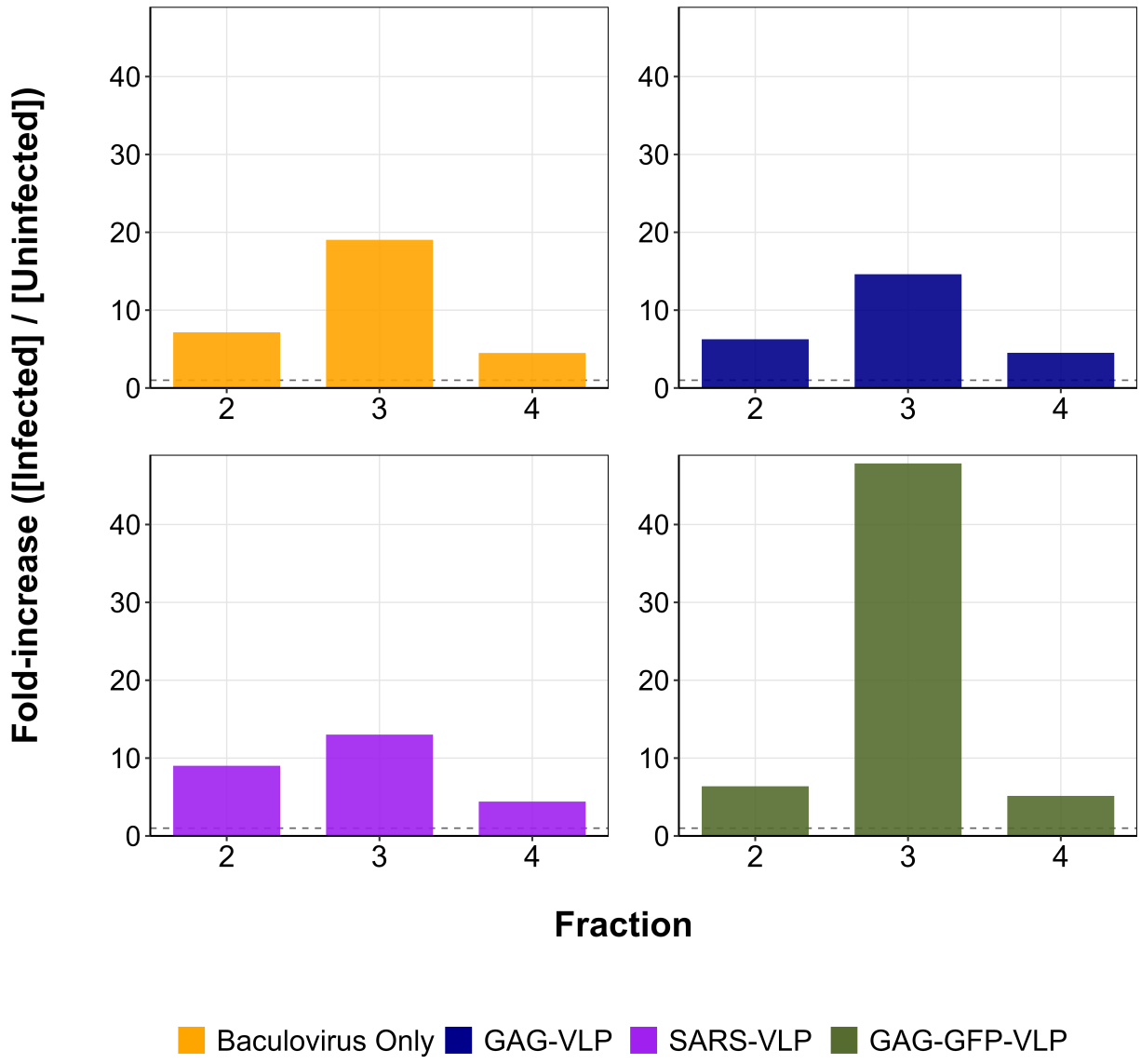

Figure 4.19: Fold-increase of average particle concentration in semi-purified samples for particles of diameter 50 nm $<$ diameter $<$ 250 nm when compared to average particle concentration of uninfected samples. Baculovirus Only / rBEV-mKOκ (orange), GAG-VLP (blue), GAG-GFP-VLP (green), SARS-VLP (purple). Dashed line through y = 1 visually highlights the baseline of average uninfected samples.

Type 1 figures show more noticeable differences between F2F and D2D fraction matching styles in fractions 2 and 3 across all samples and both particle classes. For (X > 250 nm) particles D2D matching shows more drastic decrease in particle concentration in fraction 2 by approximately 1 order of magnitude, and by a smaller margin in fraction 3 when compared to the F2F matching style (Figure 4.16). There appears to be no discernible difference in fractions 4 and 5 between fraction matching styles. This exacerbation of particle concentration differences between fractions 2 and 3 is contrasted by relative stability in 4 and 5 across samples by both D2D and F2F fraction matching styles. For (50 nm < X < 250 nm) particles this effect is repeated in fractions 2 and 3, with a magnified decrease in concentration for the D2D fraction matching style in fraction 3 across samples when subtracting uninfected Sf9 samples at 54% viability, but unexpectedly no major difference when the subtraction is repeated with uninfected samples at 74% viability. This effect appears to be confined to fractions 2 and 3 for all samples, with the exception of GAG-GFP fraction 3 (Figure 4.17). Distribution trends for both particle classes are similar in both sample types (Figures C.22, C.20) and there is more variability between viability of sample subtracted than the style of fraction matching itself. Taken together these observations suggest an F2F fraction matching style may produce a more consistent baseline for comparison of infected and uninfected samples.

Type 2 figures present a more visually apparent comparison between infected samples

when compared to a baseline produced from the average particle concentration of both uninfected samples. For (X > 250 nm) particles in key fractions it becomes clear that the proportion of particles generated as a consequence of infection reaches a peak in fraction 2 followed by a decreasing order of fractions 3, 4, and 5 across all infected samples (Figure 4.18). This is in contrast to expectations set by established and orthogonal methods, in which particles of this class are shown be found at highest concentrations in fraction 4 followed by 3, 5, and 2 (Figure C.22). This suggests that particles of this class do not exclusively correspond to baculovirus and are indeed present at noteworthy concentrations in fractions 3 - 5 more so than fraction 2 in uninfected samples, although there is a clear fold-increase in all key fractions. For (50 nm < X < 250 nm) particles it is observed that the highest fold-increase in particle concentration is observed in fraction 3 followed by 2 and 4 from infected compared to uninfected samples (Figure 4.19). This is somewhat in-line with expectations, where fraction 3 has been demonstrably enriched in particles of this class in contrast to fraction 2, however it is interesting that fraction 4 does not possess a similar degree of proportional increase in particle concentration. This suggests that there may be more particles produced as a result of infection dynamics of a density captured by fraction 3 than by either fractions 2 or 4, irrespective of sample. Both particle classes share the feature of GAG-GFP-VLP samples possessing higher fold-increase when compared to other infected samples Figures 4.18, 4.19). This is true for (X > 250 nm)

particles in fractions 2 - 4 and in (50 nm $<$ X $<$ 250 nm) particles in fraction 3, however all other fractions possess similarities to other infected samples.

4.2.6 Correlation of Orthogonal Methods

A key component of this project is to determine if an unestablished method can prove reliability and support established methods in sample analysis. MADLS and flow virometry results were compared to assess their correlation. Baculovirus virions are expected to have dsDNA and be larger than 250 nm in diameter, hence results of SYBR Green I stained flow virometry and MADLS concentration for particles with diameter greater than 250 nm were plotted (Figure 4.20). GAG-GFP-VLPs are expected to fluoresce and be between 50 nm and 250 nm in diameter, hence results of fluorescence flow virometry and MADLS concentration for particles with diameter between 50 nm and 250 nm were plotted (Figure 4.21). To determine the most well-correlated aspect of MADLS, flow virometry-derived particle concentrations were plotted against varying MADLS conditions. Where MADLS particle concentration is represented by (50 nm $<$ X $<$ 250 nm) particles (left panel), (X $>$ 250 nm) particles (center panel), and the sum of both aforementioned particle classes (right panel).

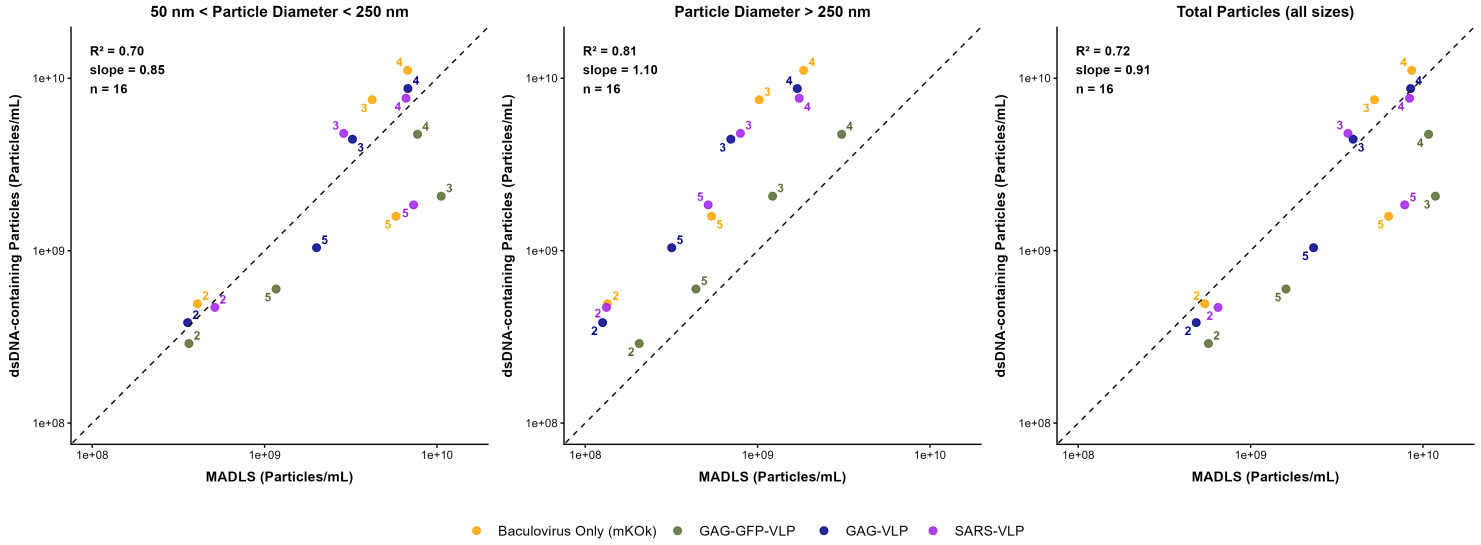

Figure 4.20: Correlation between MADLS-derived particle concentration (x) and dsDNA-containing particles detected via SYBR Green I flow virometry (y) in semi-purified samples. MADLS-derived particle concentrations of particles 50 nm $<$ diameter $<$ 250 nm (left panel), diameter $>$ 250 nm (center panel), and the sum of both particle classes (right panel) are compared. Baculovirus Only / rBEV-mKOκ (orange), GAG-VLP (blue), GAG-GFP-VLP (green), SARS-VLP (purple). Numerical label indicates fraction number. Dashed line indicates equivalency between measurements of both methods.

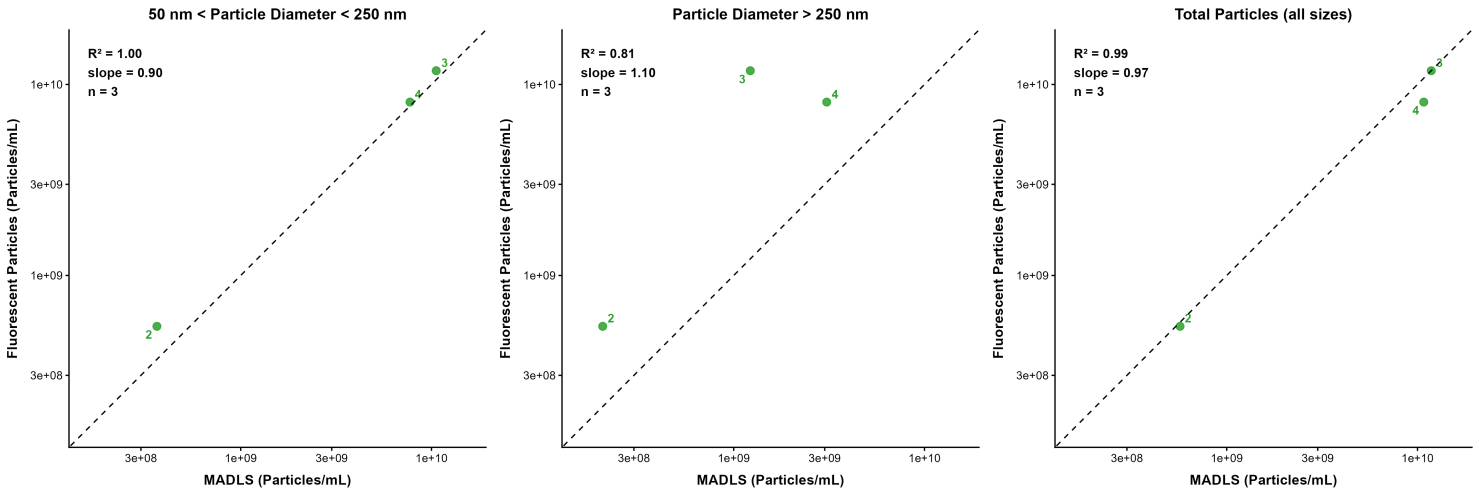

Figure 4.21: Correlation between MADLS-derived particle concentration (x) and fluorescent particles detected via flow virometry (y) in semi-purified samples. MADLS-derived particle concentrations of particles 50 nm $<$ diameter $<$ 250 nm (left panel), diameter $>$ 250 nm (center panel), and the sum of both particle classes (right panel) are compared. GAG-GFP-VLP (green). Numerical label indicates fraction number. Dashed line indicates equivalency between measurements of both methods.

For the correlation between dsDNA-containing particles detected by flow virometry and MADLS, the R^2 values for (50 nm $<$ X $<$ 250 nm) particles, (X $>$ 250 nm) particles, and the sum of both aforementioned particle classes were 0.70, 0.81, and 0.72 respectively (Figure 4.20). Therefore the strongest correlation between MADLS and dsDNA-containing particle concentration analyzed by flow virometry appears when MADLS is represented by the concentration of (X $>$ 250 nm) particles. This suggests that baculovirus particles are more likely to be particles of diameter (X $>$ 250 nm). When this particle class was examined after MADLS values were subtracted by various uninfected conditions as they were in type 1 graphs (Figure 4.16), the F2F fraction matching style more closely resembled the one examined here (Figure C.16). Using this particle class once more, this time separated by biological replicate, it is clear that the majority of GAG-GFP-VLP samples align closer to the 1:1 equivalency line between the two methods, and indeed most samples are in line with their own replicates to some extent (Figure C.19). Fractions 2 - 5 of baculovirus only, GAG-VLP, and SARS-VLP, results show a tight grouping, indicating that these three samples are more similar to one another than GAG-GFP-VLP samples (Figure 4.20). However this grouping's positioning suggests that MADLS typically underestimates concentration of particles where diameter is greater than 250 nm, when compared to SYBR Green I flow virometry. For GAG-GFP-VLP semi-purified samples, these methods appear to be more strongly correlated as indicated by its positioning. The expectation that baculovirus

virions can be detected by SYBR Green I flow virometry and MADLS can be used to confirm this appears to be founded. Underestimation of particle concentration by MADLS must be considered when applying this method to baculovirus detection.

For the correlation between fluorescent particles detected by flow virometry and MADLS, the R^2 values for (50 nm $<$ X $<$ 250 nm) particles, (X $>$ 250 nm) particles, and the sum of both aforementioned particle classes were 1.00, 0.81, and 0.99 respectively (Figure 4.21). Therefore the strongest correlation between MADLS and fluorescent particle concentration analyzed by flow virometry appears when MADLS is represented by the concentration of (50 nm $<$ X $<$ 250 nm) particles. This suggests that GAG-GFP-VLPs are more likely to be particles of diameter (50 nm $<$ X $<$ 250 nm). When this particle class was examined after MADLS values were subtracted by various uninfected conditions as they were in type 1 graphs (Figure 4.17), the F2F fraction matching style more closely resembled the one examined here (Figure C.17). Using this particle class separated by biological replicate, it is clear that the majority of GAG-GFP-VLP samples are in fairly tight groups around the 1:1 equivalency line Figure C.18). Fractions 2 - 4 of GAG-GFP-VLP, the correlation appears very strong between fluorescence flow virometry and MADLS-derived concentration for particles between 50 nm and 250 nm in diameter (Figure 4.21). It is worth noting that the correlation is strongest in fractions 3 and 4, where GAG-GFP-VLP appears to have the highest concentrations, when compared to nearly 1.5-fold less in fraction 2. This

could indicate that MADLS measurements are most accurate when particle concentration is higher, particularly relevant in biological production systems. Despite this minor deviation, correlation between fluorescence flow virometry and MADLS-derived concentration for particles between 50 nm and 250 nm in diameter is very strong and can be leveraged in accurate detection of GAG-GFP-VLP.

Chapter 5

Discussion

Previous work by Andrew Ng [62] investigated the production of two putative coronavirus VLPs using the baculovirus expression vector system: A SARS-CoV-2 VLP generated from the native S, E, and M genes, and a synthetic SARS-VLP generated from consensus S, E, and M sequences derived from SARS-CoV, MERS-CoV, and SARS-CoV-2. For the SARS-CoV-2 VLP construct, Western blot analysis confirmed the presence of all three structural proteins in the culture supernatant. Following iodixanol gradient ultracentrifugation, co-migration of the S and M proteins to the same fraction provided preliminary evidence for particle assembly. However, a sandwich ELISA using capture antibodies against baculovirus GP64 and detection antibodies against SARS-CoV-2 Spike also identified particles containing both proteins, raising the possibility that at least some of the observed material

represented decorated baculovirus rather than authentic VLPs. The synthetic SARS-VLP construct, which shares high sequence similarity with SARS-CoV-2 due to the predominance of SARS-CoV-2 sequences in the consensus design (see A.1), likewise showed the presence of S, E, and M proteins in the supernatant. However, no additional characterization was performed to confirm particle formation.

Given the uncertainty as to whether the particles observed in the previous study represented authentic VLPs or decorated baculovirus, additional recombinant baculoviruses were incorporated into the study to provide points of comparison. In addition to the baculovirus expressing the synthetic SARS-VLP, three recombinant baculoviruses expressing mKOκ, GAG, or GAG-GFP were evaluated. The mKOκ construct was selected as a negative control, as it was not expected to form VLPs, whereas GAG and GAG-GFP have both been reported to self-assemble into VLPs. The inclusion of these constructs enabled comparison between a system with no expected particle formation, systems with established VLP formation, and the putative SARS-VLP system. Furthermore, GAG-GFP VLPs are intrinsically fluorescent and have previously been detected by flow virometry, providing an orthogonal method for particle characterization and a benchmark against which the SARS-VLP system could be evaluated.

The primary hypothesis of this work was that the SARS structural proteins expressed in IC-BEVS self-assemble into VLPs. Consequently, particles produced by the SARS-

VLP construct were expected to behave similarly to HIV-derived GAG and GAG-GFP VLPs, which were expected to be similar in size and composition, during density gradient ultracentrifugation and subsequent characterization, while exhibiting properties distinct from those observed for the non-VLP-forming mKOκ control.

Additional controls consisted of uninfected insect cell cultures harvested at viabilities of 74% and 54% corresponding to the range of viabilities observed in infected cultures at harvest (73% for GAG-GFP VLP production and 60% for SARS-VLP prodcution). These controls were included to assess the extent to which particles arising from declining cell membrane integrity could contribute to the signals detected following density gradient ultracentrifugation. Although the causes of cell death differ between infected and uninfected cultures, viability in both cases was determined by trypan blue exclusion, a measure of cell membrane integrity. Following iodixanol density gradient ultracentrifugation, all samples were characterized by flow virometry, Western blotting, and multi-angle dynamic light scattering (MADLS).

5.1 Growth and Infection of cell cultures

Growth curves of all four types of infected sample showed halting of cell growth and a decline in the concentration of viable cells, which is consistent with baculovirus infection

(Figure 4.3). However, unlike other infected samples, viable cell concentration in cultures infected with rBEV-GAG-GFP remained similar from 48 to 72 HPI (Figure 4.3). This suggests that infection dynamics of rBEV-GAG-GFP may be dissimilar to other rBEVs examined in this work.

Medium in flasks that were infected with rBEV-mKOκ was visually observed to transition from yellow to an orange-red colour. After low g-force centrifugation to separate cells from the supernatant, the orange-red color was seen to remain with the cell pellet, and the supernatant returned to its original color. This is consistent with intracellular mKOκ expression in Sf9 cells. For GAG-GFP, the color of the media did not change significantly before and after low g-force centrifugation, indicating that a significant amount of GFP remained in the supernatant. These qualitative observations support that the infected cell cultures produced recombinant protein successfully.

Post-semi-purification density measurements confirmed that identically numbered fractions possessed similar densities across sample types and biological replicates (Figure 4.4). This validated that the density gradient's formation was consistent and samples can be meaningfully compared to others of identical fraction number. However, this was not necessarily the case for uninfected cultures that seemed to have a shift in density as of fraction 3 (Figure 4.4). This is important to note, as it may not be possible to compare fraction to fraction between uninfected and infected fractions. To be truly able to compare one

fraction to another, they should have the same density.

Furthermore, because Sf9 cells can remain in a stationary phase for a significant length of time periods before losing viability, abnormally long culture periods were needed to achieve viabilities that spanned the range of viabilities seen in the infected cultures. It is unclear how this long culture period may affect the accumulation of exosomes, Sf-rhabdovirus, or other particles through mechanisms that may be completely different than what occurs during a baculovirus infection.

5.2 Baculovirus and VLP Proteins in Iodixanol Fractions

Immunoblotting against GP64, P24, and Spike, the major structural proteins of baculovirus, HIV-VLPs, and SARS-VLPs respectively, revealed the presence of these proteins in fractions 2 – 5 (Figures 4.8, 4.9, 4.10, 4.11) corresponding to densities between 1.08 and 1.18 g/ml (Figure 4.4).

Testing for GP64, all infected samples showed the highest abundance of this protein in fraction 4. This aligns with expectations that baculovirus is produced in all infected samples and that their distribution post-semi-purification is the same. It should be noted as well that, although the transgenes being expressed differed in approximate size (657 bp

for rBEV-mKOκ, 1,500 bp for rBEV-GAG, 2,217 bp for rBEV-GAG-GFP, and 4,710 bp for rBEV-SARS), each insert represents only 0.5–3.5% of the approximately 134 kb AcMNPV genome [69, 70, 71, 72]. As a result, the overall recombinant genome size varied by approximately 3% across all constructs, and no substantial differences in baculovirus production or behaviour would be expected despite the different transgenes. This is consistent with the comparable GP64 distribution observed across all infected samples.

Detection of P24 in semi-purified GAG-VLP and GAG-GFP-VLP samples revealed unexpected differences. Signal intensity in GAG-GFP-VLP was up to five times greater than in GAG-VLP, depending on the fraction. Visually the Western blot of GAG-GFP-VLP showed multiple bands when compared to the single bands present in GAG-VLP. The fraction possessing the highest amount of P24 was 4 for GAG-VLP, and 3 for GAG-GFP-VLP. All these differences suggest that previous expectations of similarity between GAG-VLP and GAG-GFP-VLP samples may not be experimentally validated, and the cause warrants further investigation.

Spike protein detection in semi-purified SARS-VLP samples showed that fraction 4 had the highest concentration. This aligned with distribution patterns of GP64 and P24 in GAG-VLP, which suggests that Spike has been trafficked onto a particle that has similar purification behaviour to baculovirus and GAG-VLP but not GAG-GFP-VLP. Though GAG forms VLPs through interaction with the internal leaflet of the plasma membrane,

Spike and GP64 are anchored to the membrane and present on the exterior of their VLP and viral envelopes respectively [73, 74, 75]. This means that GAG may be unlikely to be trafficked onto baculovirus, however it is possible that Spike and GP64 are present on both baculovirus and VLPs. It has been shown in literature that GP64 can be pseudotyped onto GAG-VLPs, and thus immunoblotting alone is insufficient to determine successful formation of SARS-VLPs [75]. Despite these shortcomings immunoblotting suggests that these proteins are present on particles that have a range of densities between 1.08 g/mL and 1.18 g/mL.

The most enriched fractions (3 and 4, with densities of 1.10 g/mL and 1.13 g/mL) were somewhat less dense than GAG-VLP buoyant density reported in literature 1.16 g/mL in sucrose, this likely reflects the iso-osmotic property of iodixanol relative to sucrose [76]. It is known that enveloped VLPs undergo osmotic shrinkage in hypertonic gradients, which artificially increase their apparent density [77]. By using iodixanol as the density gradient forming medium, the osmotic pressure changes that would otherwise have been caused by sucrose are avoided and particles explored in this project should possess density most like their physiological state [77]. It is also of note that total protein content of each fraction could not be correlated to baculovirus nor VLPs specifically, indicating the presence of other cell culture-derived proteinaceous components present in fractions 1 - 6 (1.06 g/mL – 1.21 g/mL) (Figure 4.5). The presence of these proteins is an indicator that

the semi-purification workflow employed in this project is insufficient to completely purify contaminating cellular protein from VLP and baculovirus.

Flow virometry was performed using SYBR Green I dye to stain dsDNA, expected to predominantly correspond to baculovirus virions, since no other dsDNA-containing particles were expected to be present at significant concentrations in infected samples. Uninfected Sf9 samples did not present particle concentrations greater than the instrument limit of detection, consistent with the expectation that in the absence of infection, no baculovirus or other dsDNA-containing particles are present at a significant level. All four infected sample types yielded dsDNA-containing particles in fractions $2-5$, consistent with the expectation that baculovirus would be present regardless of transgene encoded (Figure 4.6). Distribution trends were similar across all infected samples types, with fraction 4 containing the peak concentration of dsDNA-containing particles. The GP64-targeted immunoblotting intensity aligned with the dsDNA-containing particle concentrations by flow virometry, offering increased confidence that both methods are detecting baculovirus virions.

Flow virometry was also performed on serially diluted samples of GAG-GFP-VLP exclusively, and particles possessing autofluorescence were detected. Due to the aforementioned propensity of GAG to self-assemble into GAG-VLPs with high exclusivity, it was expected that GAG-GFP-VLPs were the only source of fluorescent particles in the semi-purified sam-

ples. Samples showed presence of fluorescent particles ranging from fractions 2 – 5, with a peak concentration in fraction 3. The trend of GAG-GFP-VLP distribution is consistent with the trend observed for P24 signal intensity and distribution through immunoblotting, offering higher confidence that both methods are detecting GAG-GFP-VLPs.

5.3 MADLS identifies two distinct particle populations

The nature of the semi-purification protocol results in fractions with differential densities, leading to non-identical optical/physical properties. To obviate the need to measure viscosity and refractive index of each individual fraction for every unique sample, a range of iodixanol concentrations were generated to capture the various expected densities of particles to be separated. These samples were then characterized in terms of viscosity and refractive index, allowing relationships to be derived between density of the iodixanol-NTC medium and its refractive index or viscosity (Figures C.1, C.2, C.3). These relationships were tested and the corrections applied to MADLS measurements of defined concentrations of iodixanol-NTC medium, with clear effects on particle size and concentration as evidenced by the shifting of the iodixanol-dependent solvent peak towards its "true" value (Figure C.4).

When semi-purified fractions of the four infected and two uninfected sample types were

measured by MADLS and corrected for refractive index and viscosity, two particle classes emerged. Particles with a diameter between 50 nm and 250 nm (50 nm $<$ X $<$ 250 nm) and particles with particle diameter greater than 250 and less than 500 nm where (X $>$ 250 nm), consistent with expected size ranges of VLPs and baculovirus respectively [78, 57]. For infected samples of all virus types, confident measurements of (X $>$ 250 nm) particles were obtained in fractions 2 – 5, and for (50 nm $<$ X $<$ 250 nm) particles in fractions 2 – 4 (Figures C.22, C.23, C.20, C.21). These results are consistent with expectations that particles produced through IC-BEVS, VLPs and baculoviruses, can be detected by MADLS.

The expectation that samples from rBEV-mKOκ infection would possess particles that correspond to baculovirus virions seems to have been confirmed. Particles (X $>$ 250 nm) were distributed similarly across all infected samples and correlated well with the GP64 immunoblotting results. However, samples from rBEV-mKOκ infection, were expected to only have one type of particle detected by MADLS. Instead, like all other infected samples, two groups of particles having distinct sizes were observed (Figures C.22, C.23). The second group of particles having a size between 50 nm and 250 nm ($\sim$ 175 nm), did not correlate well with P24 for GAG-VLP or Spike for SARS-VLP; however, may correlate for GAG-GFP-VLP at a slightly larger size ($\sim$ 215 nm). This observation suggests that there may be a third particle type that was not accounted for in our design of experiments:

the presence of extracellular vesicles (EVs). Extracellular vesicles are getting significantly more attention of late and have been shown to be secreted by Sf9 cells as a response to baculovirus infection [79]. EVs are demonstrated to have diameters overlapping in size range with this class of particle.

A strong correlation was noted between particle concentration measurements via SYBR Green I flow virometry and MADLS for (X > 250 nm) particles. This supports the fact that both of these methods are detecting baculovirus since it is expected to contain dsDNA and be greater than 250 nm in diameter, however MADLS was shown to underestimate particle concentration for this particle class by a factor of 5 - 10 when compared to SYBR Green I flow virometry (Figure 4.20). Identical fraction numbers of, rBEV-mKOκ, rBEV-SARS-VLP, and rBEV-GAG-VLP were noted to have much closer spatial association than rBEV-GAG-GFP-VLP, indicating that those three samples are more alike than rBEV-GAG-GFP samples.

A strong correlation was observed between particle concentration measurements via fluorescence flow virometry and MADLS for particles between 50 nm and 250 nm in diameter. Since GAG-GFP-VLPs are expected to be the exclusive contributors to fluorescent particle concentration, this makes the near 1:1 agreement between the two methods very meaningful, and supports the expectation that GAG-GFP-VLPs make up the majority of the particles of this class in rBEV-GAG-GFP-VLP samples. The method agreement was

strongest in fractions 3 and 4, which both possessed the highest particle concentrations. In fraction 2 the GAG-GFP-VLP particle concentration is around 1.5 orders of magnitude lower than fractions 3 or 4, and its agreement is only slightly perturbed. This decrease in accuracy at lower particle concentrations for small particles is within expectations for an optical method such as MADLS.

5.4 GFP fusion alters GAG-VLP produced in IC-BEVS

A hypothesis of this work was that GAG-GFP-VLPs may be suitable as fluorescent surrogates for SARS-VLPs in the development of purification workflows. It was expected that GAG-GFP-VLPs would display the same particle distribution as GAG-VLPs and SARS-VLPs after semi-purification through iodixanol density gradient ultracentrifugation.

Peak concentrations for GAG-GFP occured in fraction 3 while all other samples had peaks in fraction 4. The majority of the GAG-GFP particles were less dense than their counterparts by approximately 0.03 g/mL. The agreement of MADLS, immunoblotting and fluorescence flow virometry also suggests that this was not simply a measurement artifact.

It is also important to note that the particles > 250 nm in diameter detected by MADLS, distribute similarly across all four infected samples (Figure C.22). This implies that the observed difference in particles between 50 nm and 250 nm may be indeed caused by the

presence of VLPs. Since the approximately 27 kDa GFP protein is fused to the C-terminus of each of the approximately 5000 copies of 55 kDa GAG polyproteins per VLP, it stands to reason that the volume of the VLP could be increased and the particle be less dense as a result, leading to migration to a less dense fraction post-semi-purification [64, 80].

The observation that a sample not expected to produce VLPs nevertheless generated particles in the 50 - 250 nm size range that were indistinguishable in size distribution, concentration, and density profile from samples expected to produce VLPs suggests a common origin for these particles. One possible explanation is that particle production in the IC-BEVS is driven, at least in part, by infection-induced extracellular vesicle (EV) secretion rather than exclusively by viral self-assembly mechanisms inherited from the source virus (Figure 5.1).

Such a model is biologically plausible. Baculovirus infection has been reported to alter vesicle trafficking and EV secretion in Sf9 cells, while both HIV-1 Gag and SARS-CoV-2 structural proteins are known to localize to cellular membranes and participate in membrane remodeling and budding processes [79, 73]. Rather than acting as the primary drivers of particle formation, these recombinant proteins may simply become incorporated into EVs generated by the infected cell. In this scenario, the proteins function less as architects of particle assembly and more as cargo that is recruited into pre-existing cellular budding pathways. These resultant particles may overlap in both size and density with

native EVs, and thus the definition of an IC-BEVS-derived VLP may rest exclusively on the divergence in production mechanism from VLPs derived of other systems.

This hypothesis also provides a potential explanation for why rBEV-SARS-VLP and rBEV-GAG-VLP systems, despite encoding structurally unrelated viral proteins that assemble through fundamentally different mechanisms in their native viruses, produce particles with remarkably similar densities, sizes, and concentrations. If the host cell's EV biogenesis machinery is the dominant determinant of particle formation, then the resulting particles would be expected to resemble one another regardless of the recombinant viral proteins they contain.

The deviation observed for rBEV-GAG-GFP-VLP particles may reflect the influence of the GFP fusion on particle formation. The increased molecular mass or steric constraints imposed by the GAG-GFP construct could alter membrane curvature, vesicle budding, or cargo loading, resulting in the production of larger particles.

If correct, this model has important implications for IC-BEVS process development. Efforts to optimize VLP production may need to consider not only the expression and assembly of recombinant structural proteins but also the underlying cellular pathways governing EV biogenesis and secretion, which may substantially contribute to the final particle population.

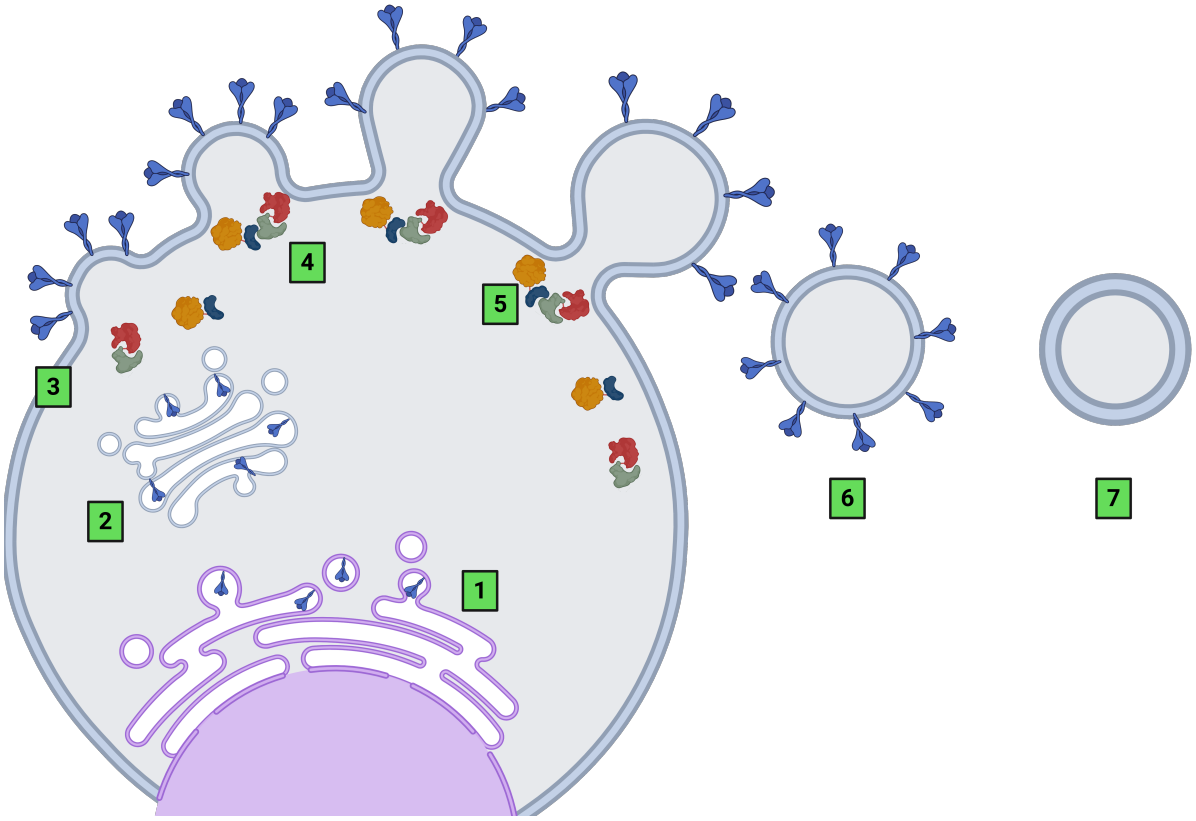

Figure 5.1: Proposed mechanism for production of enveloped VLPs in insect cell-baculovirus expression vector system, implicating existing extracellular vesicle (EV) secretion systems. 1) Rough endoplasmic reticulum synthesizes VLP major structural proteins (MSP). 2) Golgi body processes and directs MSP-embedded vesicles to the plasma membrane (PM). 3) Vesicles fuse with PM and MSPs are present on outer leaflet of the PM. 4) PM curvature induced by MSPs is exacerbated by endosomal sorting complex required for transport (ESCRT). 5) MSP-decorated extracellular vesicle (VLP-EV) buds off PM and ESCRT completes the process as it would in EV release. 6) VLP-EV is liberated into the extracellular milieu. 7) Undecorated EV for reference. [81, 82]

Chapter 6

Conclusions and Future Directions

In a system that makes both virus-like particles (VLPs) and baculovirus, and that both (enveloped VLPs and baculovirus) gain much of their attributes from the lipid membrane they inherit from the cell, how do you confirm you are making VLPs? We decided to attack this problem through the comparison of harvested supernatant from insect cells infected with 4 different baculoviruses: rBEV-SARS-VLP, rBEV-GAG, rBEV-GAG-GFP and rBEV-mKOκ. We chose two rBEVS that were thought to make VLPs and one that was thought to make intracellular protein. The central hypothesis was that rBEVs would be found in all four systems, while VLPs would only be found in 3 of the four systems. It was further hypothesized that a fluorescent GAG-GFP-VLP would exhibit separation characteristics similar to a non-fluorescent SARS-VLP, allowing the former to be used as

an easily visualizable surrogate for purification workflow production for the latter.

The objectives of this work included producing, semi-purifying and characterizing IC-BEVS-derived SARS-VLP, GAG-VLP, GAG-GFP-VLP and mKOκ using different and orthogonal methodologies. Non-fluorescent GAG-VLP samples showed remarkable similarities in separation behaviour to SARS-VLP samples across all methods trialed, which suggests that the IC-BEVS-derived envelope is able to share physical characteristics while retaining unique structural proteins. The fluorescent GAG-GFP-VLP possessed a different semi-purification distribution, likely due to the bulk introduced by the GFP moiety resulting in the particle density to decrease. The unexpected similarity of non-VLP producing rBEV-mKOκ to the VLP-producing samples in the particle class expected to contain VLPs supports the idea that EV secretion may be a mechanism for VLP production in IC-BEVS. If verified, this model may broaden the scope of diseases treated by proteins anchored in enveloped particles manufactured through IC-BEVS.

6.1 Semi-purification of recombinant products

Growth curves and media fluorescence-corresponding colour changes indicated successful infection of Sf9 cells with engineered baculovirus. Semi-purification through sucrose cushion and iodixanol density gradient ultracentrifugation were carried out followed by system-

atic fractionation. Density determination confirmed that fractions possessed consistent densities across samples and replicates, meaning direct comparison could be made against an identically numbered fraction. Immunoblotting confirmed presence of Spike, P24 and GP64 across fractions 2 – 5 for all infected samples, proving that both baculovirus and VLPs were co-produced. BCA assay was able to determine the presence of contaminating proteins in less dense fractions.

6.2 MADLS characterization of iodixanol fractions

MADLS was successfully demonstrated as an orthogonal quantitative method for characterizing IC-BEVS-derived particles. MADLS resolved two distinct particle populations in a single, complex biological sample (particles between 50 nm and 250 nm, and particles between 250 and 500 nm). For (50 nm $<$ X $<$ 250 nm) particles compared to fluorescence flow virometry, MADLS showed a nearly perfect agreement of particle concentration. For (X $>$ 250 nm) particles compared to SYBR Green I flow virometry, a strong correlation was observed with all infected samples, with rBEV-mKOκ, rBEV-GAG-VLP, rBEV-SARS-VLP creating a tight cluster. MADLS was shown to underestimate particle concentration for this class by a factor of 5 or less relative to SYBR Green I flow virometry. MADLS can be used to obtain particle size data, however it is more accurate to use SYBR Green I flow

virometry for accurate viral concentration results. A requirement of MADLS is knowledge of refractive index and viscosity parameters for each sample, which is essential to obtain accurate measurements. Once accounted for, MADLS becomes a rapid, reagent-free, and inexpensive sample assessment method that can improve the speed of purification workflow design.

6.3 An EV-based model for VLP production in IC-BEVS

GAG-GFP-VLPs do not possess the same biophysical properties as SARS-VLPs. Analytical methods including flow virometry, immunoblotting, and MADLS all point to the fact that GAG-GFP-VLPs are most concentrated in fraction 3, whereas SARS-VLPs, GAG-VLPs, and (50 nm $<$ X $<$ 250 nm) particles in rBEV-mKOκ are most concentrated in fraction 4. MADLS size data further exemplified the difference between GAG-GFP-VLPs and other infected sample types by comparing the average size of this same particle class in fraction 3, which for GAG-GFP-VLP was around 215 nm, compared to 175 nm on average for each of the other viruses. This size increase for GAG-GFP-VLP is logical since adding a GFP moiety would increase steric repulsion and cause the particle to become larger and less dense. GAG-VLP is shown to be consistent with SARS-VLP across all analytical tests, demonstrating that the only difference is the addition of the GFP on the GAG molecule

for GAG-GFP-VLPs, which is very likely to be cause of the separation behavior divergence from other infected samples.

The enormous similarities between the (50 nm $<$ X $<$ 250 nm) particles in the VLP-producing and non-VLP-producing samples suggest that a significant proportion of these particles in infected samples may result from a baculovirus-induced EV secretion mechanism. It is possible that VLP structural proteins become incorporated into the plasma membrane and become part of the EV as they are secreted. These findings emphasize that physical validation is essential prior to adoption of a fluorescent particle as a purification surrogate, and that the linkage between VLP production in the IC-BEVS may be more closely tied to infection-dependent EV secretion than previously thought. If host EV biogenesis is indeed the dominant route for VLP formation, and the possibility exists for a wide range of non-self-assembling proteins to be anchored to the membrane of an EV, then the IC-BEVS becomes a platform with versatility reaching far beyond VLP applications.

6.4 Study Limitations

Although a number of controls were included in this study, additional samples and measurements would have been beneficial. This study was unable to determine the infectious baculovirus titer in the different fractions, as bacterial contamination was observed in in-

fectious virus assays. The addition of virus activity would have given us additional insight as to where the baculovirus actually ended up. A second limitation is in our uninfected negative controls. Had we had additional replicates and harvest times, we could have modeled how the particles evolved over time to better match them to our infected samples. That stated, time-matching may not have provided a sufficient baseline for comparison either due to the unaccounted difference in dynamics associated with cell death. For the SARS-VLP characterization, we limited our work to detecting the Spike protein with conformational antibodies via dot blot. This served dual purposes: To assess preservation of native Spike protein structure post-purification and assess presence at a given density. This did not change the fact that it was impossible for this method alone to differentiate between particle types, hence fraction 4 possessing peak Spike protein content may have been contributed by pseudotyped baculovirus. Our results would be more compelling had we also did Western blot analysis of the S, E, and M proteins as well. This has been previously shown in Andrew Ng's work, who first studied SARS-CoV-2 VLPs and SARS VLPs in our lab, however, having those measurements here would have strengthened our assertion of the production of SARS- VLPs. For MADLS-based particle characterization, the major limitation was that populations reported were unable to be classified based on particle composition. This led to unreconcilable ambiguity within particle classes, since VLPs, EVs, and possibly apoptotic bodies may be contributing in unknown proportions to

the total particle concentration and average size of each class.

6.5 Future Directions

Widely utilized techniques may be contextualized and used to further characterize semi-purified samples. Sandwich ELISAs utilizing a combination of anti-S, anti-M, and anti-E could be used to confirm co-assembly of MSPs onto a single particle. ELISAs utilizing native receptors such as ACE2 as the capture agent would provide functional evidence that Spike on the SARS-VLP retains receptor-binding activity. Transmission electron microscopy showing the characteristic Spike-derived "corona" on SARS-VLP samples would provide direct structural confirmation of assembly and allow for further characterization of EV population in non-VLP-producing samples. Using immunoblotting to probe EV-specific proteins, such as subcomponents of Endosomal Sorting Complex Required for Transport (ESCRT), would deliver confirmation that EV secretion mechanisms are implicated in IC-BEVS VLP production. Live cell fluorescence microscopy could then be used to probe VLP MSPs and EV-specific proteins synchronously, allowing them to be co-visualized to determine if they are locally associated at membrane budding sites.

The purification workflow may be modified in an attempt to maximize resolution or minimize co-elution of various particles. An example of this is tuning of the iodixanol

density gradient to render it either more discrete with sharp and defined interfaces, or more continuous with gentle density changes. Both gradient modifications may have value in sample characterization, with the discrete providing less overlap between particle populations, and the continuous providing flatter distribution curves. Another possibility is that increasing the number of fractions collected may allow more granular observations to be made, such as a more precise density border at which a particle population no longer appears. This enables the determination of upper and lower bounds of densities of a given particle population.

However, beyond this, it is possible to investigate systems where baculovirus be reduced, such as in the work by [37], or using different cell lines such as the use of Hi5 cells. There is also opportunity to investigate removing one of the particle types using various size exclusion filters or affinity based removal of baculovirus particles.

References

[1] John Raphael Smith. Edward Jenner., 1800.

[2] Hongzhou Lu, Charles W. Stratton, and Yi-Wei Tang. Outbreak of pneumonia of unknown etiology in Wuhan, China: The mystery and the miracle. *Journal of Medical Virology*, 92(4):401–402, April 2020.

[3] Domenico Cucinotta and Maurizio Vanelli. WHO Declares COVID-19 a Pandemic. *Acta Bio Medica : Atenei Parmensis*, 91(1):157–160, 2020.

[4] World Health Organization. *World Health Statistics 2023: Monitoring Health for the SDGs, Sustainable Development Goals*. World Health Organization, Geneva, 1st ed edition, 2023.

[5] Manas Pustake, Isha Tambolkar, Purushottam Giri, and Charmi Gandhi. SARS, MERS and CoVID-19: An overview and comparison of clinical, laboratory and radio-

logical features. *Journal of Family Medicine and Primary Care*, 11(1):10–17, January 2022.

[6] Fatma Elrashdy, Elrashdy M. Redwan, and Vladimir N. Uversky. Why COVID-19 Transmission Is More Efficient and Aggressive Than Viral Transmission in Previous Coronavirus Epidemics? *Biomolecules*, 10(9):1312, September 2020.

[7] Health Canada. COVID-19 Vaccines: Authorized vaccines, December 2020. Last Modified: 2025-03-03.

[8] Andreas C. Chrysostomou, Bram Vrancken, Christos Haralambous, Maria Alexandrou, Antonia Aristokleous, Christina Christodoulou, Ioanna Gregoriou, Marios Ioannides, Olga Kalakouta, Christos Karagiannis, George Koumbaris, Charalambos Loizides, Michail Mendris, Panagiotis Papastergiou, Philippos C. Patsalis, Despo Pieridou, Jan Richter, Markus Schmitt, Christos Shammas, Dora C. Stylianou, Giorgos Themistokleous, Philippe Lemey, and Leondios G. Kostrikis. Genomic Epidemiology of the SARS-CoV-2 Epidemic in Cyprus from November 2020 to October 2021: The Passage of Waves of Alpha and Delta Variants of Concern. *Viruses*, 15(1):108, December 2022.

[9] Takahiko Koyama, Kei Miyakawa, Reitaro Tokumasu, Sundararaj S Jeremiah, Michiharu Kudo, and Akihide Ryo. Evasion of vaccine-induced humoral immunity by emerg-

ing sub-variants of SARS-CoV-2. *Future Microbiology*, 17:417–424, April 2022.

[10] David Cox. The hunt for a universal Covid-19 vaccine, January 2023.

[11] Eric Lewitus, Hongjun Bai, and Morgane Rolland. Design of a pan-betacoronavirus vaccine candidate through a phylogenetically informed approach. *Science Advances*, 9(3):eabq4149, January 2023.

[12] Colleen M. Flood, Bryan Thomas, and Kumanan Wilson. Mandatory vaccination for health care workers: an analysis of law and policy. *CMAJ : Canadian Medical Association Journal*, 193(6):E217–E220, February 2021.

[13] A. Roldão, A.C. Silva, M.C.M. Mellado, P.M. Alves, and M.J.T. Carrondo. Viruses and Virus-Like Particles in Biotechnology: Fundamentals and Applications. *Comprehensive Biotechnology*, pages 633–656, 2017.

[14] Braeden Donaldson, Farah Al-Barwani, Vivienne Young, Sarah Scullion, Vernon Ward, and Sarah Young. Virus-Like Particles, a Versatile Subunit Vaccine Platform. *Subunit Vaccine Delivery*, pages 159–180, August 2014.

[15] Marc G. Aucoin, Danielle Jacob, Parminder Singh Chahal, Jamal Meghrous, Alice Bernier, and Amine A. Kamen. Virus-like particle and viral vector production using the baculovirus expression vector system/insect cell system: adeno-associated virus-based products. *Methods in Molecular Biology*, 388:281–296, 2007.

[16] Emily M. Plummer and Marianne Manchester. Viral nanoparticles and virus-like particles: platforms for contemporary vaccine design. *Wiley Interdisciplinary Reviews. Nanomedicine and Nanobiotechnology*, 3(2):174–196, 2011.

[17] International Council for Harmonisation of Technical Requirements for Pharmaceuticals for Human Use and European Medicines Agency. ICH Q5A(R2) Guideline on viral safety evaluation of biotechnology products derived from cell lines of human or animal origin_step 5. *ICH Quality Guidelines*, 2023.

[18] Qiaonan Hong, Jian Liu, Yuquan Wei, and Xiawei Wei. Application of Baculovirus Expression Vector System (BEVS) in Vaccine Development. *Vaccines*, 11(7):1218, July 2023.

[19] Hasnat Tariq, Sannia Batool, Saaim Asif, Mohammad Ali, and Bilal Haider Abbasi. Virus-Like Particles: Revolutionary Platforms for Developing Vaccines Against Emerging Infectious Diseases. *Frontiers in Microbiology*, 12:790121, January 2022.

[20] Elisa Crisci, Juan Bárcena, and María Montoya. Virus-like particle-based vaccines for animal viral infections. *Inmunologia (Barcelona, Spain : 1987)*, 32(3):102–116, 2013.

[21] Catherine Demoliou, Christos Papaneophytou, and Vicky Nicolaidou. SARS-CoV-2 and HIV-1: So Different yet so Alike. Immune Response at the Cellular and Molecular Level. *International Journal of Medical Sciences*, 19(12):1787–1795, October 2022.

[22] Nail Minigulov, Kuandyk Boranbayev, Ayaulym Bekbossynova, Bakhytgul Gadilgereyeva, and Olena Filchakova. Structural proteins of human coronaviruses: what makes them different? *Frontiers in Cellular and Infection Microbiology*, 14:1458383, December 2024.

[23] David A. Jamison, S. Anand Narayanan, Nídia S. Trovão, Joseph W. Guarnieri, Michael J. Topper, Pedro M. Moraes-Vieira, Viktorija Zaksas, Keshav K. Singh, Eve Syrkin Wurtele, and Afshin Beheshti. A comprehensive SARS-CoV-2 and COVID-19 review, Part 1: Intracellular overdrive for SARS-CoV-2 infection. *European journal of human genetics: EJHG*, 30(8):889–898, August 2022.

[24] Luiza Mendonça, Andrew Howe, James B. Gilchrist, Dapeng Sun, Michael L. Knight, Laura C. Zanetti-Domingues, Benji Bateman, Anna-Sophia Krebs, Long Chen, Julika Radecke, Yuewen Sheng, Vivian D. Li, Tao Ni, Ilias Kounatidis, Mohamed A. Koronfel, Marta Szynkiewicz, Maria Harkiolaki, Marisa L. Martin-Fernandez, William James, and Peijun Zhang. SARS-CoV-2 Assembly and Egress Pathway Revealed by Correlative Multi-modal Multi-scale Cryo-imaging. *bioRxiv: The Preprint Server for Biology*, page 2020.11.05.370239, November 2020.

[25] Heather Swann, Abhimanyu Sharma, Benjamin Preece, Abby Peterson, Crystal Eldredge, David M. Belnap, Michael Vershinin, and Saveez Saffarian. Minimal system

for assembly of SARS-CoV-2 virus like particles. *Scientific Reports*, 10(1):21877, December 2020.

[26] Hai Trong Nguyen, Darryl Falzarano, Volker Gerdts, and Qiang Liu. Construction and immunogenicity of SARS-CoV-2 virus-like particle expressed by recombinant baculovirus BacMam. *Microbiology Spectrum*, 12(8):e00959–24, June 2024.

[27] Suzanne Scarlata and Carol Carter. Role of HIV-1 Gag domains in viral assembly. *Biochimica et Biophysica Acta (BBA) - Biomembranes*, 1614(1):62–72, July 2003.

[28] B. G. Turner and M. F. Summers. Structural biology of HIV. *Journal of Molecular Biology*, 285(1):1–32, January 1999.

[29] Ian B. Hogue, Jonathan R. Grover, Ferri Soheilian, Kunio Nagashima, and Akira Ono. Gag Induces the Coalescence of Clustered Lipid Rafts and Tetraspanin-Enriched Microdomains at HIV-1 Assembly Sites on the Plasma Membrane. *Journal of Virology*, 85(19):9749–9766, October 2011.

[30] Mariia Novikova, Yulan Zhang, Eric O. Freed, and Ke Peng. Multiple Roles of HIV-1 Capsid during the Virus Replication Cycle. *Virologica Sinica*, 34(2):119–134, April 2019.

[31] Sonia Gutiérrez-Granados, Laura Cervera, Francesc Gòdia, and María Mercedes Segura. Characterization and quantitation of fluorescent Gag virus-like particles. *BMC Proceedings*, 7(Suppl 6):P62, December 2013.

[32] Alina Venereo-Sanchez, Renald Gilbert, Melanie Simoneau, Antoine Caron, Parminder Chahal, Wangxue Chen, Sven Ansorge, Xuguang Li, Olivier Henry, and Amine Kamen. Hemagglutinin and neuraminidase containing virus-like particles produced in HEK-293 suspension culture: An effective influenza vaccine candidate. *Vaccine*, 34(29):3371–3380, June 2016.

[33] Jéromine Klingler, Halina Anton, Eléonore Réal, Manon Zeiger, Christiane Moog, Yves Mély, and Emmanuel Boutant. How HIV-1 Gag Manipulates Its Host Cell Proteins: A Focus on Interactors of the Nucleocapsid Domain. *Viruses*, 12(8):888, August 2020.

[34] Adam C. Chambers, Mine Aksular, Leo P. Graves, Sarah L. Irons, Robert D. Possee, and Linda A. King. Overview of the Baculovirus Expression System. *Current Protocols in Protein Science*, 91:5.4.1–5.4.6, February 2018.

[35] Joanna Kwiatkowska, Ewa Stein, Anastasiia Romanenko, Martyna Plens-Gałąska, Małgorzata Podsiadła-Białoskórska, Ewa Szołajska, Uwe Kühn, and Kinga Kamieniarz-Gdula. A beginners guide to Sf9 and Sf21 insect cell line culture and troubleshooting. *Scientific Reports*, 15:19907, June 2025.

[36] Ricardo Correia, Taja Zotler, Francisco Ferraz, Bárbara Fernandes, Miguel Graça, Gorben P. Pijlman, Paula M. Alves, and António Roldão. Continuous Production of Influenza VLPs Using IC-BEVS and Multi-Stage Bioreactors. *Biotechnology and Bioengineering*, 122(4):846–857, April 2025.

[37] Mark R. Bruder and Marc G. Aucoin. Evaluation of Virus-Free Manufacture of Recombinant Proteins Using CRISPR-Mediated Gene Disruption in Baculovirus-Infected Insect Cells. *Vaccines*, 11(2):225, January 2023.

[38] Thomas A. Kost and Christopher W. Kemp. Fundamentals of Baculovirus Expression and Applications. In M. Cristina Vega, editor, *Advanced Technologies for Protein Complex Production and Characterization*, pages 187–197. Springer International Publishing, Cham, 2016.

[39] Carissa Grose, Zoe Putman, and Dominic Esposito. A Review of Alternative Promoters for Optimal Recombinant Protein Expression in Baculovirus-infected Insect Cells. *Protein expression and purification*, 186:105924, October 2021.

[40] Jean-Christophe Drugmand, Yves-Jacques Schneider, and Spiros N. Agathos. Insect cells as factories for biomanufacturing. *Biotechnology Advances*, 30(5):1140–1157, September 2012.

[41] José G. Hernández-Cifre, Ricardo Rodríguez-Schmidt, Carmen M. Almagro-Gómez, and José García de la Torre. Calculation of the friction, diffusion and sedimentation coefficients of nanoplatelets of arbitrary shape. *Polymer*, 262:125467, December 2022.

[42] Alexander E. Yarawsky, Paola Cardenas Lopez, Johannes Walter, Michael T. DeLion, and Lake N. Paul. A fundamental approach to buoyant density determination by DGE-AUC. *Analytical Biochemistry*, 704:115907, September 2025.

[43] Tiago Vicente, António Roldão, Cristina Peixoto, Manuel J. T. Carrondo, and Paula M. Alves. Large-scale production and purification of VLP-based vaccines. *Journal of Invertebrate Pathology*, 107:S42–S48, July 2011.

[44] Hans J. Kueng, Victoria M. Leb, Daniela Haiderer, Graça Raposo, Clotilde Thery, Sophia V. Derdak, Klaus G. Schmetterer, Alina Neunkirchner, Christian Sillaber, Brian Seed, and Winfried F. Pickl. General Strategy for Decoration of Enveloped Viruses with Functionally Active Lipid-Modified Cytokines. *Journal of Virology*, 81(16):8666–8676, August 2007.

[45] Kwan-Jip Kim, Gijeong Kim, Jin-Ho Bae, Ji-Joon Song, and Hak-Sung Kim. A pH-Responsive Virus-Like Particle as a Protein Cage for a Targeted Delivery. *Advanced Healthcare Materials*, 13(4):2302656, February 2024.

[46] Renata Gois de Mello, Thaissa Consoni Bernardino, Luis Giovani Oliveira Guardalini, Renato Mancini Astray, Marta Maria Antoniazzi, Simone Gonçalves Silva Jared, Eutimio Gustavo Fernández Núñez, and Soraia Attie Calil Jorge. Zika virus-like particles (VLPs) produced in insect cells. *Frontiers in Pharmacology*, 14:1181566, June 2023.

[47] Christopher A. Gonelli, Georges Khoury, Rob J. Center, and Damian F.J. Purcell. HIV-1-Based Virus-like Particles that Morphologically Resemble Mature, Infectious HIV-1 Virions. *Viruses*, 11(6):507, June 2019.

[48] Al Charest. Experimental and Biological Insights from Proteomic Analyses of Extracellular Vesicle Cargos in Normalcy and Disease. *Advanced biosystems*, 4(12):e2000069, December 2020.

[49] Malvern Panalytical. Multi-angle Dynamic Light Scattering (MADLS) on the Zetasizer Ultra – How it Works. Malvern Panalytical Knowledge Center, 2018-07-19.

[50] Sven Falke and Christian Betzel. Dynamic Light Scattering (DLS). *Radiation in Bioanalysis*, 8:173–193, July 2019.

[51] Ashutosh Sharma, Jason Beirne, Dikshitkumar Khamar, Ciaran Maguire, Ambrose Hayden, and Helen Hughes. Evaluation and Screening of Biopharmaceuticals using Multi-Angle Dynamic Light Scattering. *AAPS PharmSciTech*, 24(4):84, March 2023.

[52] Jake Austin, Caterina Minelli, Douglas Hamilton, Magdalena Wywijas, and Hanna Jankevics Jones. Nanoparticle number concentration measurements by multi-angle dynamic light scattering. *Journal of Nanoparticle Research*, 22(5):108, May 2020.

[53] Christine L. Plavchak, Allison Z. Werner, Elizabeth Betz, Davinia Salvachúa, Gregg T. Beckham, and S. Kim Ratanathanawongs Williams. Determination of particle number concentration for biological particles using AF4-MALS: Dependencies on light scattering model and refractive index. *Journal of Chromatography A*, 1737:465460, November 2024.

[54] Malvern Panalytical. Determining Dispersant Viscosity Using Dynamic Light Scattering. Malvern Panalytical Knowledge Center, 2010-11-04.

[55] Alina Venereo-Sanchez, Melanie Simoneau, Stéphane Lanthier, Parminder Chahal, Lucie Bourget, Sven Ansorge, Rénald Gilbert, Olivier Henry, and Amine Kamen. Process intensification for high yield production of influenza H1N1 Gag virus-like particles using an inducible HEK-293 stable cell line. *Vaccine*, 35(33):4220–4228, July 2017.

[56] Edward Sullivan, Po-Yu Sung, Weining Wu, Neil Berry, Sarah Kempster, Deborah Ferguson, Neil Almond, Ian M. Jones, and Polly Roy. SARS-CoV-2 Virus-like Particles

Produced by a Single Recombinant Baculovirus Generate Anti-S Antibody and Protect against Variant Challenge. *Viruses*, 14(5):914, April 2022.

[57] Youjun Mi, Tao Xie, Bingdong Zhu, Jiying Tan, Xuefeng Li, Yanping Luo, Fei Li, HongXia Niu, Jiangyuan Han, Wei Lv, and Juan Wang. Production of SARS-CoV-2 virus-like particles in insect cells, February 2021. Pages: 2021.01.30.428979 Section: New Results.

[58] L. Buonaguro, F. M. Buonaguro, M. L. Tornesello, D. Mantas, E. Beth-Giraldo, R. Wagner, S. Michelson, M. C. Prevost, H. Wolf, and G. Giraldo. High efficient production of Pr55gag virus-like particles expressing multiple HIV-1 epitopes, including a gp120 protein derived from an Ugandan HIV-1 isolate of subtype A. *Antiviral Research*, 49(1):35–47, January 2001.

[59] Ruodan Xu, Mingfei Shi, Jing Li, Ping Song, and Ning Li. Construction of SARS-CoV-2 Virus-Like Particles by Mammalian Expression System. *Frontiers in Bioengineering and Biotechnology*, 8:862, July 2020.

[60] Stefan Hirschberg, Fatemeh Ghazaani, Ghada Ben Amor, Markus Pydde, Alexander Nagel, Saveria Germani, Lara Monica, Anja Schlör, Hannes Bauer, Jane Hornung, Michael Voetz, Yamen Dwai, Benjamin Scheer, Frauke Ringel, Omar Kamal-Eddin, Christoph Harms, Jonas Füner, Lorenz Adrian, Axel Pruß, Kai Schulze-Forster, Katja

Hanack, and Julian Kamhieh-Milz. An Efficient and Scalable Method for the Production of Immunogenic SARS-CoV-2 Virus-like Particles (VLP) from a Mammalian Suspension Cell Line. *Vaccines*, 11(9):1469, September 2023.

[61] Edward Sullivan, Po-Yu Sung, Weining Wu, Neil Berry, Sarah Kempster, Deborah Ferguson, Neil Almond, Ian M. Jones, and Polly Roy. SARS-CoV-2 Virus-like Particles Produced by a Single Recombinant Baculovirus Generate Anti-S Antibody and Protect against Variant Challenge. *Viruses*, 14(5):914, April 2022.

[62] Andrew Ng. The Construction and Characterization of a Synthetic SARS VLP Comprised of Betacoronavirus Consensus Sequence-Encoded Viral Components. Master's thesis, Waterloo, 2022.

[63] Mark Bruder. *Toward Optimization of the Baculovirus Expression Vector System - Development of Genetic Tools to Improve Biologics Production.* PhD thesis, Waterloo, 2021.

[64] Mark R. Bruder and Marc G. Aucoin. Evaluation of Virus-Free Manufacture of Recombinant Proteins Using CRISPR-Mediated Gene Disruption in Baculovirus-Infected Insect Cells. *Vaccines*, 11(2):225, February 2023.

[65] JH Seinfeld and SN Pandis. *Atmospheric chemistry and physics: From air pollution to climate change.* John Wiley & Sons, 2006.

[66] Andreas Baer, Simon E. Wawra, Kristina Bielmeier, Maximilian J. Uttinger, David M. Smith, Wolfgang Peukert, Johannes Walter, and Ana-Sunčana Smith. The Stokes–Einstein–Sutherland Equation at the Nanoscale Revisited. *Small*, 20(6):2304670, 2024. _eprint: https://onlinelibrary.wiley.com/doi/pdf/10.1002/smll.202304670.

[67] Craig F. Bohren and Donald R. Huffman. Rayleigh-Gans Theory. In *Absorption and Scattering of Light by Small Particles*, pages 158–165. John Wiley & Sons, Ltd, 1998. Section: 6 _eprint: https://onlinelibrary.wiley.com/doi/pdf/10.1002/9783527618156.ch6.

[68] Ilze Oshina and Janis Spigulis. Beer–Lambert law for optical tissue diagnostics: current state of the art and the main limitations. *Journal of Biomedical Optics*, 26(10):100901, October 2021.

[69] Jennifer A. Aguiar. Betacoronavirus consensus sequence. Unpublished raw sequence data, 2020.

[70] Jonathan M. Geisinger, Sören Turan, Sophia Hernandez, Laura P. Spector, and Michele P. Calos. *In vivo* blunt-end cloning through CRISPR/Cas9-facilitated non-homologous end-joining. *Nucleic Acids Research*, 44(8):e76–e76, May 2016.

[71] M.D. Resh and G. Pavlakis. NIH AIDS Reagent Program, Division of AIDS, NIAID, NIH: pGag-EGFP (cat no.11468).

[72] Ajay B. Maghodia, Donald L. Jarvis, and Christoph Geisler. Complete Genome Sequence of the Autographa californica Multiple Nucleopolyhedrovirus Strain E2. *Genome Announcements*, 2(6):e01202–14, December 2014.

[73] Ian B. Hogue, Jonathan R. Grover, Ferri Soheilian, Kunio Nagashima, and Akira Ono. Gag Induces the Coalescence of Clustered Lipid Rafts and Tetraspanin-Enriched Microdomains at HIV-1 Assembly Sites on the Plasma Membrane ▽. *Journal of Virology*, 85(19):9749–9766, October 2011.

[74] Shuvomoy Banerjee, Xinyu Wang, Shujuan Du, Caixia Zhu, Yuping Jia, Yuyan Wang, and Qiliang Cai. Comprehensive role of SARS-CoV-2 spike glycoprotein in regulating host signaling pathway. *Journal of Medical Virology*, 94(9):4071–4087, September 2022.

[75] Ziyaad Valley-Omar, Ann E Meyers, Enid G Shephard, Anna-Lise Williamson, and Edward P Rybicki. Abrogation of contaminating RNA activity in HIV-1 Gag VLPs. *Virology Journal*, 8:462, October 2011.

[76] Lynn Rasmussen, Jane K Battles, Willis H Ennis, Kunio Nagashima, and Matthew A Gonda. Characterization of virus-like particles produced by a recombinant bac-

ulovirus containing the *gag* gene of the bovine immunodeficiency-like virus. *Virology*, 178(2):435–451, October 1990.

[77] Hyo-Jick Choi, Jae-Min Song, Brian J. Bondy, Richard W. Compans, Sang-Moo Kang, and Mark R. Prausnitz. Effect of Osmotic Pressure on the Stability of Whole Inactivated Influenza Vaccine for Coating on Microneedles. *PLOS ONE*, 10(7):e0134431, July 2015.

[78] Dayanand B. Sajjan and Shivayogeppa B. Hinchigeri. Structural Organization of Baculovirus Occlusion Bodies and Protective Role of Multilayered Polyhedron Envelope Protein. *Food and Environmental Virology*, 8(1):86–100, March 2016.

[79] Lex J. C. Van Es, Robert D. Possee, and Linda A. King. Characterisation of extracellular vesicles in baculovirus infection of Spodoptera frugiperda cells. *Journal of Extracellular Biology*, 3(7):e163, June 2024.

[80] W. Uckert, L. Pedersen, and W. Günzburg. Green fluorescent protein retroviral vector : generation of high-titer producer cells and virus supernatant. *Methods in Molecular Medicine*, 35:275–285, 2000.

[81] James H. Hurley and A. King Cada. Inside Job: How the ESCRTs release HIV-1 from infected cells. *Biochemical Society transactions*, 46(5):1029–1036, October 2018.

[82] N.R. Cheng. Vlp-ev mechanism. Unpublished image created in BioRender adapted from 10.1042/BST20180019, 2026.

[83] PubChem. S - surface glycoprotein (Severe acute respiratory syndrome coronavirus 2), 2020.

[84] NCBI RefSeq. envelope protein (Severe acute respiratory syndrome coronavirus 2), 2020.

[85] NCBI RefSeq. membrane glycoprotein (Severe acute respiratory syndrome coronavirus 2), 2020.

[86] CF Shen, Meghrous J, and Kamen A. Quantitation of baculovirus particles by flow cytometry. *Journal of Virological Methods*, 105:321–330, Sep 2002.

APPENDICES

Appendix A

General

A.1 Consensus SARS-CoV-2 Sequences

Table A.1: Comparison between wild-type and consensus-based SARS-CoV-2 major structural proteins

Major Structural Protein	Wild-Type	Consensus	Sequence Identity %	Reference
Spike	MFVFLVLLPLVSSQCVNLTTRTQLPPAYTNSFTRGVYYP DKVFRSSVLHSTQDLFLPFFSNVTWFHAIHVSGTNGTKR FDNPVLPFNDGVYFASTEKSNIIRGWIFGTTLDSKTQSLLI VNNATNVVIKVCEFQFCNDPFLGVYYHKNNKSWMESEF RVYSSANNCTFEYVSQPFLMDLEGKQGNFKNLREFVFK NIDGYFKIYSKHTPINLVRDLPQGFSALEPLVDLPIGINITR FQTLLALHRSYLTPGDSSSGWTAGAAAYYVGYLQPRTFL LKYNENGTITDAVDCALDPLSETKCTLKSFTVEKGIYQTS NFRVQPTESIVRFPNITNLCPFGEVFNATRFASVYAWNR KRISNCVADYSVLYNSASFSTFKCYGVSPTKLNDLCFTNV YADSFVIRGDEVRQIAPGQTGKIADYNYKLPDDFTGCVI AWNSNNLDSKVGGNYNYLYRLFRKSNLKPFERDISTEIY QAGSTPCNGVEGFNCYFPLQSYGFQPTNGVGYQPYRVV VLSFELLHAPATVCGPKKSTNLVKNKCVNFNFNGLTGT GVLTESNKKFLPFQQFGRDIADTTDAVRDPQTLEILDITP CSFGGVSVITPGTNTSNQVAVLYQDVNCTEVPVAIHADQ LTPTWRVYSTGSNVFQTRAGCLIGAEHVNNSYECDIPIG AGICASYQTQTNSPRRARSVASQSIIAYTMSLGAENSVAY SNNSIAIPTNFTISVTTEILPVSMTKTSVDCTMYICGDSTE CSNLLLQYGSFCTQLNRALTGIAVEQDKNTQEVFAQVKQ IYKTPPIKDFGGFNFSQILPDPSKPSKRSFIEDLLFNKVTL ADAGFIKQYGDCLGDIAARDLICAQKFNGLTVLPPLLTD EMIAQYTSALLAGTITSGWTFGAGAALQIPFAMQMAYRF NGIGVTQNVLYENQKLIANQFNSAIGKIQDSLSSTASALG KLQDVVNQNAQALNTLVKQLSSNFGAISSVLNDILSRLDK VEAEVQIDRLITGRLQSLQTYVTQQLIRAAEIRASANLAA TKMSECVLGQSKRVDFCGKGYHLMSFPQSAPHGVVFLH VTYVPAQEKNFTTAPAICHDGKAHFPREGVFVSNGTHW FVTQRNFYEPQIITTDNTFVSGNCDVVIGIVNNTVYDPLQ PELDSFKEELDKYFKNHTSPDVDLGDISGINASVVNIQKEI DRLNEVAKNLNESLIDLQELGKYEQYIKWPWYIWLGFIA GLIAIVMVTIMLCCMTSCCSCLKGCCSCGSCCKFDEDDSE PVLKGVKLHYT	MFVFLVLLPLVSSQCVNLTTRTQLPPAYTNSFTRGVYY PDKVFRSSVLHSTQDLFLPFFSNVTWFHAIHVSGTNGT KRFDNPVLPFNDGVYFASTEKSNIIRGWIFGTTLDSKT QSLLIVNNATNVVIKVCEFQFCNDPFLGVYYHKNNKSW MESEFRVYSSANNCTFEYVSQPFLMDLEGKQGNFKNL REFVFKNIDGYFKIYSKHTPINLVRDLPQGFSALEPLVD LPIGINITRFQTLLALHRSYLTPGDSSSGWTAGAAAYYV GYLQPRTFLLKYNENGTITDAVDCALDPLSETKCTLKS FTVEKGIYQTSNFRVQPTESIVRFPNITNLCPFGEVFNA TRFASVYAWNRKRISNCVADYSVLYNSASFSTFKCYGV SPTKLNDLCFTNVYADSFVIRGDEVRQIAPGQTGKIAD YNYKLPDDFTGCVIAWNSNNLDSKVGGNYNYLYRLFR KSNLKPFERDISTEIYQAGSTPCNGVEGFNCYFPLQSYG FQPTNGVGYQPYRVVVLSFELLHAPATVCGPKKSTNL VKNKCVNFNFNGLTGTGVLTESNKKFLPFQQFGRDIA DTTDAVRDPQTLEILDITPCSFGGVSVITPGTNTSNQVA VLYQGVNCTEVPVAIHADQLTPTWRVYSTGSNVFQTR AGCLIGAEHVNNSYECDIPIGAGICASYQTQTNSPRRAR SVASQSIIAYTMSLGAENSVAYSNNSIAIPTNFTISVTTEI LPVSMTKTSVDCTMYICGDSTECSNLLLQYGSFCTQLN RALTGIAVEQDKNTQEVFAQVKQIYKTPPIKDFGGFNF SQILPDPSKPSKRSFIEDLLFNKVTLADAGFIKQYGDCL GDIAARDLICAQKFNGLTVLPPLLTDEMIAQYTSALLA GTITSGWTFGAGAALQIPFAMQMAYRFNGIGVTQNVL YENQKLIANQFNSAIGKIQDSLSSTASALGKLQDVVNQN AQALNTLVKQLSSNFGAISSVLNDILSRLDKVEAEVQID RLITGRLQSLQTYVTQQLIRAAEIRASANLAATKMSECV LGQSKRVDFCGKGYHLMSFPQSAPHGVVFLHVTYVPA QEKNFTTAPAICHDGKAHFPREGVFVSNGTHWFVTQR NFYEPQIITTDNTFVSGNCDVVIGIVNNTVYDPLQPELD SFKEELDKYFKNHTSPDVDLGDISGINASVVNIQKEIDR LNEVAKNLNESLIDLQELGKYEQYIKWPWYIWLGFIAG LIAIVMVTIMLCCMTSCCSCLKGCCSCGSCCKFDEDDSE PVLKGVKLHYT	99.99%	[83], [69]
Envelope	MYSFVSEETGTLIVNSVLLFLAFVVFLLVTLAILTALRLCA YCCNIVNVSLVKPSFYVYSRVKNLNSSRVPDLLV	MYSFVSEETGTLIVNSVLLFLAFVVFLLVTLAILTALRLC AYCCNIVNVSLVKPSFYVYSRVKNLNSSRVPDLLV	100.00%	[84], [69]
Membrane	MADSNGTITVEELKKLLEQWNLVIGFLFLTWICLLQFAY ANRNRFLYIIKLIFLWLLWPVTLACFVLAAVYRINWITGG IAIAMACLVGLMWLSYFIASFRLFARTRSMWSFNPETNIL LNVPLHGTILTRPLLESELVIGAVILRGHLRIAGHHLGRCD IKDLPKEITVATSRTLSYYKLGASQRVAGDSGFAAYSRYR IGNYKLNTDHSSSSDNIALLVQ	MADSNGTITVEELKKLLEQWNLVIGFLFLTWICLLQFA YANRNRFLYIIKLIFLWLLWPVTLACFVLAAVYRINWIT GGIAIAMACLVGLMWLSYFIASFRLFARTRSMWSFNPE TNILLNVPLHGTILTRPLLESELVIGAVILRGHLRIAGHH LGRCDIKDLPKEITVATSRTLSYYKLGASQRVAGDSGF AAYSRYRIGNYKLNTDHSSSSDNIALLVQ	100.00%	[85], [69]

Appendix B

Flow Virometry

B.1 Equations

B.1.1 Calculations associated with SYBR green staining of baculovirus particles

The number of particles present in a sample using data generated from flow virometry can be calculated via the following equation as previously described [86]

$$\text{Particle Concentration (Particles / mL)} = \frac{C_v \cdot D \cdot 1000 \cdot 50000}{C_f \cdot V_{ol}} \qquad \text{(AE-1)}$$

Where:

Cv is particle count for stained particles

Cf is particle count for Flowset

D is dilution ratio of the sample

Vol is volume of diluted sample in microliters

1000 is the final volume of analyzed sample in microliters

50000 is the particle concentration of the diluted flowset

This equation can be modified based on the needs of the experiment, and be used to detect both SYBR Green-stained or fluorescent particles.

B.2 Supplementary Results

B.2.1 Infected Cell Culture Supernatant Characterization

Flow virometry techniques were used to assess particle concentration within infected cell culture supernatant.

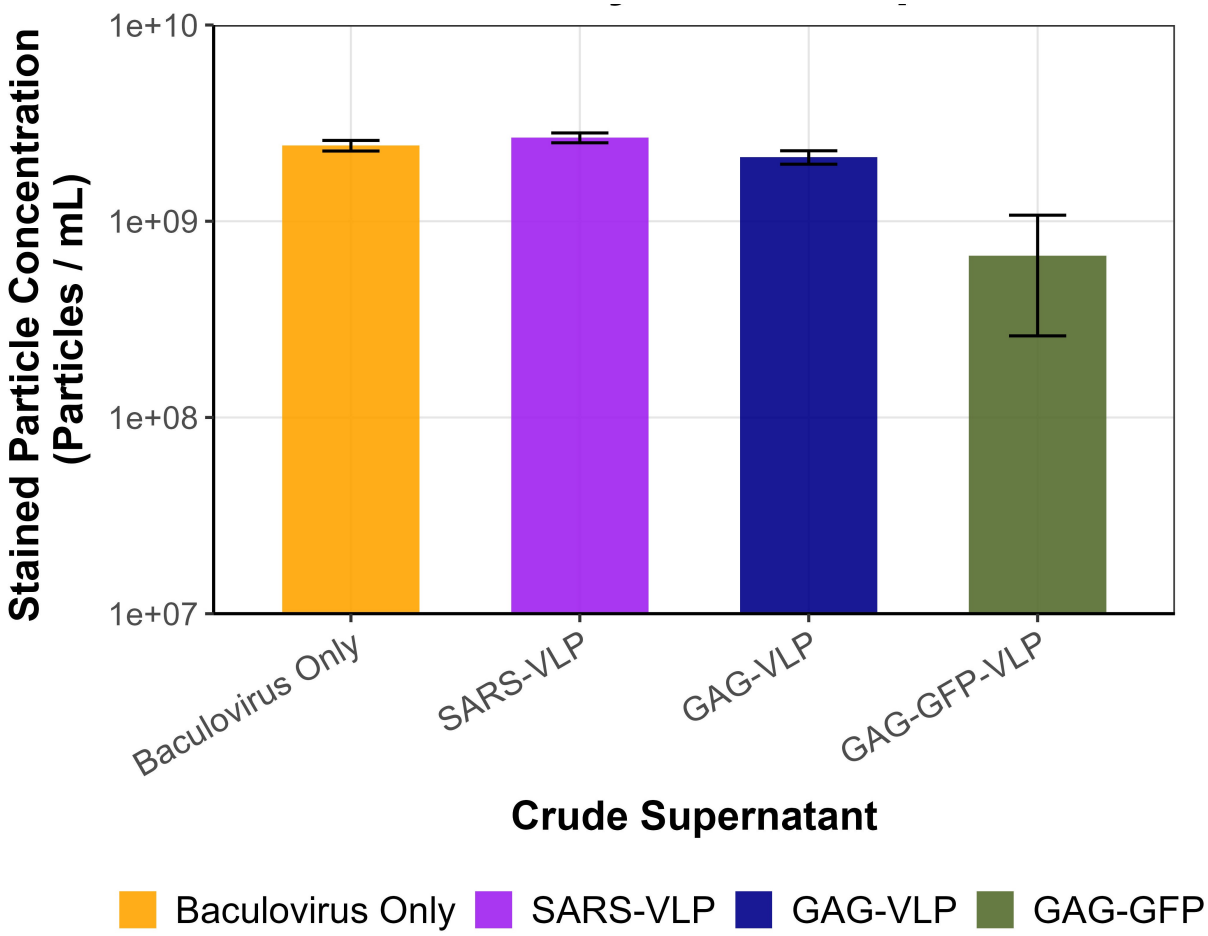

Figure B.1: Flow virometry-derived dsDNA-containing particle concentration in infected cell culture supernatant samples. Baculovirus Only / rBEV-mKOκ (orange), GAG-VLP (blue), GAG-GFP-VLP (green), SARS-VLP (purple). Samples stained with SYBR Green I dye to detect dsDNA-containing particles. Error bars represent biological triplicates.

SYBR Green I stained flow virometry enabled determination of concentration of particles containing dsDNA. All rBEV samples appeared to contain dsDNA-containing particles around $5*10^9$ particles/mL (Figure B.1). rBEV-GAG-GFP-VLP samples possessed a much lower value, approximately $8*10^8$ particles/mL with a larger variability between biological replicates. This suggests that the expression of GAG-GFP-VLP may be hampering the titer of baculovirus produced more significantly than recombinant proteins and VLPs in other rBEVs.

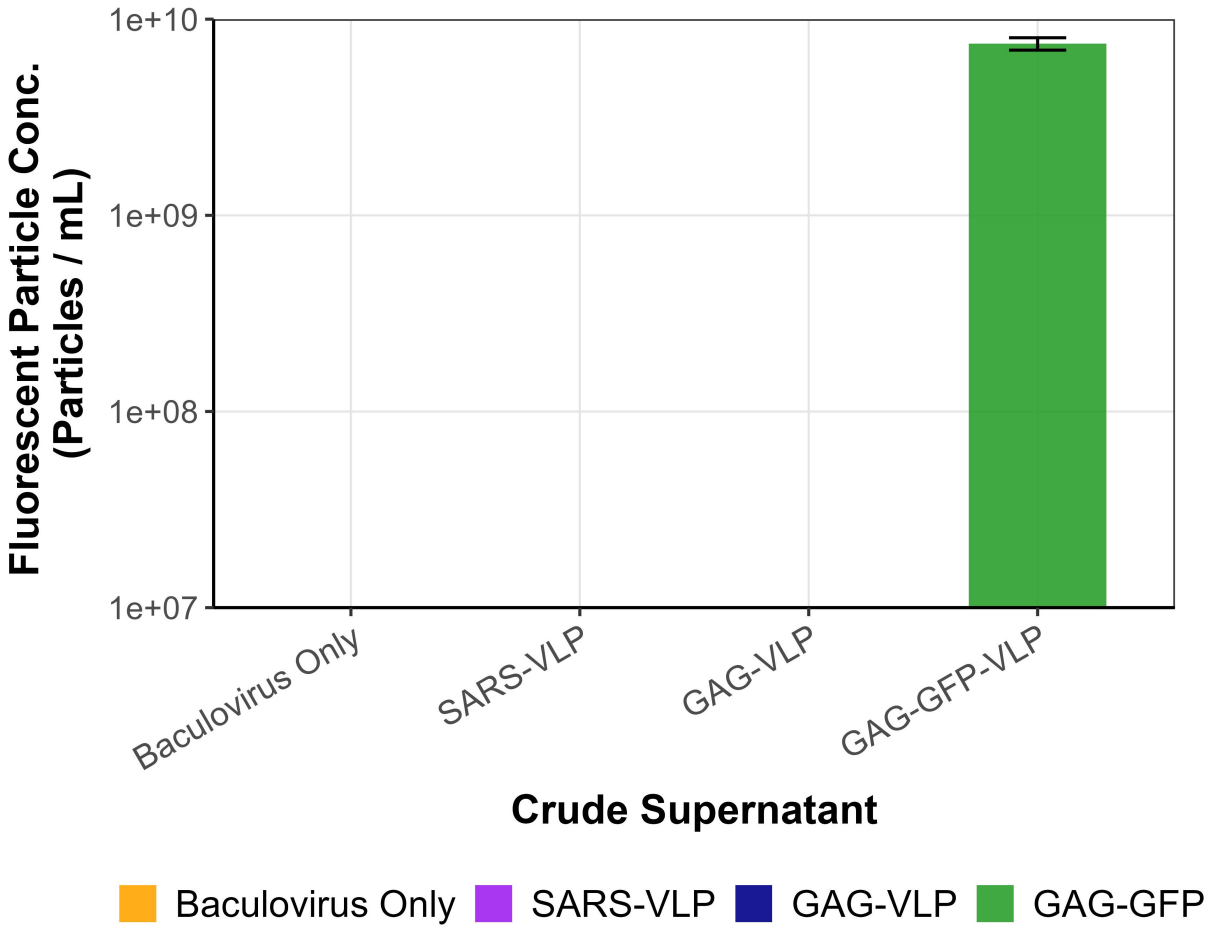

Figure B.2: Flow virometry-derived fluorescent particle concentration infected cell culture supernatant samples. Fluorescent particles in GAG-GFP-VLP (light green). Fluorescent flow virometry of non-fluorescent samples yielded data lower than the instrument LOD ($1.5 * 10^8$ Particles/mL) data not shown. Error bars represent biological replicates.

Fluorescence flow viromtery enabled determination of concentration of fluorescent particles, which are likely GAG-GFP-VLPs in this context. No meaningful detection of fluorescent particles in samples other than GAG-GFP-VLP was observed, in line with expectations (Figure B.2). The GAG-GFP-VLP concentration detected appeared to be around $8 * 10^9$ particles/mL. This suggests that the methodology works as intended, and that particles containing GAG-GFP which are likely to be GAG-GFP-VLPs, can be detected effectively.

B.2.2 Semi-Purification Characterization

Two stages of semi-purification are performed in this project: Sucrose cushion ultracentrifugation and iodixanol density gradient ultracentrifugation. After sucrose cushion ultracentrifugation, the pellet is resuspended in 1 X NTC buffer, and subjected to iodixanol density gradient ultracentrifugation. Flow virometry was used to compare the % yield of particles present before and after each stage, where particle concentrations in infected cell culture supernatant were used to normalize yield %. Yield % of all semi-purified fractions were added to generate the total yield % of the iodixanol.

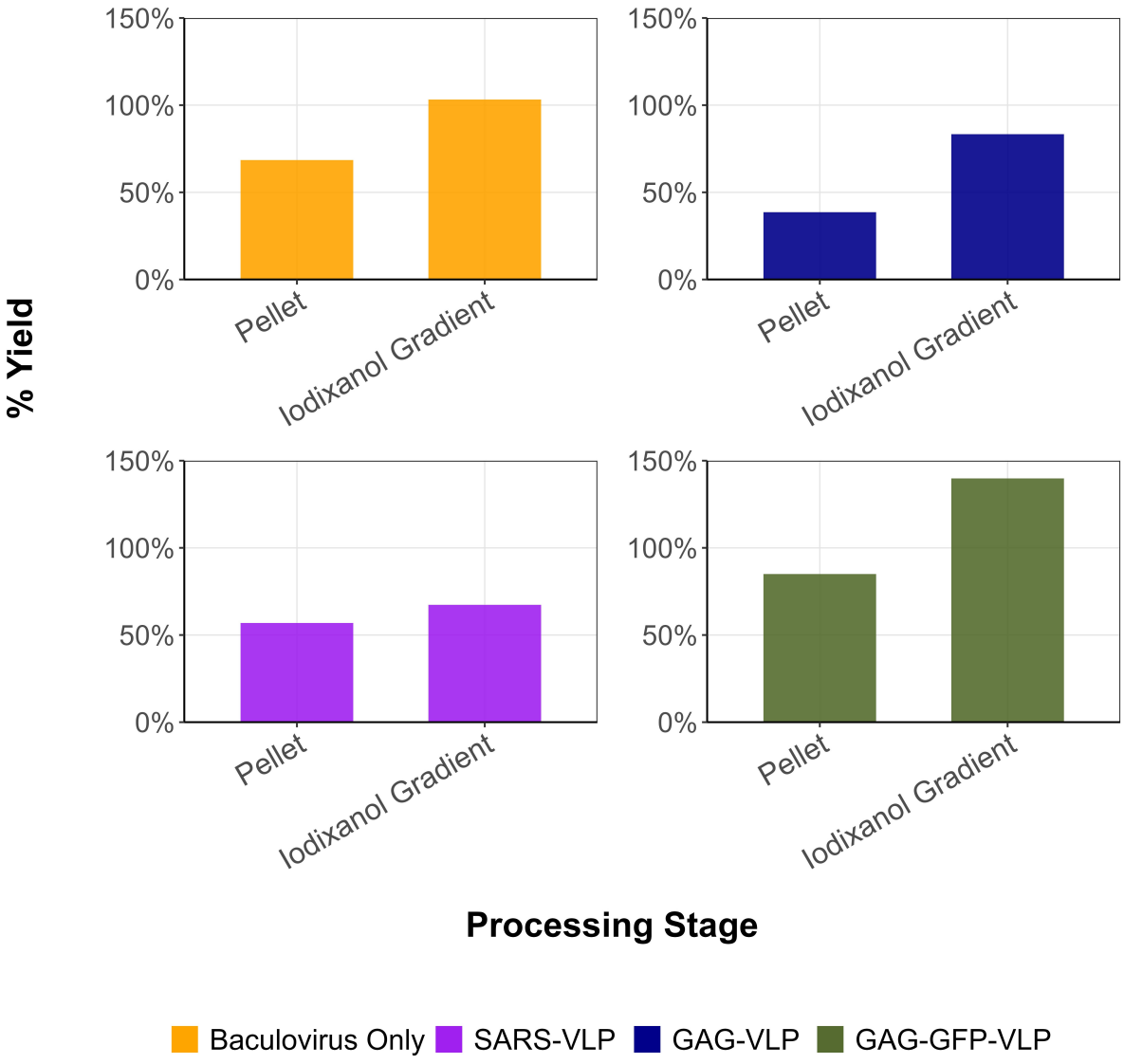

Figure B.3: Flow virometry-derived dsDNA-containing particle yield percentages at semi-purification stages. Baculovirus Only / rBEV-mKOκ (orange), GAG-VLP (blue), GAG-GFP-VLP (green), SARS-VLP (purple). Samples stained with SYBR Green I dye to detect dsDNA-containing particles. Stages of semi-purification include infected cell culture supernatant, resuspended pellet, and iodixanol density gradient fractions. Yield percentage was normalized to infected cell culture supernatant. Yield percent of iodixanol density gradient fractions were combined to determine yield percent for the entire stage, displayed here.

Across all samples, sucrose cushion pellet yield % was lower than the infected cell culture supernatant, as expected (Figure B.3). Iodixanol gradient yield % appeared to decrease in order of GAG-GFP-VLP, baculovirus only, GAG-VLP, SARS-VLP. It should be noted that GAG-GFP-VLP and baculovirus only samples had yield % that exceeded the 100% normalization factor of infected cell culture supernatant.

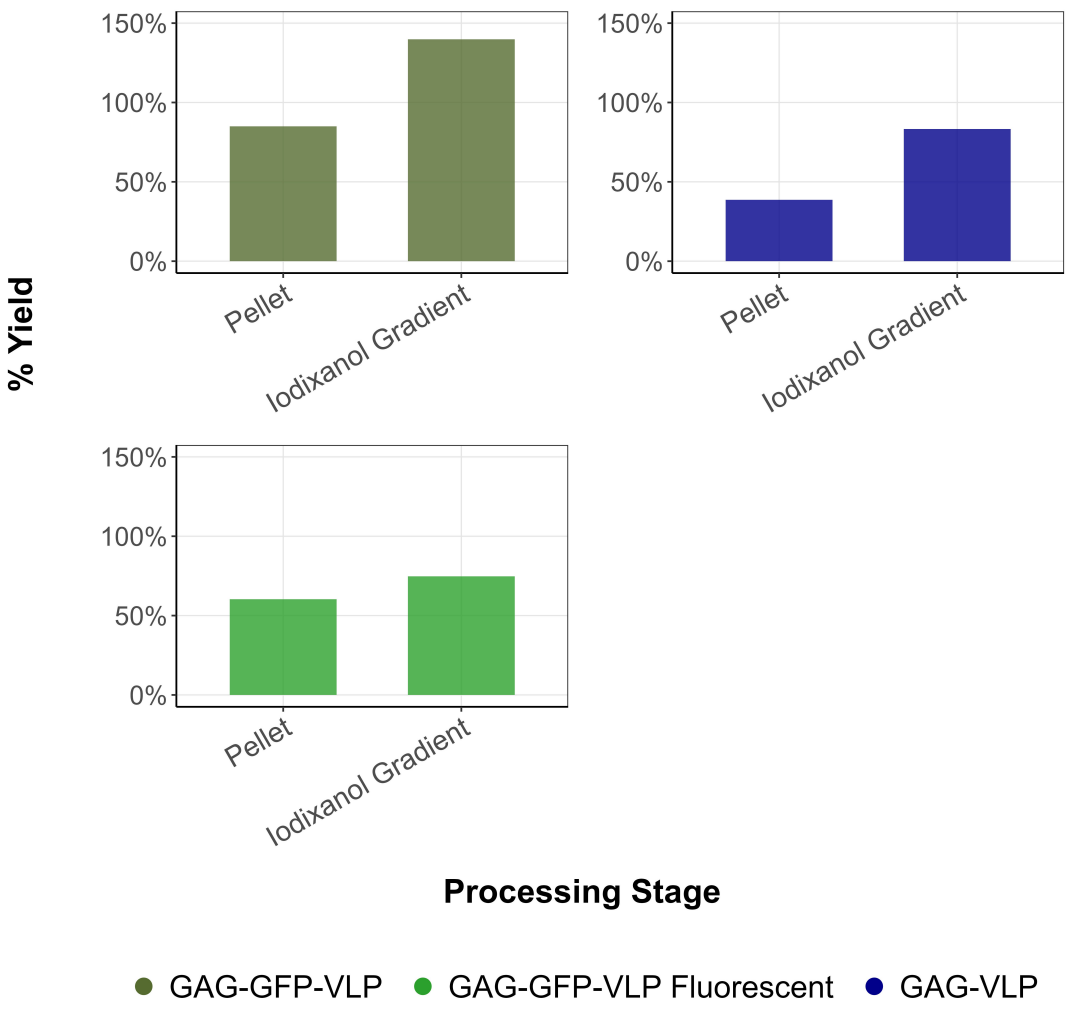

Figure B.4: Flow virometry-derived particle concentration in semi-purified sample. dsDNA-containing particles in GAG-VLP (dark blue), GAG-GFP-VLP (dark green). Fluorescent particles in GAG-VLP (light blue), GAG-GFP-VLP (light green). Fluorescent flow virometry of GAG-VLP samples yielded data close to the instrument LOD ($1.5 * 10^8$ Particles/mL) consistent with non-fluorescent signal shifting, data not shown. Stages of semi-purification include infected cell culture supernatant, resuspended pellet, and iodixanol density gradient fractions. Yield percentage was normalized to infected cell culture supernatant. Yield percent of iodixanol density gradient fractions were combined to determine yield percent for the entire stage, displayed here.

When compared to SYBR Green I stained flow virometry values, fluorescent flow virometry-derived yield % appears to be decreased. It is also of note that the iodixanol gradient yield % does not exceed the normalization factor of infected cell culture supernatant.

Appendix C

Multi-Angle Dynamic Light Scattering

C.1 Equations

C.1.1 Rayleigh Scattering Intensity Law

$$I = I_o + (\frac{1 + cos^2\theta}{2R^2})(\frac{2\pi}{\lambda})^4(\frac{n^2 - 1}{n^2 + 2})^2(\frac{d}{2})^6$$

[65]

I = Intensity of scattered light

I_o = Intensity of incident light

R = Distance from particle to detector

θ = Scattering angle

λ = particle radius

n = Refractive index of particle

d = Particle diameter

C.1.2 Stokes - Einstein - Sutherland

$$D = \frac{k_B T}{6\pi\eta r}$$

[66]

D = diffusion coefficient

k_B = Boltzmann constant

T = absolute temperature (K)

η = dynamic viscosity of the fluid

r = particle radius

C.1.3 Rayleigh–Gans–Debye Approximation

$$I \propto \ R^6 (\frac{n_p^2 - n_m^2}{n_p^2 + 2n_m^2})^2$$

[67]

I = Intensity of scattered light

R = Particle radius

n_p = Refractive index of particle

n_m = Refractive index of medium

C.1.4 Beer–Lambert Law

$$A = \epsilon \; c \; l$$

[68]

A = Absorbance

ϵ = Extinction coefficient

c = Particle concentration

l = path length

C.2 Supplementary Results

C.2.1 Density

Density gradient ultracentrifugation requires detailed knowledge of the gradient-forming medium, including density of each component solution. Various concentrations of NTC - iodixanol solutions were weighed at known volumes, enabling density to be calculated. Increasing iodixanol concentration corresponds linearly to increasing solution mass at a fixed volume. This indicates that increasing the proportion of iodixanol in a solution results in a denser solution.

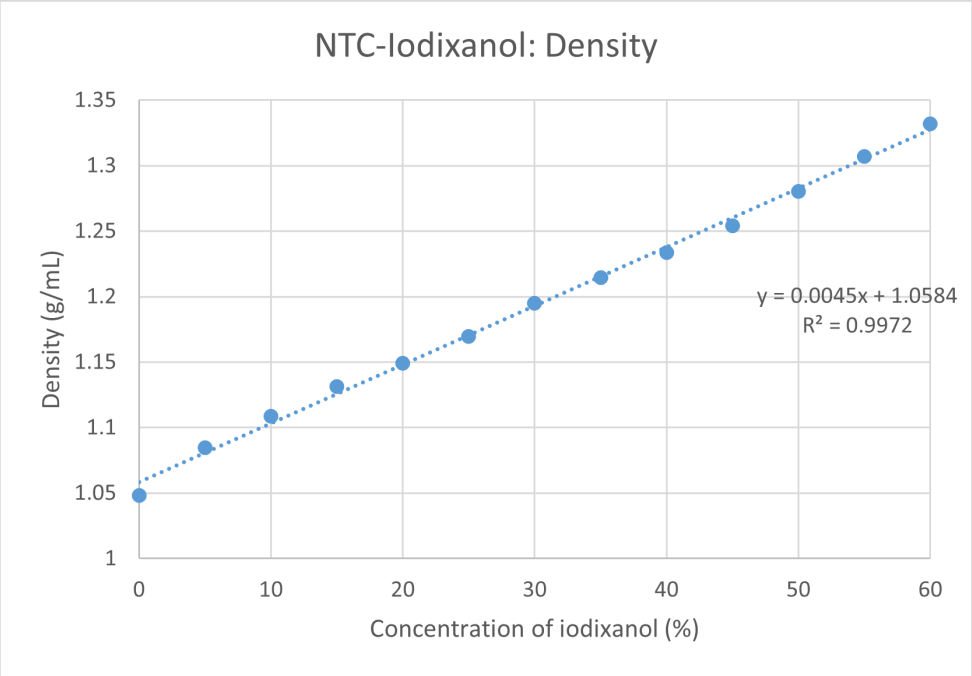

Figure C.1: Density of iodixanol-NTC solutions at varying concentration of iodixanol. Solutions of iodixanol were made from Optiprep™, a 60% iodixanol-water solution by dilution into NTC buffer. Density was determined for solutions of increasing iodixanol concentration which were made in increments of 5%, from 0 to 60%.

C.2.2 Refractive Index

MADLS measurements are moderately affected by the refractive index of the medium in which particles to be characterized are suspended, necessitating knowledge of refractive index of sample solution. In lieu of measuring refractive index of each sample, a relationship between density and refractive index of NTC – iodixanol was determined. Various concentrations of NTC - iodixanol solutions were measured using a refractometer, allowing

refractive index to be derived. Increasing solution density corresponds linearly to increasing refractive index. This indicates that increasing the proportion of iodixanol in a solution results in a solution with an increased capacity to bend light.

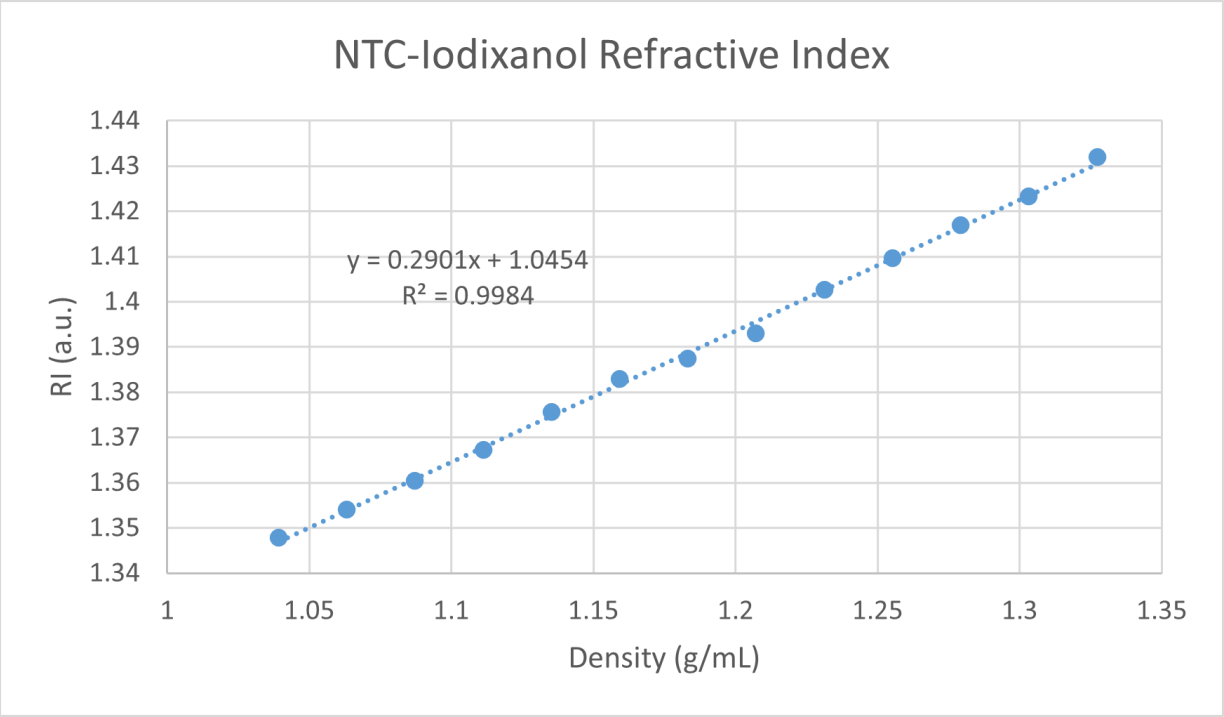

Figure C.2: Refractive index of iodixanol-NTC solutions at varying concentrations of iodixanol. Iodixanol-NTC solutions were analyzed using a refractometer to determine their refractive indexes, a measure of how much light bends when passing through the solution.

C.2.3 Viscosity

MADLS measurements are significantly affected by the viscosity of the medium in which particles to be characterized are suspended, necessitating knowledge of viscosity of sample

solution. In lieu of measuring viscosity of each sample, a relationship between density and viscosity of NTC – iodixanol was determined. Various concentrations of NTC - iodixanol solutions were measured using a rheometer, allowing viscosity to be calculated. Increasing solution density corresponds to a 4th order polynomial relationship with increasing viscosity. This indicates that increasing the proportion of iodixanol in a solution results in disproportionate increase in solution viscosity.

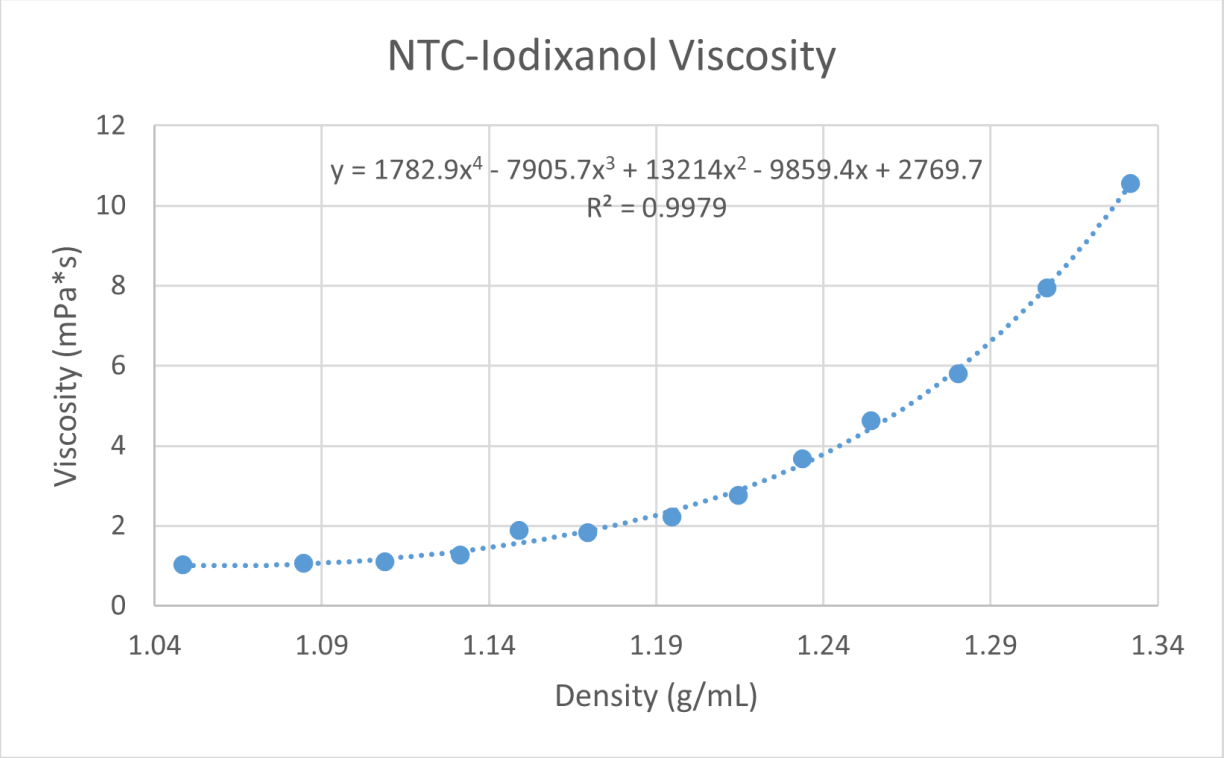

Figure C.3: Viscosity of iodixanol-NTC solutions at varying concentrations of iodixanol. Iodixanol-NTC solutions were analyzed using a rheometer to determine their viscosities, a measure of the fluid's resistance to flow.

C.2.4 MADLS Analysis of Separation Medium

To understand what particles are detected in a virus sample via MADLS, the pre-existing particles present in the separation medium must be identified and their presence documented. The effects of accounting for refractive index and viscosity (physical properties) of sample medium are also important to note. Various concentrations of NTC – Iodixanol were analyzed via MADLS with and without accounting for physical properties of individual solutions. Increasing iodixanol concentration in a solution without accounting for physical properties resulted in the shift of a range of particles to appear as though particles themselves and their range were larger, and less intensely scattered light. Accounting for physical properties of individual solutions resulted in previously larger particles and ranges shifting towards smaller particle sizes and more narrow ranges, all solutions presenting intensely light scattering molecules at 2 (+/-) 1 nm. This indicates that particles of approximately 2 nm are present within all NTC – iodixanol solutions, some of these being iodixanol particles themselves in addition to small approximately 1 nm particles and slightly larger 8 – 14 nm particles present in pure NTC. This also indicates that without correctly accounting for physical properties of individual solutions, particle sizes and intensities may vary significantly from their true values and negatively impact data quality.

Uncorrected versus Corrected

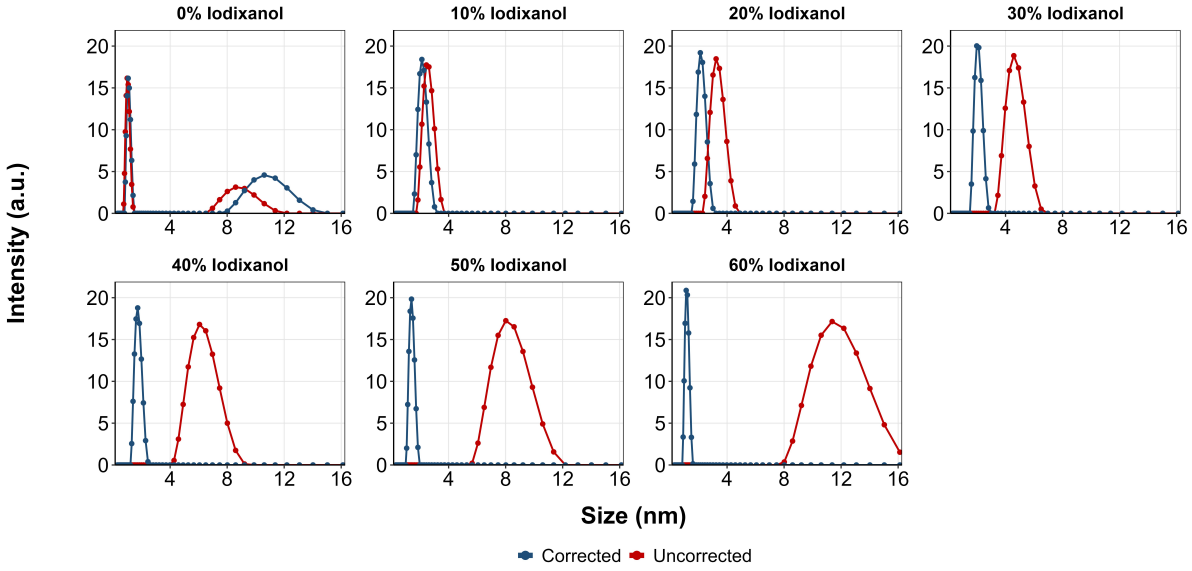

Figure C.4: Light scattering intensity and size distribution of particles in solutions of iodixanol-NTC at varying concentrations of iodixanol, before and after correcting for refractive index and viscosity. Samples of 0, 10, 20, 30, 40, 50, and 60% iodixanol-NTC were analyzed using MADLS. Uncorrected (red), Corrected (blue).

C.3 MADLS Methodology

Since MADLS-based analysis of polydisperse biological particle populations are not commonly reported in literature, it was necessary to determine whether or not the technique itself could generate good quality data. To determine this, particle concentration, size, and repeat detection (hit rate) were rigorously tested and results carefully scrutinized. Prior work resulted in the generation of a set of semi-purified samples of SARS-VLP which were

analyzed by various techniques. A key fraction was found to contain baculovirus, SARS-VLP, and approximately 14% Iodixanol-NTC. This was compared to sterile filtered 1 X NTC buffer via MADLS analysis. Briefly a cuvette was loaded with 1 mL of semi-purified SARS-VLP and analyzed, followed by a removal of sample and thorough cleaning protocol for the cuvette. 1 X NTC was loaded into the cleaned cuvette and analyzed, followed by a removal of samples and thorough cleaning protocol for the cuvette. This was repeated until 15 replicate scans were obtained for each the sample and buffer. Contained in this section is also repeat detection measurements for the main body of this work.

C.3.1 Concentration

The concentration of particles of diameters X where X is ($X < 50$ nm), (50 nm $< X < 250$ nm), and ($X > 250$ nm) were examined for the SARS-VLP sample and 1 X NTC buffer. The SARS-VLP sample was later analyzed via serial dilution and both concentration and size of particles were examined.

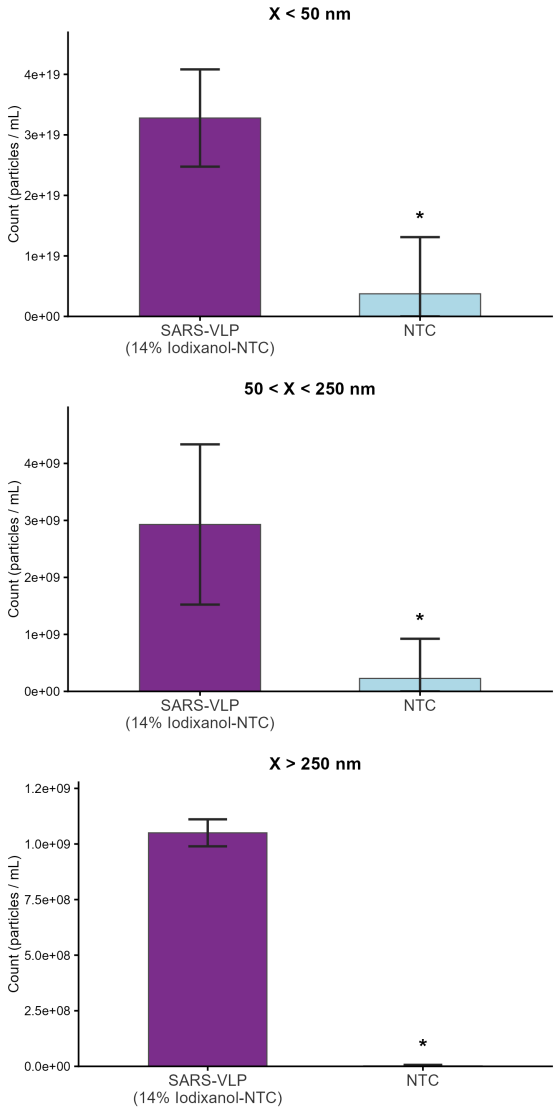

Figure C.5: MADLS-derived particle concentration measurement of known sample versus buffer for particles of a given diameter range. Known sample has been identified to contain recombinant baculovirus, SARS-VLP, and approximately 14% iodixanol-NTC (purple). 1 X NTC buffer (blue) had been sterile filtered prior to measurement and does not contain baculovirus, SARS-VLP, nor iodixanol. Graphs are divided by particles classes of a given diameter X. Top: (X $<$ 50 nm). Middle: (50 nm $<$ X $<$ 250 nm). Bottom: (X $>$ 250 nm). Asterisk (*) indicates that measurements were repeatedly inconsistent, and that less confidence can be placed on the noted data. Error bars represent variability in triplicate repeat measurements of all non-sequential measurements.

Particle concentration is far more consistent for the SARS-VLP sample than for the 1 X NTC buffer, as indicated by the proporationate size of the error bars (Figure C.5). It is supposed that the iodixanol, SARS-VLP, and recombinant baculovirus present in the SARS-VLP sample all contribute to the consistency of the concentration measurements when compared to the buffer.

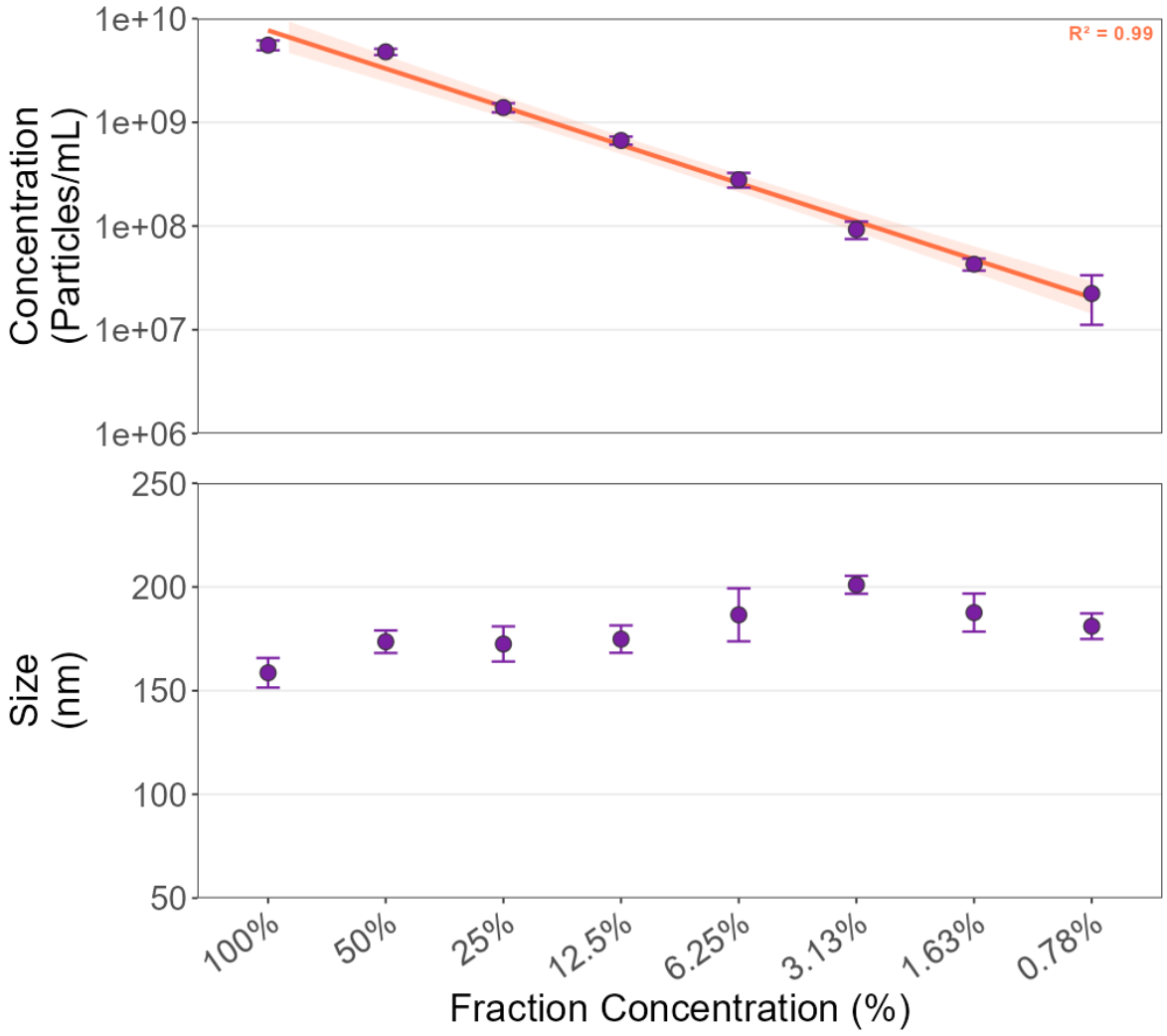

Figure C.6: MADLS-derived measurements of known sample for particles where (50 nm < diameter < 250 nm). Known sample has been identified to contain recombinant baculovirus, SARS-VLP, and approximately 14% iodixanol-NTC (purple). Sample was diluted with filtered 1 X NTC buffer by a factor of 2 for each successive measurement. Concentration (y-top) and size (y-bottom) are displayed at decreasing concentration (x) of the sample. Error bars represent decuplicate measurements.

For particles where (50 nm < diameter < 250 nm), concentration for the serially diluted

SARS-VLP sample shows a decreasing trend with a strong degree of linearity and low measurement variability as expected (Figure C.6). It is worth noting that as concentration decreases, the variability of the measurements appears to increase slightly. Size for these particles aligns with expectations and produces a relatively flat line, as it should not change the size of particles based on concentration changes. This is supported by the fact that the sample was diluted in the same buffer as the separation medium, maintaining ion concentration and not perturbing the electric double layer that contributes to apparent particle size. The particle size appears to increase slightly as the sample becomes more dilute, which is also in line with expectations that size measurements of particles of lower concentrations are less consistent than the same particles at higher concentrations.

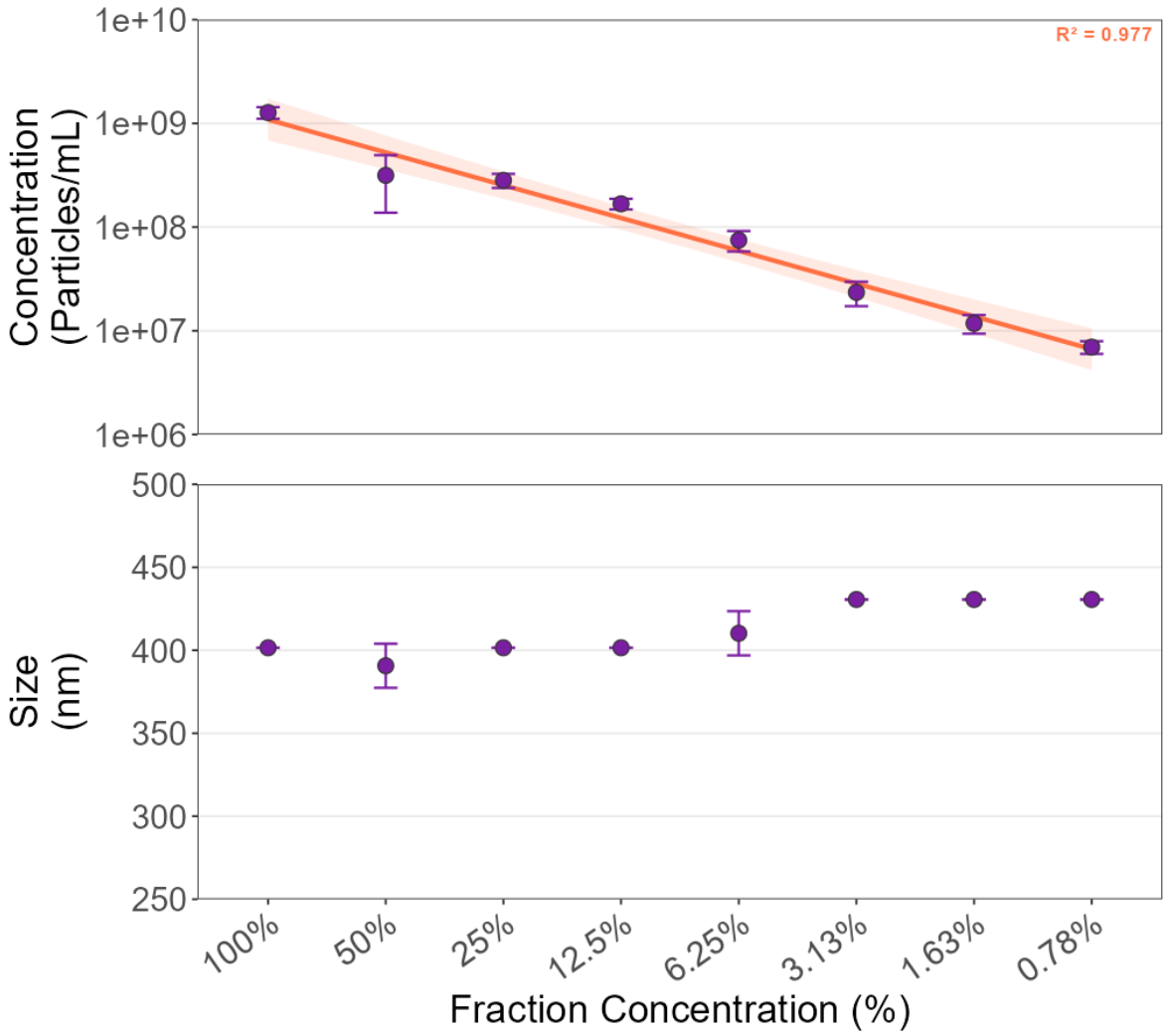

Figure C.7: MADLS-derived measurements of known sample for particles where (diameter $>$ 250 nm). Known sample has been identified to contain recombinant baculovirus, SARS-VLP, and approximately 14% iodixanol-NTC (purple). Sample was diluted with filtered 1 X NTC buffer by a factor of 2 for each successive measurement. Concentration (y-top) and size (y-bottom) are displayed at decreasing concentration (x) of the sample. Error bars represent decuplicate measurements.

For particles where (diameter $>$ 250 nm), the same observations apply as were noted

in C.6 (Figure C.7). The only major difference is that as particle concentration decreases, the measurement variability does not seem to be affected as drastically as particles where (50 nm $<$ diameter $<$ 250 nm). This is illustrated by the error bars in the concentration graph showing no significant increase at lower concentrations, which can be explained by the Rayleigh Scattering Intensity Law (See Appendix B.1.1)

C.3.2 Size

The size of particles of diameters X where X is (X $<$ 50 nm), (50 nm $<$ X $<$ 250 nm), and (X $>$ 250 nm) were examined for the SARS-VLP sample and 1 X NTC buffer.

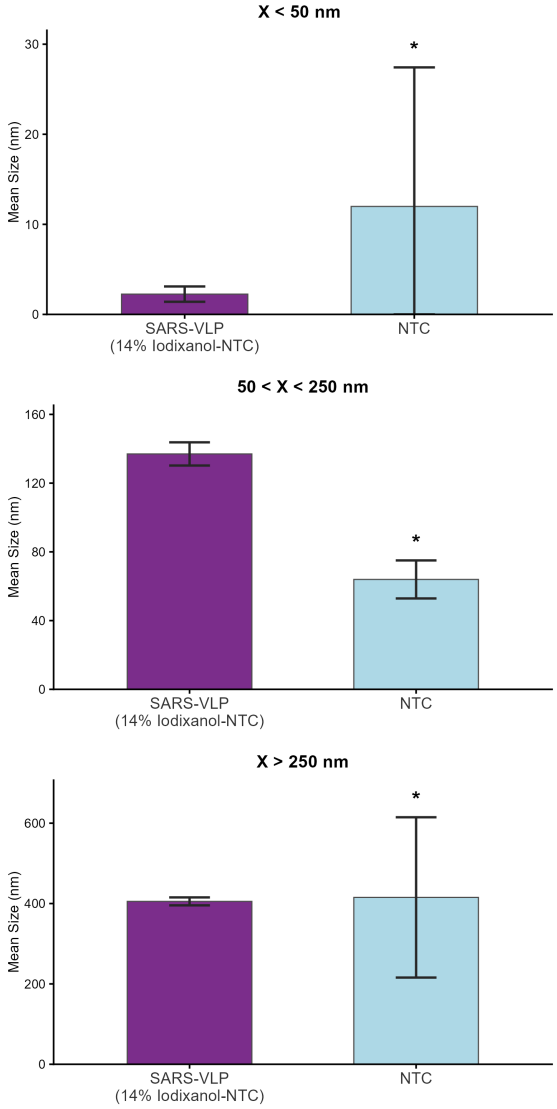

Figure C.8: MADLS-derived particle size measurement of known sample versus buffer for particles of a given diameter range. Known sample has been identified to contain recombinant baculovirus, SARS-VLP, and approximately 14% iodixanol-NTC (purple). 1 X NTC buffer (blue) had been sterile filtered prior to measurement and does not contain baculovirus, SARS-VLP, nor iodixanol. Graphs are divided by particles classes of a given diameter X. Top: (X $<$ 50 nm). Middle: (50 nm $<$ X $<$ 250 nm). Bottom: (X $>$ 250 nm). Asterisk (*) indicates that measurements were repeatedly inconsistent, and that less confidence can be placed on the noted data. Error bars represent variability in triplicate repeat measurements of all non-sequential measurments.

Since the MADLS has an internal algorithm for interpretation of scattered light intensity data, it will attempt to explain the data by using particles of a variety of sizes in its model. This means that though there may be particles in the 1 X NTC buffer, the extreme variability in their measurement makes it easy to determine that they are simply mathematical artifacts (Figure C.8).

C.3.3 Particle Detection Variability

For each sequential measurement of a sample, it is possible that a particle population that has appeared in prior measurements may not appear. It is also possible that the model used by the MADLS algorithm may class the same particle population under a slightly larger or smaller diameter "peak". To account for this particles were treated as classes and multiple sequential measurements were taken to ensure data reliability. Therefore it is established that real particles will appear consistently in sequential measurements, and mathematical artifacts will vary greatly between measurements. This variability in particle detection frequency is defined here as "Hit Rate". The hit rates of particles of diameters X where X is ($X < 50$ nm), (50 nm $< X < 250$ nm), and ($X > 250$ nm) were examined for the SARS-VLP sample, 1 X NTC buffer, and the semi-purified samples appearing in chapter 4 (Results).

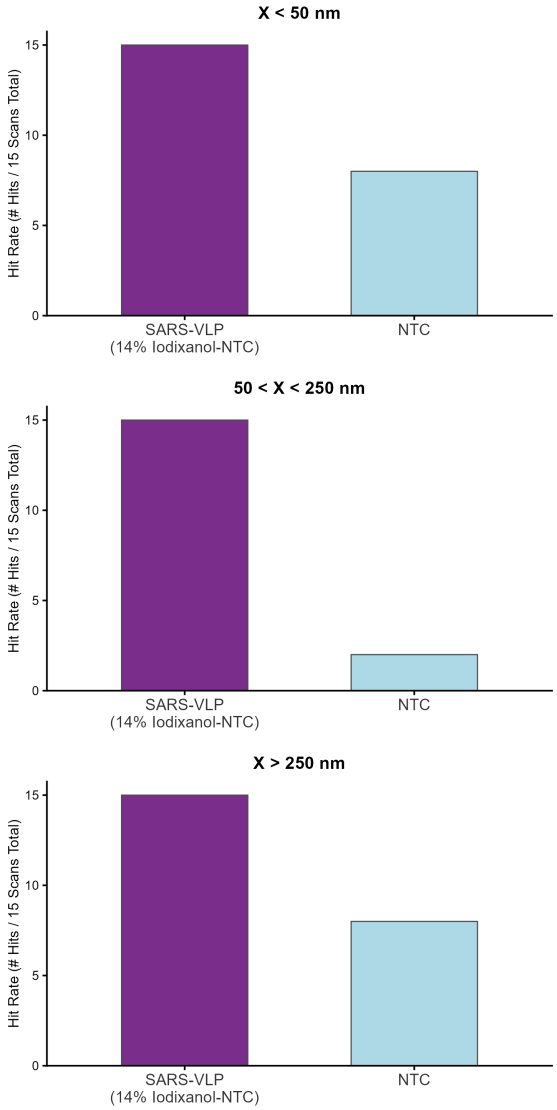

Figure C.9: Hit rate of known sample versus buffer for particles of a given diameter range. Known sample has been identified to contain recombinant baculovirus, SARS-VLP, and approximately 14% iodixanol-NTC (purple). 1 X NTC buffer (blue) had been sterile filtered prior to measurement and does not contain baculovirus, SARS-VLP, nor iodixanol. Graphs are divided by particles classes of a given diameter X. Top: (X $<$ 50 nm). Middle: (50 nm $<$ X $<$ 250 nm). Bottom: (X $>$ 250 nm). 15 scans were performed in total.

It is clearly demonstrated that for a sample known to contain particles the hit rate is very high, in this case the semi-purified SARS-VLP sample has a hit rate of 100% across all three particle classes (Figure C.9). For 1 X NTC buffer which is not expected to contain meaningful particles, the hit rate is at best 50% for certain particle classes, clearly demonstrating the facile differentiability of consistent and inconsistent readings from MADLS.

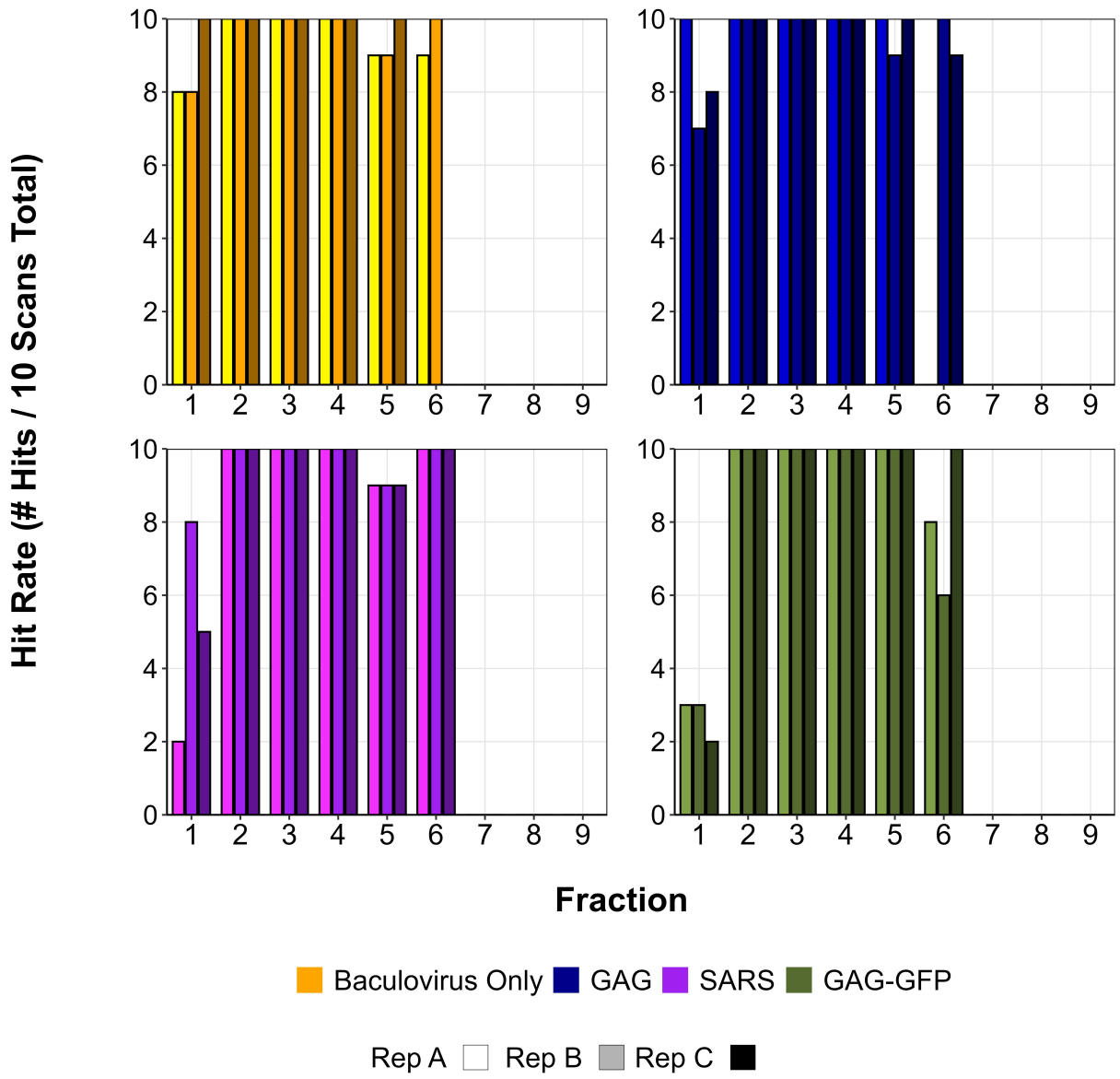

Figure C.10: Hit rate of semi-purified samples for particles of (50 nm < diameter < 250 nm). Baculovirus Only / rBEV-mKOκ (orange), GAG-VLP (blue), GAG-GFP-VLP (green), SARS-VLP (purple). Biological replicates of semi-purified samples are displayed together in varying shades. 10 scans were performed in total.

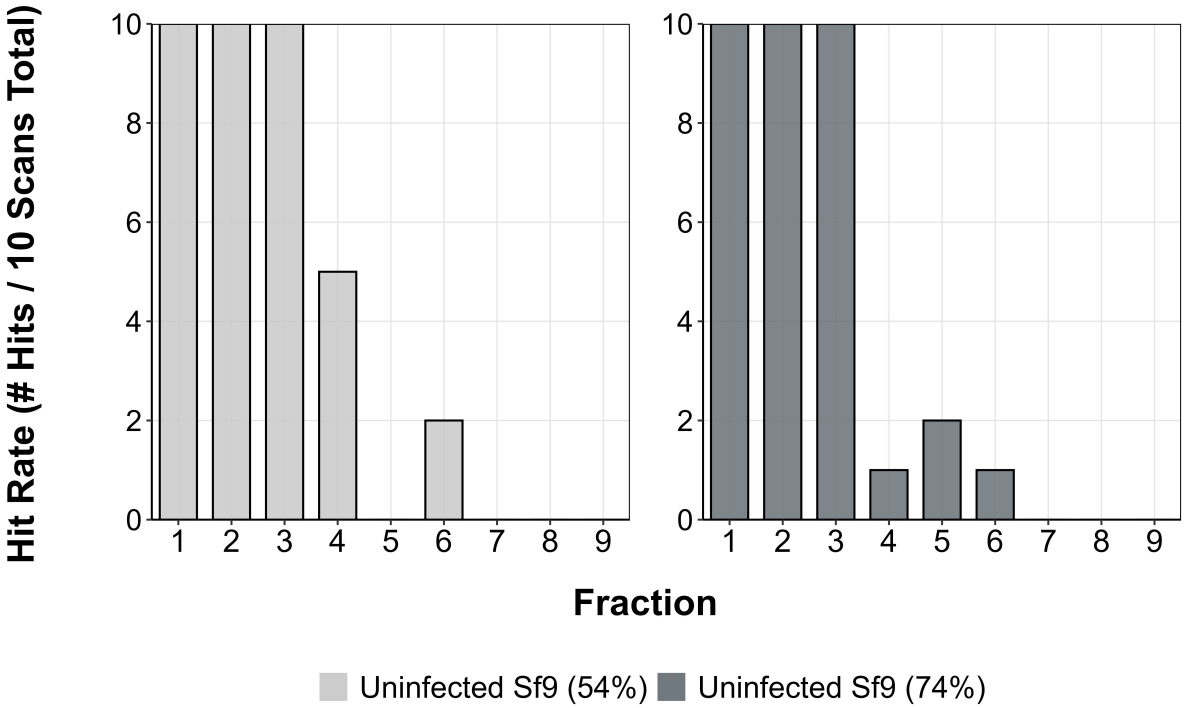

Figure C.11: Hit rate of semi-purified samples for particles of (50 nm $<$ diameter $<$ 250 nm). Uninfected Sf9 samples at 54% viability (light grey) and 74% viability (dark grey). 10 scans were performed in total.

For infected samples, the hit rate for particles of (50 nm $<$ diameter $<$ 250 nm) clearly demonstrates the consistency difference between each biological replicate within a sample, and between entire samples. It is worth noting that the fractions of major interest for this particle class, fractions 2 - 4, are the only fractions for which all replicates of all infected samples have extremely high hit rates (Figure C.10). This supports the assertion that real particles, perhaps VLPs or EVs, exist in these fractions at high concentrations. Uninfected samples possess high hit rates for particles of this class in fractions 1 - 3 (Figure C.11).

This high hit rate overlap between fractions 2 and 3 for both uninfected and infected samples indicates that particles of this class may be produced irrespective of infection by baculovirus.

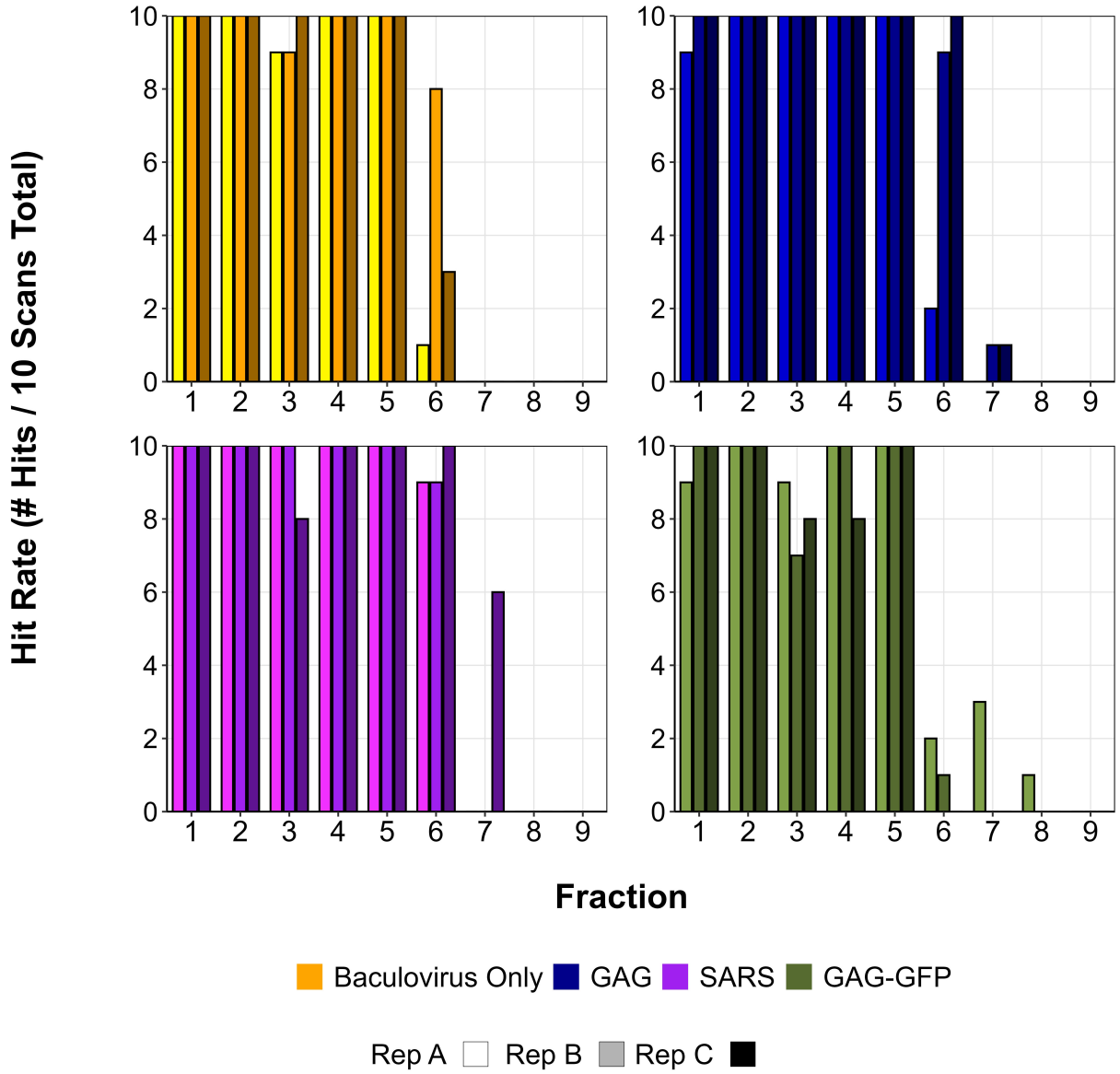

Figure C.12: Hit rate of semi-purified samples for particles of (diameter $>$ 250 nm). Baculovirus Only / rBEV-mKOκ (orange), GAG-VLP (blue), GAG-GFP-VLP (green), SARS-VLP (purple). Biological replicates of semi-purified samples are displayed together in varying shades. 10 scans were performed in total.

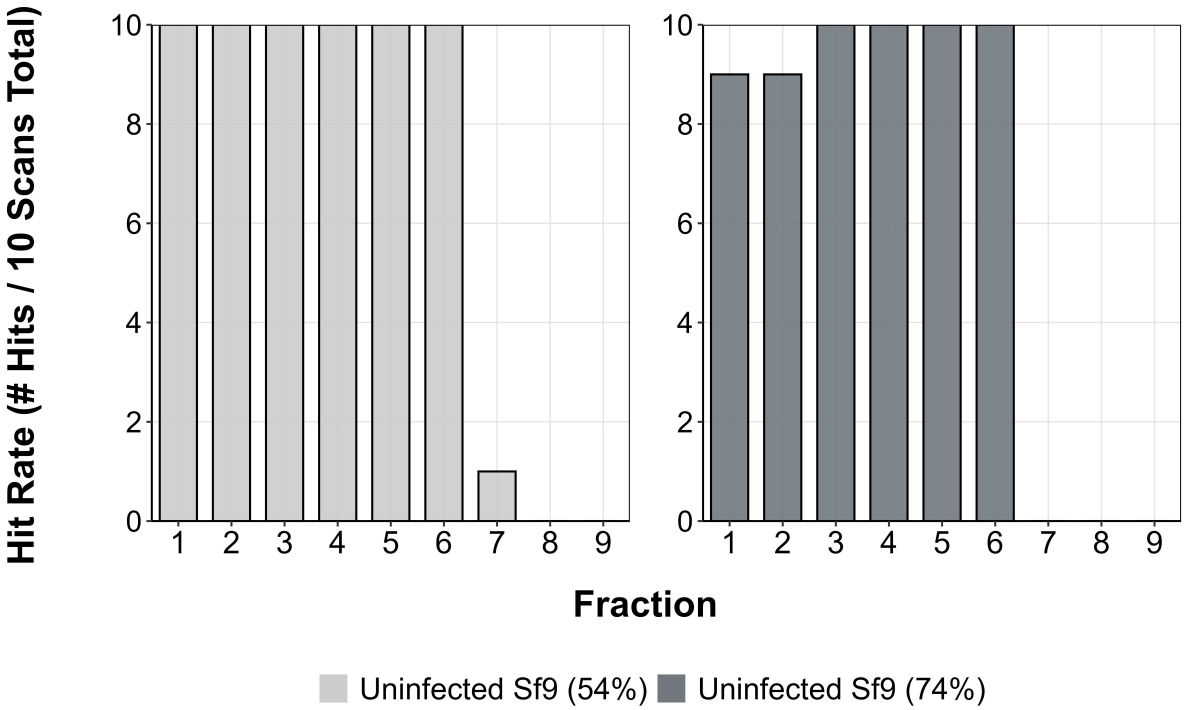

Figure C.13: Hit rate of semi-purified samples for particles of (diameter > 250 nm). Uninfected Sf9 samples at 54% viability (light grey) and 74% viability (dark grey). 10 scans were performed in total.

The hit rate for particles of (diameter > 250 nm) is very high for fractions 1 - 5 across all infected samples and replicates, but is markedly lower for all replicates of GAG-GFP-VLP fraction 3 (Figure C.12). This can be explained by the depolarized light scattering caused by the fluorescent GAG-GFP-VLPs in the same fraction, interfering with measurement consistency by masking existence of larger particles occasionally and smaller particles to a great extent. Uninfected samples possess a high hit rate for particles of this class between fractions 1 - 6 (Figure C.13). The overlap in particles of this class present in fractions of

similar densities between both infected and uninfected samples suggests that particles of this density are present during cell death irrespective of infection.

C.3.4 Solvent Peaks

As noted in C.2.4, solutions of iodixanol-NTC possess characteristic intensity peaks at approximately 2 nm, which are attributed to the presence of iodixanol in the medium and are referred to as "Solvent Peaks". It is demonstrated that measured solvent peak size becomes increasingly repeatable in later fractions across all samples (Figure C.14), consistent with the expected behavior of a single dominant scatterer (iodixanol) producing a stronger, more reproducible scattering signal at increasing concentration. It should be noted that the size measurements do not converge to a constant value but instead follow a curve across fractions. This indicates that the refractive index and viscosity corrections applied for the medium alone are sufficient to constrain the observed solvent peak size range, but require fraction-by-fraction refinement to achieve exact solvent peak matching.

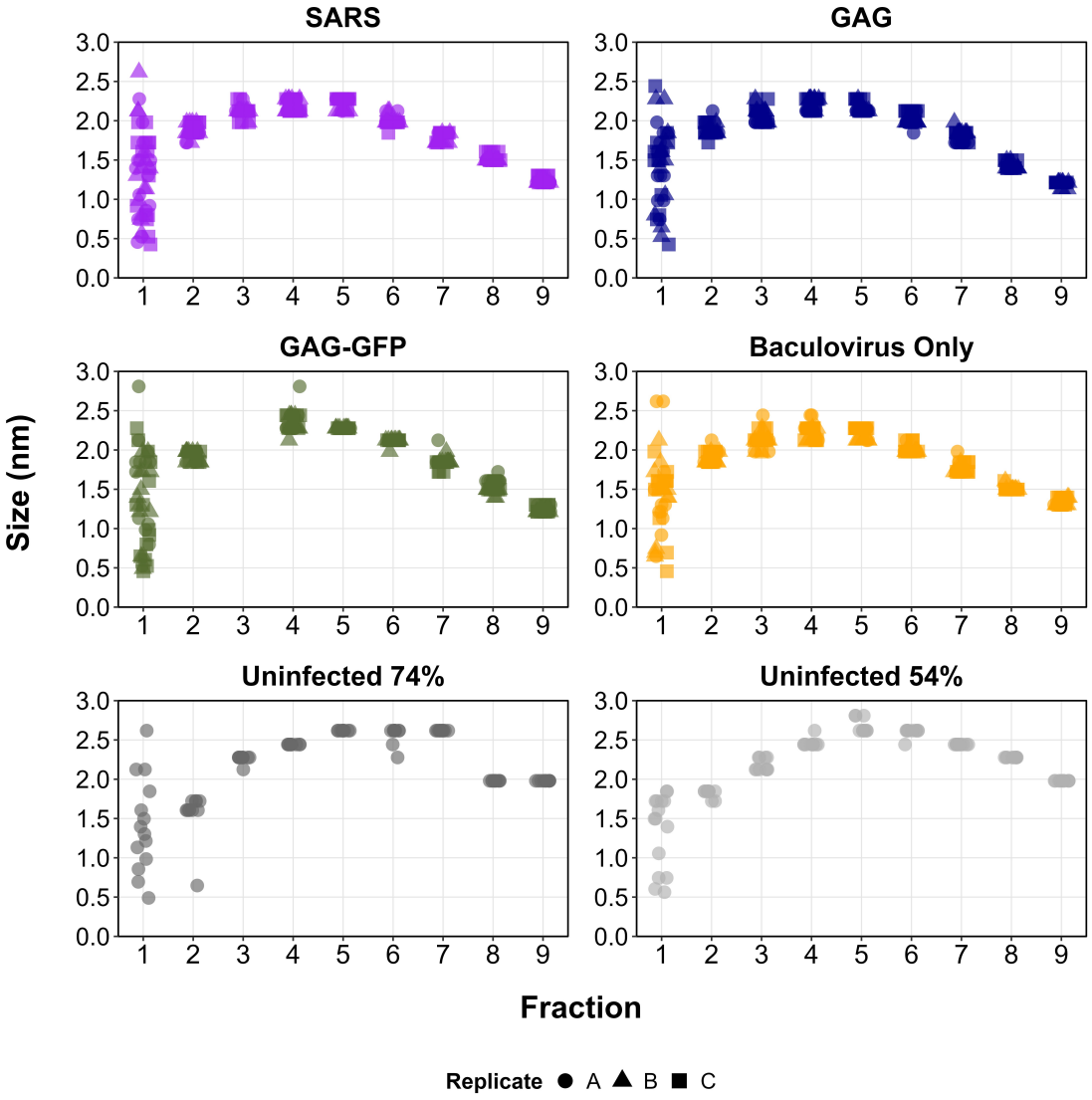

Figure C.14: Aggregated MADLS-derived size measurements of solvent peaks across semi-purified samples. SARS-VLP (purple), GAG-VLP (blue), GAG-GFP-VLP (green), Baculovirus Only / rBEV-mKOκ (orange), uninfected Sf9 samples at 54% viability (light grey) and 74% viability (dark grey). Each point represents a single MADLS scan; ten scans were aggregated per replicate across biological replicates A (circle), B (triangle), C (square). Peaks were restricted to a size range of 0.3 – 3 nm, where 0.3 nm represents the minimum diameter reported by MADLS and may not accurately resolve features at this scale. Refractive index and viscosity corrections were applied for the medium of each fraction. No measurements omitted.

C.3.5 Estimated VLP Concentration

It was noted that for particles of (50 nm $<$ diameter $<$ 250 nm), the baculovirus only samples which do not contain VLPs were showing high hit rates and similar concentrations and sizes to other VLP-containing semi-purified samples. This can be explained by the existence of extracellular vesicles (EVs), which are known to increase in concentration in supernatant upon infection of insect cells with baculovirus. For particles of this class, the average particle concentration in a given fraction of baculovirus only sample was subtracted from the same fraction of a VLP-producing sample. Since EVs and VLPs overlap in size and density, in some cases the subtraction results in a net concentration of zero. The results are displayed below.

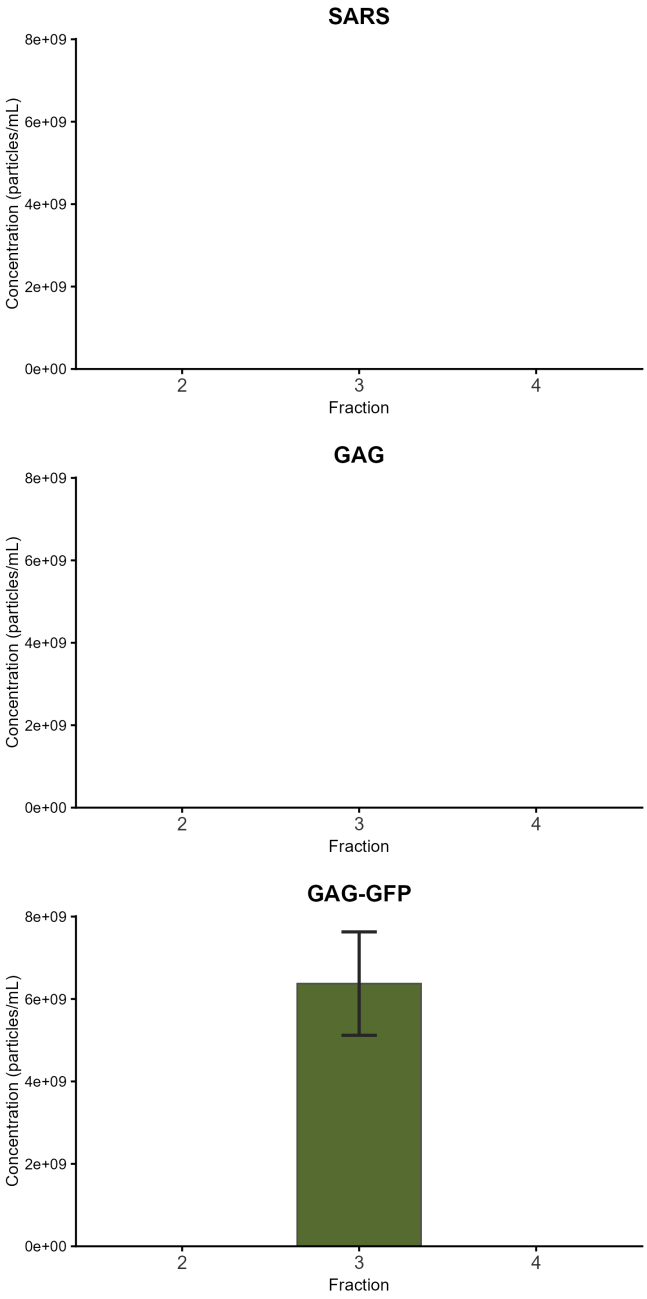

Figure C.15: Estimated concentration of VLPs in VLP-producing samples. Concentrations of particles of (50 nm $<$ diameter $<$ 250 nm) for Baculovirus Only / rBEV-mKOκ were subtracted from the VLP-producing samples: GAG-VLP (blue), GAG-GFP-VLP (green), SARS-VLP (purple). Where error $>$ data, samples were omitted.

It is clearly evident that GAG-GFP-VLP has significantly more VLPs present in fraction 3 than possible EVs in baculovirus only fraction 3 (Figure C.15). It is also clear that there are no more VLPs present in any other fraction than EVs that may have been produced in those same fractions by baculovirus only samples. This points to the fact that EVs and VLPs may egress the cell by similar mechanisms, or possibly that they may be produced at the expense of one another due to limits on host cell resources.

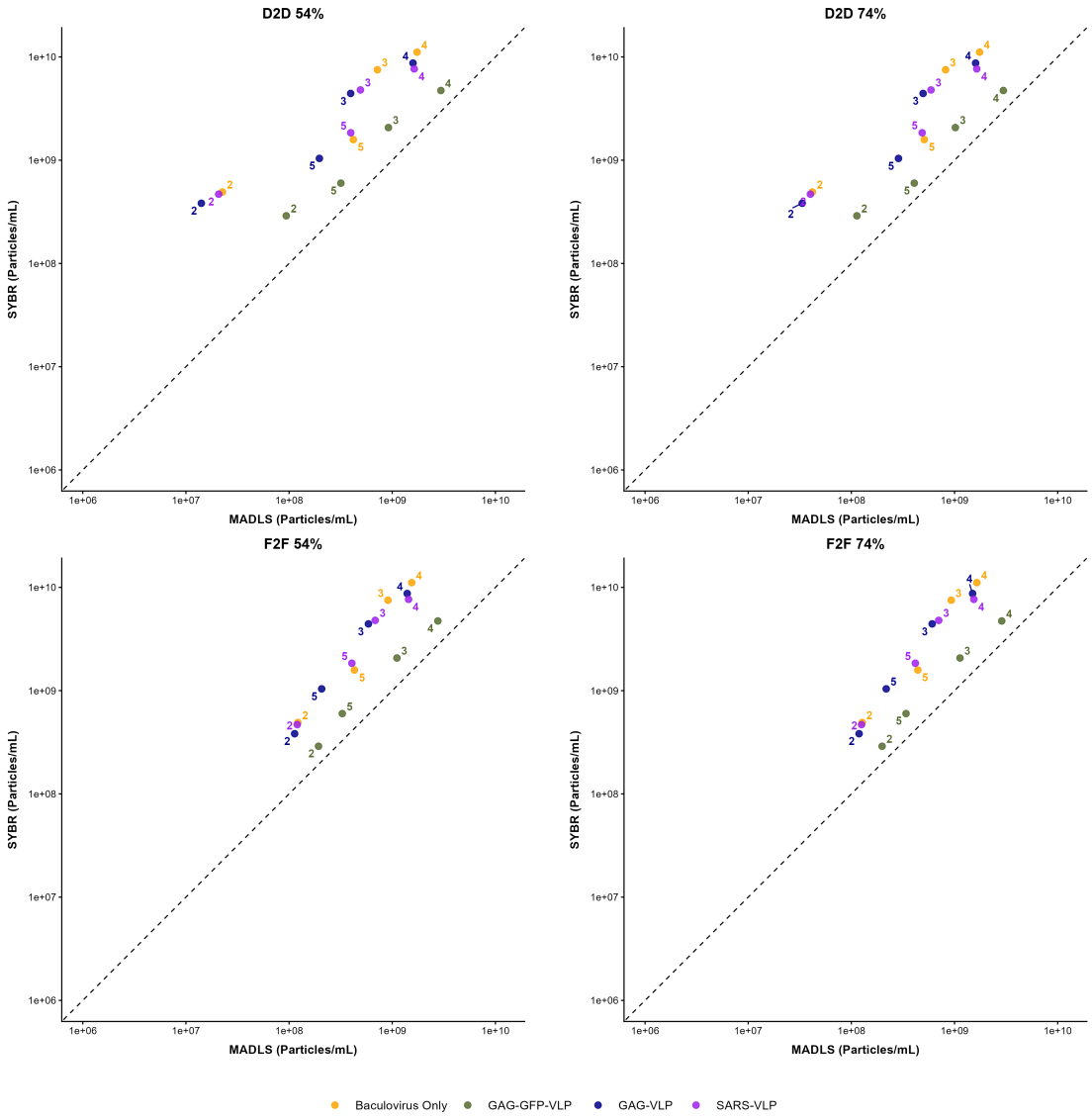

Figure C.16: Correlation between MADLS-derived particle concentration for particles of diameter $>$ 250 nm (x) and dsDNA-containing particles detected via SYBR Green I flow virometry (y) in semi-purified samples after subtraction of the MADLS-derived value by a given uninfected Sf9 supernatant sample concentration at 54% viability (54%) or 74% viability (74%) by fraction (F2F) or density (D2D) matching. Baculovirus Only / rBEV-mKOκ (orange), GAG-VLP (blue), GAG-GFP-VLP (green), SARS-VLP (purple). Numerical label indicates fraction number. Dashed line indicates equivalency between measurements of both methods.

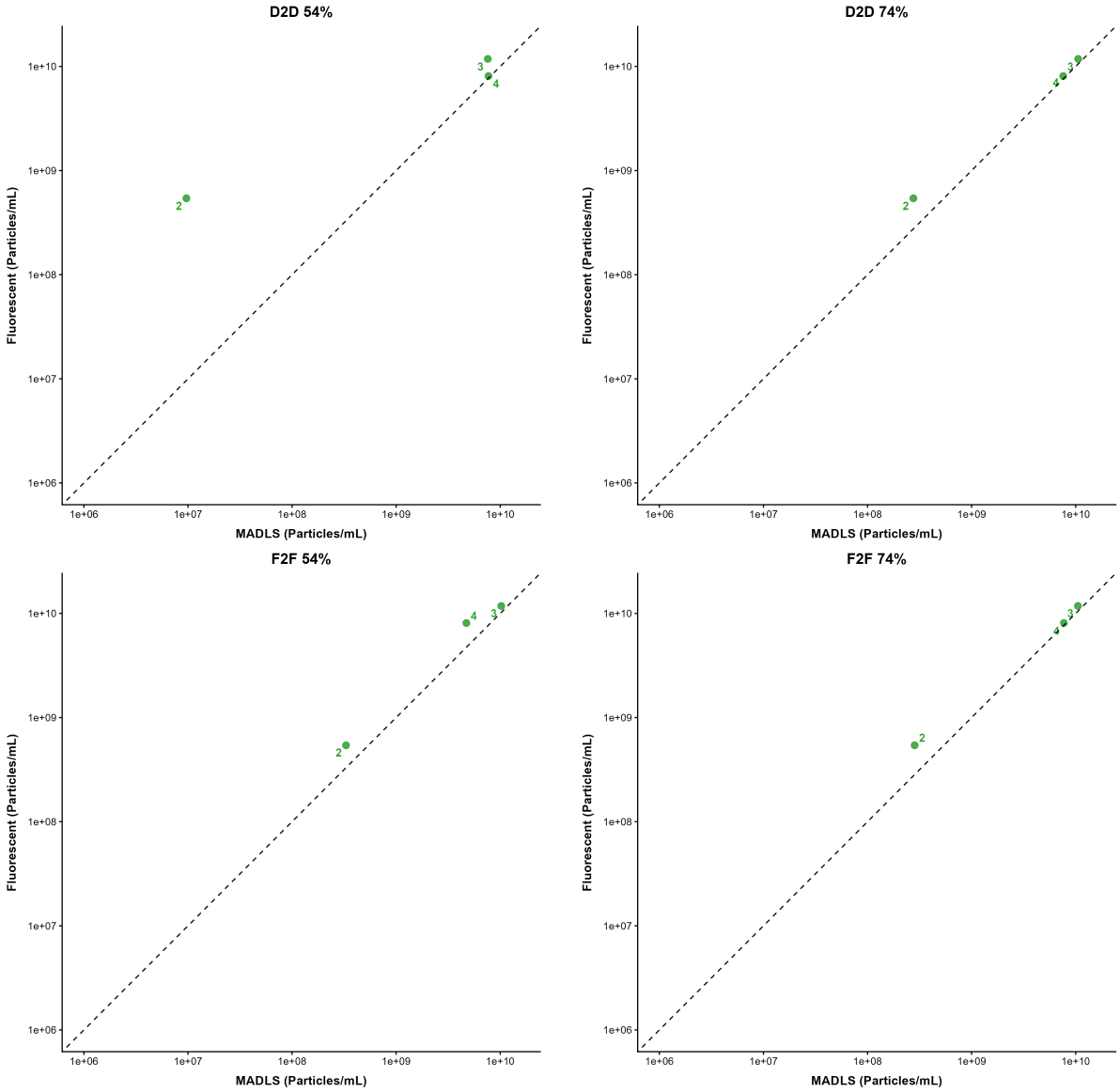

Figure C.17: Correlation between MADLS-derived particle concentration for particles of 50 nm $<$ diameter $<$ 250 nm (x) and fluorescent particles detected via flow virometry (y) in semi-purified samples after subtraction of the MADLS-derived value by a given uninfected Sf9 supernatant sample concentration at 54% viability (54%) or 74% viability (74%) by fraction (F2F) or density (D2D) matching. Baculovirus Only / rBEV-mKOκ (orange), GAG-VLP (blue), GAG-GFP-VLP (green), SARS-VLP (purple). Numerical label indicates fraction number. Dashed line indicates equivalency between measurements of both methods.

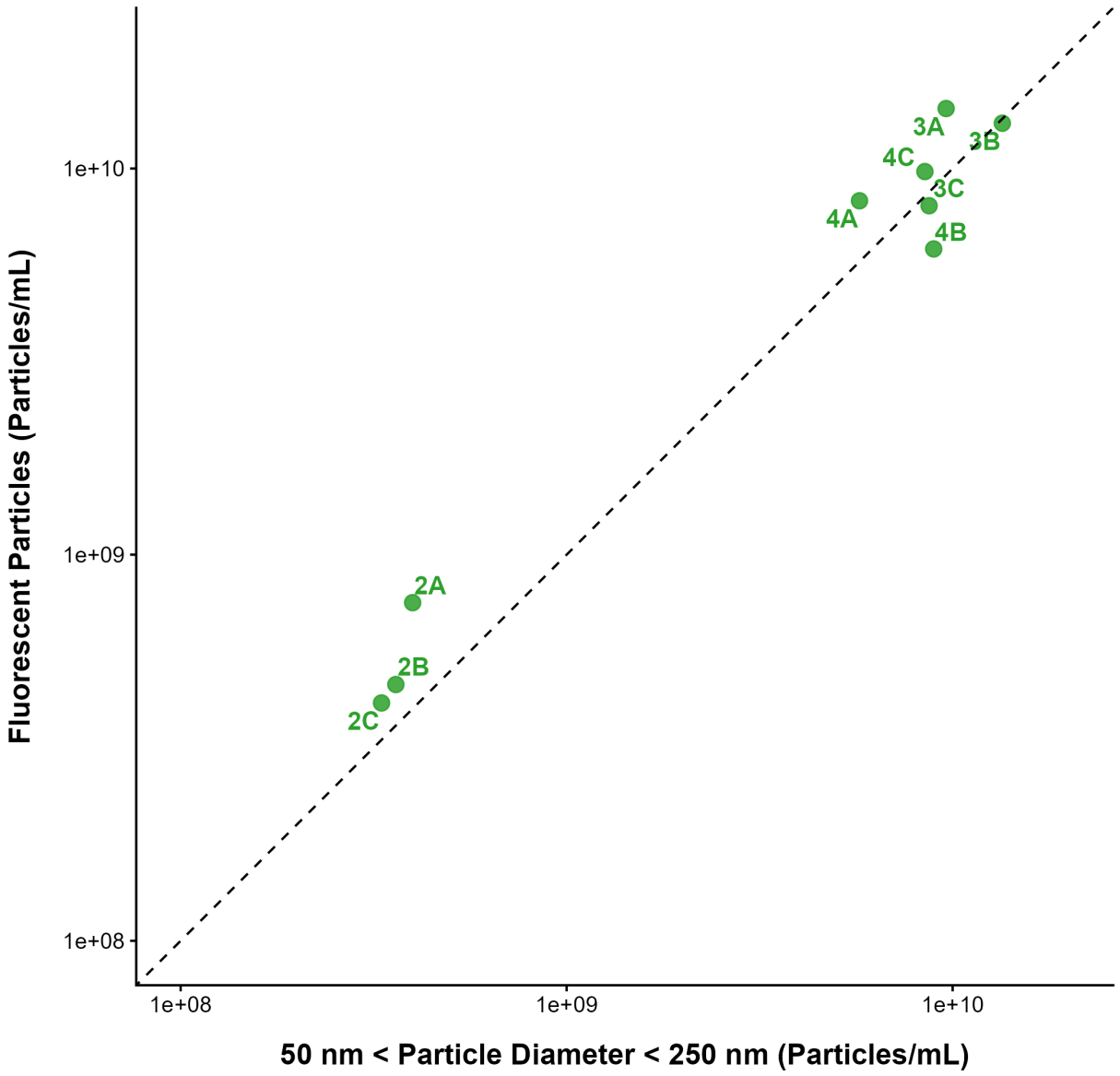

Figure C.18: Correlation between MADLS-derived particle concentration for particles of 50 nm $<$ diameter $<$ 250 nm (x) and fluorescent particles detected via flow virometry (y) in semi-purified samples separated by biological replicates. GAG-GFP-VLP (green). Numerical label indicates fraction number, letter label indicates biological replicate (A, B, C). Dashed line indicates equivalency between measurements of both methods.

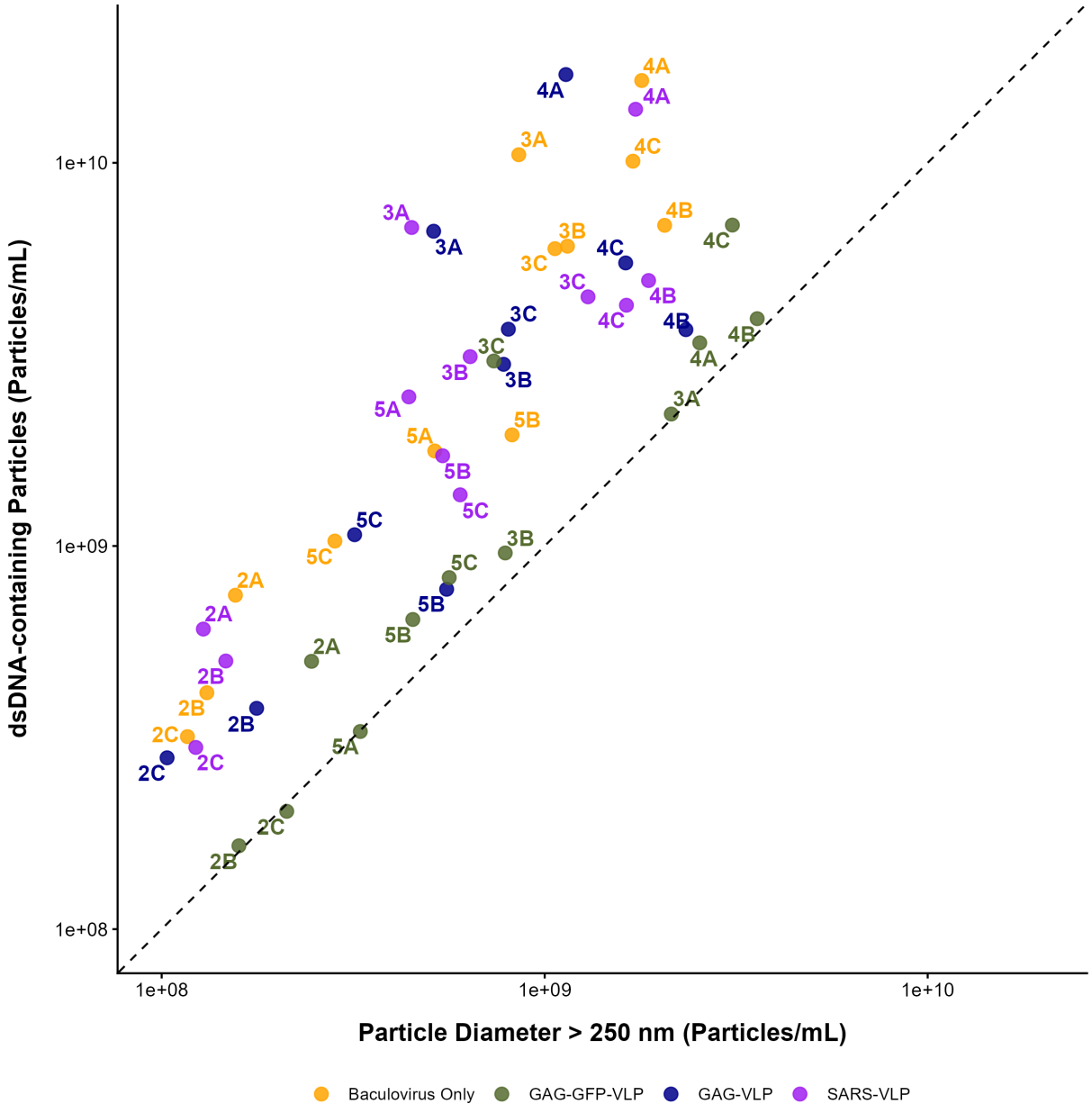

Figure C.19: Correlation between MADLS-derived particle concentration for particles of diameter > 250 nm (x) and dsDNA-containing particles detected via SYBR Green I flow virometry (y) in semi-purified samples separated by biological replicates. GAG-GFP-VLP (green). Numerical label indicates fraction number, letter label indicates biological replicate (A, B, C). Dashed line indicates equivalency between measurements of both methods.

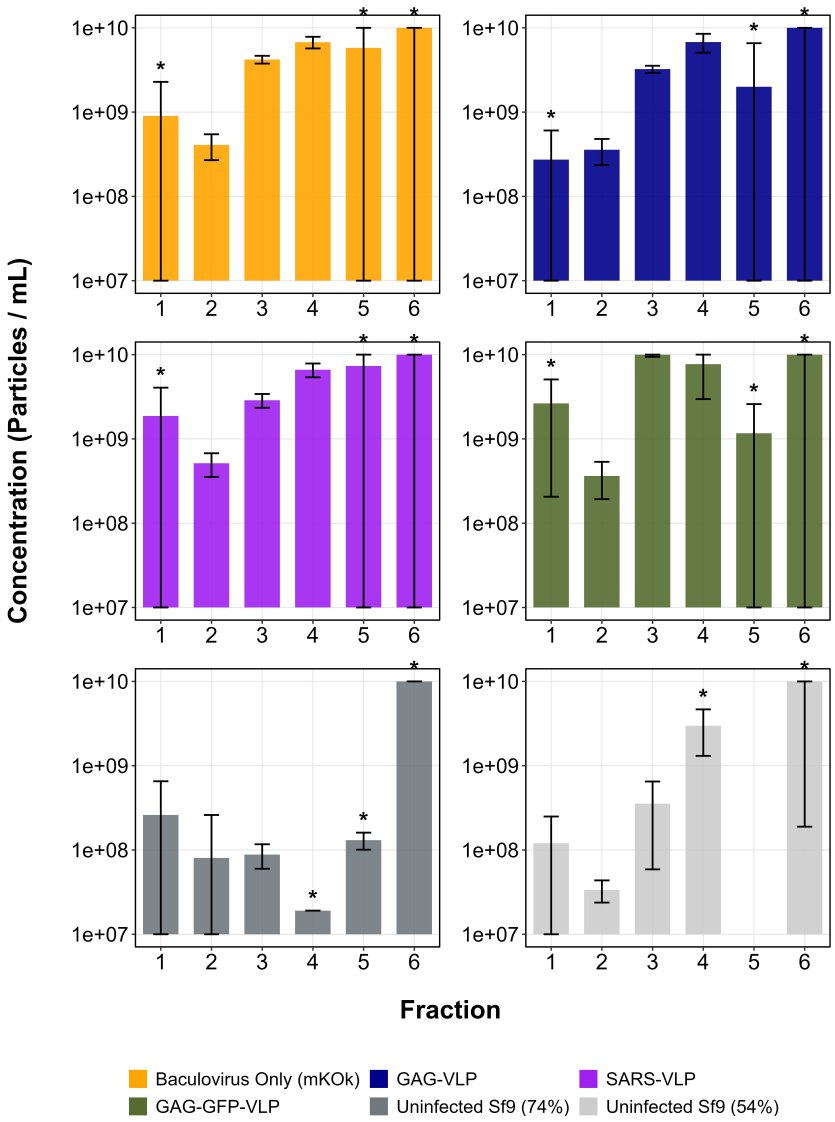

Figure C.20: MADLS-derived particle concentration in semi-purified samples for particles of 50 nm $<$ diameter $<$ 250 nm. Baculovirus Only / rBEV-mKOκ (orange), GAG-VLP (blue), GAG-GFP-VLP (green), SARS-VLP (purple), Uninfected Sf9 supernatant at 54% viability (light grey), 74% viability (dark grey). Although measurements were taken for fractions 1 - 9, confident measurements were only obtained for fractions 2 - 4 for infected and 1 - 3 for uninfected samples. Samples with a hit rate less than 50% of total scans or unacceptably high standard error are denoted by an asterisk (See C.10, C.11 for further details). Error bars represent decuplicate scans of biological triplicates for infected and decuplicate scans for uninfected samples.

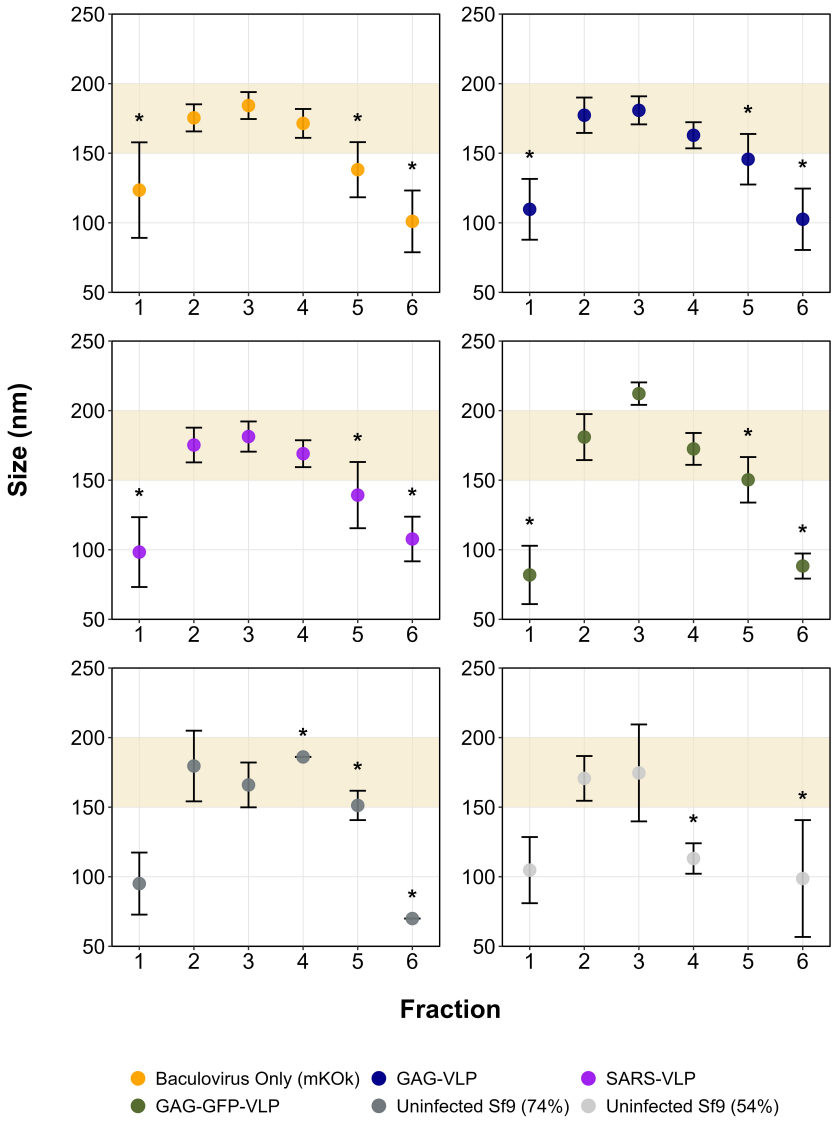

Figure C.21: MADLS-derived particle size in semi-purified samples, for particles of 50 nm < diameter < 250 nm. Baculovirus Only / rBEV-mKOκ (orange), GAG-VLP (blue), GAG-GFP-VLP (green), SARS-VLP (purple), Uninfected Sf9 supernatant at 54% viability (light grey), 74% viability (dark grey). Although measurements were taken for fractions 1 - 9, confident measurements were only obtained for fractions 2 - 4 for infected and 1 - 3 for uninfected samples. Samples with a hit rate less than 50% of total scans or unacceptably high standard error are denoted by an asterisk (See C.10, C.11 for further details). Error bars represent decuplicate scans of biological triplicates for infected and decuplicate scans for uninfected samples. Light beige graph area visually highlights particles between 150 - 200 nm in diameter.

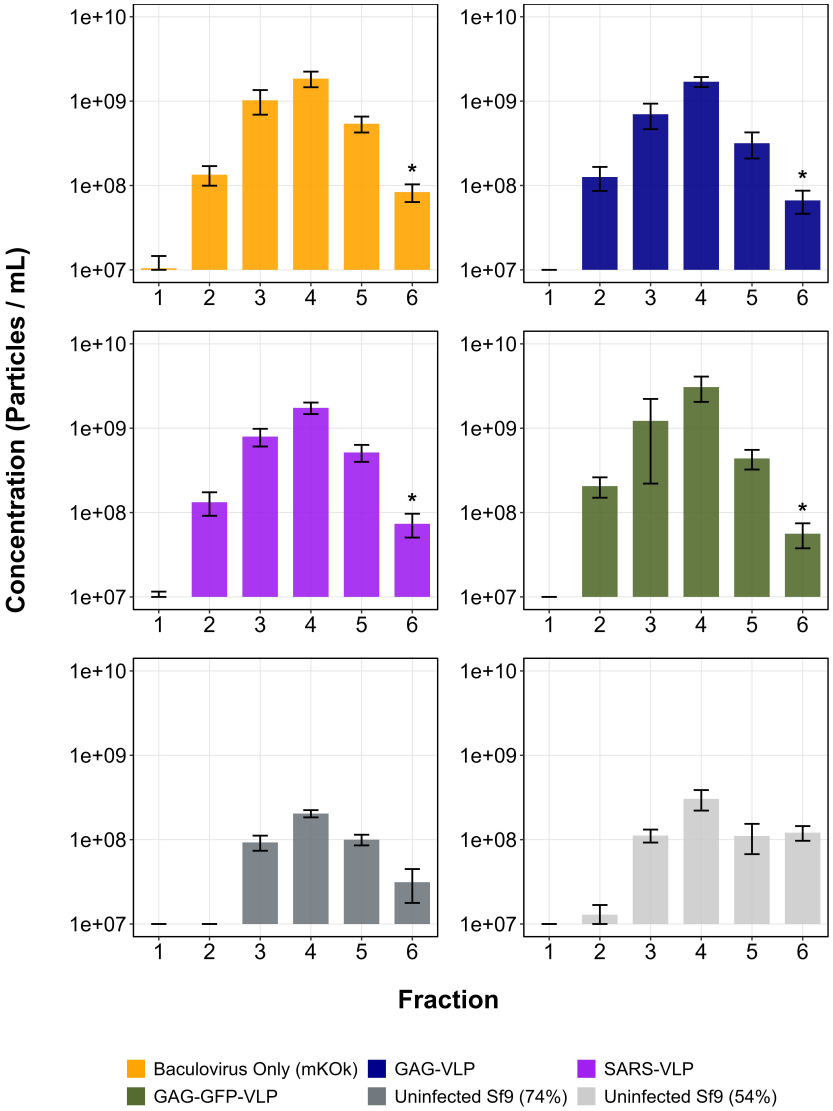

Figure C.22: MADLS-derived particle concentration in semi-purified samples for particles of diameter > 250 nm. Baculovirus Only / rBEV-mKOκ (orange), GAG-VLP (blue), GAG-GFP-VLP (green), SARS-VLP (purple), Uninfected Sf9 supernatant at 54% viability (light grey), 74% viability (dark grey). Although measurements were taken for fractions 1 - 9, confident measurements were only obtained for fractions 2 - 5 for infected and 1 - 6 for uninfected samples. Samples with a hit rate less than 50% of total scans are denoted by an asterisk (See C.12, C.13 for further details). Error bars represent decuplicate (10x) scans of biological triplicates for infected and decuplicate scans for uninfected samples.

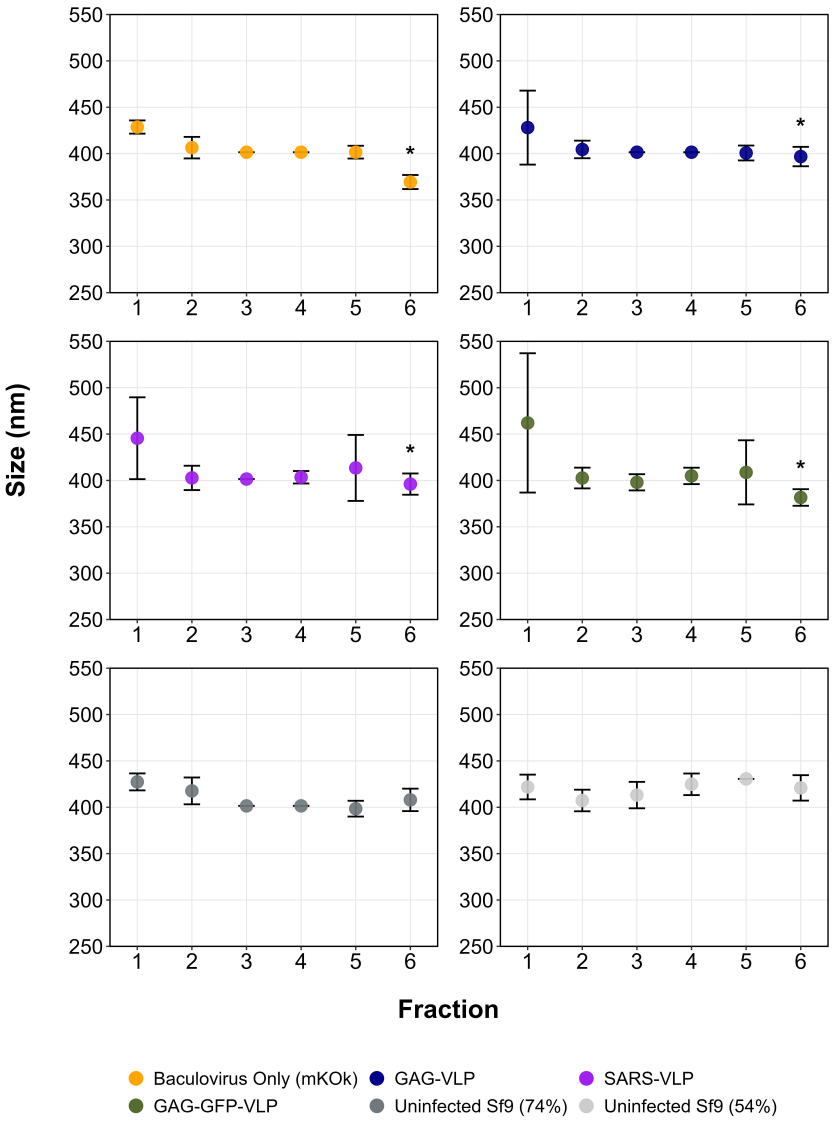

Figure C.23: MADLS-derived particle size in semi-purified samples for particles of diameter $>$ 250 nm. Baculovirus Only / rBEV-mKOκ (orange), GAG-VLP (blue), GAG-GFP-VLP (green), SARS-VLP (purple), Uninfected Sf9 supernatant at 54% viability (light grey), 74% viability (dark grey). Although measurements were taken for fractions 1 - 9, confident measurements were only obtained for fractions 2 - 5 for infected and 1 - 6 for uninfected samples. Samples with a hit rate less than 50% of total scans are denoted by an asterisk (See C.12, C.13 for further details). Error bars represent decuplicate scans of biological triplicates for infected and decuplicate scans for uninfected samples.